Sedimentology of the lower Uitenhage Group in the Middle to Late Mesozoic Oudtshoorn Basin, South Africa

By

Yambi Renato Daniel Dinis
Student number: **DNSYAM001**

Supervisor: Dr Emese M. Bordy

Dissertation presented for the degree of
Master of Science in Geology in the
Department of Geological Sciences,
University of Cape Town

April 2018

Plagiarism declaration

I hereby acknowledge that plagiarism is a wrongful act and punishable by university norms. Each significant contribution to, and quotation in this thesis from the work of others has been adequately attributed, cited and referenced using the South African Journal of Geology convention for citation and referencing.. I have not allowed, and will not allow anyone to copy my work with the intention of passing it off as their own.

Signature

Signed by candidate

Yambi Renato Daniel Dinis

Acknowledgements

I firstly thank my great supervisor Dr Emese M. Bordy for the great opportunity, for the priceless experience and the learning but most of all, for believing in and supporting me from the first moment right through every minute of difficulty, frustration, shouting, celebration and laughter. I thank her for being my inspiration in academia since my undergraduate studies and for striving to unlock the best of every student. May many more shine under her light!

I thank my siblings Jéssica, Bruna and Toy for their love, understanding and support, and for enduring all the hardships in my absence. I thank my siblings Vivi and Tshepang for their assured and endless love, comfort and support, and I thank them for our (new) source of joy, our little Tholoana. I thank tia Lídia and tia Anita for their immense motherly love, and Peter, tio Ciloya and the Tese family for their prayer, mentorship and support throughout my past 12 years of studying. I thank my Capoeira masters Mordaça and Espirrinho, “my elders” Sikhumbuzo and Soldado, “my love” Consuelo and “my wife” Rosalia who have helped me in the shaping of my persona in the past eight years, and for always, always, always having my back. To the Miti family: Professor, auntie Annie, Kochiwe, Kawesha, Pieter, the Miti-Drummonds, Mavuto and James Long Live The Don Miti Leader of the People, I will never be able to thank you enough or pay you back for being one of the greatest blessings in my lifetime. I thank my friends Rose, T’Nielle, Melissa, Sherissa, Américo, Rubem, Das Mangas, Paiva, Robert, Efésios, Silvestre, Pablo, Hernani, Tucunaré, Dárcio...and others, whom, very directly and indirectly, have kept me going during times of difficulty and hardship, even with simple words of encouragement. I give a special thanks to my dear friend Adjany for making the completion of this project possible. I thank the members of the SedPalaeo research team for making academia an even more enjoyable environment to be in, and for their priceless contributions to this project through assistance with the field work (esp. Robert and Miengah!!), discussions, acquiring of new skills and knowledge, words and acts of encouragement and the everyday chatter and laughter.

A big thank you to the academic, housekeeping, technical, administrative and scientific staff in the Department of Geological Sciences for their great support in the past eight years, during my undergradaute and postgradate studies. Lastly but not least, I thank the National Research Foundation of South Africa for having funded this research through a grant to my supervisor Dr Emese M. Bordy.

This thesis is dedicated to my mother to whom I owe my life, to my stepfather to whom, amongst many things, I owe my whole tertiary education and to my grandmother, the beginning and the reason for all this.

Abstract

The Oudtshoorn Basin is the largest onshore Mesozoic depocentre along the southern margin of South Africa, and is among the sedimentary basins that have been linked to the break-up of southern Gondwana. Filled by the continental lower Uitenhage Group, which for the most part is sparsely fossiliferous, difficult to correlate on a regional scale and void of non-renewable natural resources, the Oudtshoorn Basin is relatively poorly studied.

This project aims at carrying out an in depth, field- and lab-based investigation of the sediment supply processes and directions, location of sediment sources and palaeoclimate during the deposition of the lower Uitenhage Group in the Oudtshoorn Basin. In addition to the sediment transit patterns from source to sink via palaeocurrent measurements and petrographic studies, the sedimentary architecture was assessed via modern facies analysis techniques, which also permitted the investigation of the reason, the nature and the mode of sediment transport (traction currents vs. mass movements) in the early stages of Gondwana fragmentation.

The study identified nine facies associations, the composition, clast size and orientation of which suggest steep vs. gentle gradients along the northern and southern basin margins, respectively, and very gentle gradients in the basin centre. Furthermore, the common mass movement-deposits in the north contrast the sediments laid down by traction current and in turbid waters in the south, southwest, west and centre of the basin. Sediments were sourced from the northern and southern margins in alluvial fans, and moved toward the centre, where axial fluvial system dominated. Sedimentary facies distribution, grain size, and petrological composition collectively indicate sediment transport distances that were shorter and more rigorous in the north than in the south. Geochemical proxies and mineralogy indicate moderate weathering and deposition under an arid palaeoclimate. The lack of clear lithostratigraphic markers and the sparse distribution of isolated outcrops in the basin prevent the relative age assessment of the facies associations. This study highlights the need for systematic high-precision geochronological studies, if possible from drill core samples, of the facies associations identified herein to constrain the stratigraphic relationships in the Oudtshoorn Basin. Until these reconstructed palaeoenvironments are in temporal isolation, the history of the Oudtshoorn Basin and its relationship to the other Mesozoic grabens and half grabens of the southern Cape remain elusive.

Table of contents

List of figures

List of tables

1. Introduction

The Uitenhage Group of South Africa is host to the record of the separation of Gondwana into the southern hemisphere continents and India, and the opening of the South Atlantic during the Middle to Late Mesozoic. These events culminated in the geological and geographical settings of the present-day southern Cape region of South Africa (e.g., Du Toit, 1939; Lock et al., 1975; Dingle et al., 1983; McMillan et al., 1997; Koopmann et al., 2014). While the onset and major evolutionary events of the supercontinent break-up are debated (e.g.: Bond and Midgley, 2012; McPhee et al., 2016), consensus has that the rifting and drifting phases were completed by the Early to Middle Cretaceous (McLachlan and McMillan, 1976; McMillan et al., 1997; Muir, 2018 – in preparation).

Because of its regional geodynamic importance, the distribution area of the Uitenhage Group has been subject to several geological investigations, which focused on the rift processes that impacted on the formation of the region's passive continental margin, palaeoclimate and evolution of the flora and the fauna (e.g., Dingle, 1973, McLachlan and McMillan, 1976; Dingle et al., 1983; Shone, 2006; Muir et al., 2015; 2017a, b for recent reviews), as well as the changes in its landscape to the present day (e.g., Dingle et al., 1983; Wildman et al., 2015; Green et al., 2017; Marsh, 2016; Richardson et al., 2017; Muir, 2018 – in preparation). However, only a few studies (e.g., Du Preez, 1944; Lock et al., 1975; Holzförster, 2007) investigated the sedimentary facies and depositional environment of the Uitenhage Group in the Oudtshoorn Basin (Fig. 1.1), which is the largest outcrop area that preserves these rocks in the southern Cape region of South Africa. All in all, detailed basin-wide qualitative and quantitative modern sedimentary facies analysis studies are lacking; hence the evolution of the Mesozoic sedimentary fill of the Oudtshoorn Basin is still poorly understood.

1.1. Research rationale

The Uitenhage Group, which comprises high- to moderate-energy alluvial, fluvial and lacustrine sediments, for the most of its lower part, is sparsely fossiliferous, lithologically highly heterogeneous and thus difficult to correlate on a regional scale (Dingle et al., 1983). Because the unit has remained poorly studied and constitutes a regional stratigraphic correlation problem, its locally diverse fossil assemblages are in temporal isolation and their associated palaeoenvironments are rarely reconstructed (McLachlan and McMillan, 1976; Shone, 2006; Muir et al., 2015; McPhee et al., 2016). Furthermore, due to the lack of chrono- and biostratigraphic data, the onshore basins that contain the Uitenhage Group are correlated to the relatively better researched Algoa Basin and to their offshore counterparts by means of broad lithostratigraphic comparison only (Figs. 1.1 and 1.2A; Dingle, 1973; McLachlan and McMillan, 1976; Shone, 1978; Dingle et al., 1983; McMillan et al., 1997; Shone, 2006; Holzförster, 2007; Muir et al., 2017a, b).

1.2. Aims of research

The main aim of this multidisciplinary study is to provide an assessment of the sedimentological changes that occurred in the Oudtshoorn Basin during the Mesozoic Gondwana break-up and focuses on the palaeoenvironmental reconstruction of the Enon and Kirkwood Formations in this part of the southern Cape. Therefore, this project, using robust basin-wide data, is aimed at an in depth, field- and lab-based investigation of the sediment architecture, sediment supply processes and directions, palaeoclimatic proxies as preserved in the Mesozoic conglomerates and associated clastic sedimentary rocks of the Oudtshoorn Basin. This will allow the assessment of the depositional history in the basin, including: 1) the sediment transit patterns; 2) the nature of the sediment-generating events, and 3) broad palaeoclimatic patterns in the basin during the break-up of Gondwana. By applying modern facies analysis techniques, the sedimentary architecture of these deposits would also permit the investigation of the reason, the nature and the mode of sediment transport (traction currents vs. mass movements) from source to sink in the early stages of

Gondwana fragmentation. While this sedimentological study will be important for the spacio-temporal contextualisation of fossil discoveries in the study area, by providing a reconstruction of the local palaeoenvironments, the study is not aimed at assessing fossils. No fossils were collected in the field; however, palaeontologist colleagues were alerted about the few new findings made during this study.

The next sub-section of this chapter briefly describes the geological context of onshore Mesozoic basins of South Africa, with a focus on the Oudtshoorn Basin. Chapter 2 is dedicated to the methods applied, which includes field- and lab-based sedimentological, standard petrographic and geochemical techniques. Chapter 3 is a description of the results from the various methods applied. Chapter 4 is the interpretation of each proxy, as well as a synthesis of what they collectively represent (e.g., an explanation on how the combination of modern facies analysis, petrography and geochemisitry allowed for, among others, palaeoclimate inferences). Chapter 5 aims to discuss the inferences made based on the results and the implications to the research questions at hand. The last section concludes the project and explains the contributions made in this project for the better understanding of the geology of the Oudtshoorn Basin.

1.3. Geological context

1.3.1 Tectonic setting of the Oudtshoorn Basin

The Oudtshoorn Basin, the largest of the onshore Mesozoic basins in southern Africa (Lock et al., 1975; Dingle et al., 1983; Shone, 2006), forms part of one of the several onshore rift-basin segments that resulted from the continental breakup of Gondwana in the southern region of South Africa (Fig. 1.1). It is understood that these Mesozoic basins are erosional and/or structural relicts of the original depositional areas that existed in this region during the early fragmentation of the supercontinent. These rift basins form several discontinuous depositional chains of grabens and half grabens, which follow fault lines that trend in a roughly east to west direction within the present-day Cape

Mountains (Fig. 1.1A) (Dingle et al., 1983). These large, mainly southward-throwing normal faults that bound asymmetric major fold structures of the Cape Fold Belt, constitute reactivated thrust faults that formed during the Cape Orogeny in the Permian and Triassic (e.g., Lock et al., 1975; Dingle et al., 1983). The faults created accommodation space into which fluvial, lacustrine and marine sediments were deposited within the newly formed complex grabens, half grabens and horst structures from the Middle Jurassic onwards. Concomitant with the rift sedimentation, rift-related volcanic activity also took place particularly in the early stages of basin development (Koopmann et al., 2014; Marsh, 2016; Muir and Bordy, 2016). The sedimentary units preserved in the onshore rift basins have continental, transitional and marine rock equivalents in the offshore, hydrocarbon producing areas, which collectively are referred to as the Outeniqua Basin (Fig. 1.2A; e.g., Shone, 1976, 1978; 2006; McLachlan and McMillan, 1976).

The Oudtshoorn Basin (Fig. 1.1B) is part of the rift basin segment that stretches from Worcester in the northwest to Gamtoos Basin in the southeast (Fig. 1.1A). Bounded to the north by the steeply southward-dipping Kango Fault (which is part of the Oudtshoorn/Gamtoos Fault line), the Oudtshoorn Basin has been identified as a half graben, with depositional gradients possibly maintained by fault activity (Du Preez, 1944; Lock et al., 1975, Dingle et al., 1983; Al-Farraj and Harvey, 2005; Holzförster, 2007). The Oudtshoorn Basin is filled by exclusively continental rocks of the Uitenhage Group (Enon and Kirkwood Formations in the lower part and the informal Buffelskloof Formation in the upper part; see next section; Fig. 1.2A; Viljoen, 1992; Muir et al., 2017a). In the south, the basin fill unconformably overlies the Palaeozoic Cape Supergroup, whereas in the north, the basin fill is bound by the Kango Fault (e.g., Du Preez, 1944; Lock et al., 1975; Dingle et al., 1983; Holzförster, 2007).

1.3.2 Stratigraphy of the of the Uitenhage Group

Throughout the southern Cape region (Figs. 1.1, 1.2), the lowermost unit of the Uitenhage Group, the Middle Jurassic Enon Formation (EF), comprises conglomerates and subordinate sandy facies interpreted as alluvial fan and debris flow deposits representing high energy depositional events

(Dingle et al., 1983; Muir et al., 2017a, b; Muir and Bordy, 2016). Localized facies variations in the conglomerate-dominated units bear local names: e.g., Robberg Formation (Plettenberg-Knysna area), the informal Buffelskloof Formation. The overlying Middle Jurassic-Upper Cretaceous Kirkwood Formation (KF) is important, amongst others, for its plant and dinosaur fossil record (e.g., McLachlan and McMillan, 1976; de Klerk, 2008; McPhee et al., 2016; Muir et al., 2015, 2017b), and has been interpreted as sediments of distal fans and axial meandering fluvial systems (e.g., Lock et al., 1975; Shone, 1978; 2006; Muir et al., 2015). The KF has a gradual and interfingering relationship with the underlying EF (Lock et al., 1975; Dingle, 1973; Dingle et al., 1983; McLachlan and McMillan, 1975; McMillan et al., 1997; Muir et al., 2017b). The Colchester and Bethelsdorp Members (Tithonian) comprise estuarine and marine facies within the KF, respectively, and occur locally in the Algoa Basin (McMillan et al., 1997; Muir et al., 2017b for a recent review). Finally, the Aptian-Albian Sundays River Formation is the uppermost unit of the Uitenhage Group (Dingle et al., 1983), and based on its sedimentary characteristics and fossil invertebrate fauna, its depositional setting has been reconstructed as an estuarine to shallow marine. For a more detailed description of the stratigraphy of the Uitenhage Group, the reader is referred to Dingle et al. (1973), Dingle et al. (1983), Shone (1978, 2006), McMillan et al. (1997) as well as Muir et al. (2015, 2017a, b).

Within the Oudtshoorn Basin, conglomerates of the Jurassic-Cretaceous Uitenhage Group are exposed in a series of road cuttings and natural exposures. The conglomerates and breccias, which form part of the Enon and informal Buffelskloof Formations, are crudely bedded or massive, often clast-supported and moderately-to-poorly sorted with clast sizes ranging from a few mm to boulders (Du Preez, 1944; Lock et al., 1975; Holzförster, 2007; Muir et al., 2017a; Richardson et al., 2017). In the Oudtshoorn Basin, the sandstone-dominated Kirkwood Formation is not as fossiliferous as in the neighbouring Algoa Basin, however two fossil discoveries by Broom in 1927 and Hoffman in 1966 were identified of sauropod fossil material (de Klerk, 2008). Abundant silicified plant material in channel bars have been noted in this study.

The stratigraphic relationship in the basin fill and suggested evolution models for the Oudtshoorn Basin were undertaken in a few, preliminary studies to date. The first facies study, carried out by Du Preez (1944), identified a conformable succession that was subdivided into four units: Lower

Red Enon Conglomerates, Small Pebble Conglomerate, Enon Sandstone and Upper Red Beds (Fig. 1.2B). Lock et al. (1975) and Lock (1978) disagreed with this classification and proposed that the asymmetrical basin fill is characterized by interfingering facies units. A more recent contribution from Holzförster (2007) identified the basin an asymmetric, half graben that was filled from the north by mountain-front gravity flow fans, and telescopic mountain-front fans and rivers from the south. This author also concluded that sedimentation was controlled mainly by intermittent allogenic forces (tectonism). Climatic influences on sedimentation, based on geochemical and petrographic analysis, are comparable to those occur under arid climates with prevalent oxidation and torrential storm events (Du Preez, 1944; Lock et al., 1975). Based on paleocurrent studies and stratigraphic considerations, Lock et al. (1975) speculated that the Oudtshoorn Basin and the adjacent basins to the east (Fig. 1.1A) might have been connected via a fluvial system, which drained the basins to the sea that was east of the Gamtoos Basin at the time. This east flowing river system transferred sediment from the Cape Fold Belt mountains in the west out to sea in the east. A recent study by Richardson et al. (2017), integrating cosmogenetic dating with geomorphological and sedimentological data from southern Africa and the Falkland region, see.sm to confirm this large-scale sediment transfer system as it revealed that for the past 145 Ma extensive drainage systems connected these basins to the sea, depositing sediments sourced in the Cape Fold Belt hinterland that was several 100s' of km upstream from the final sink, the Falkland Plateau.

Due to the lack of sedimentological, stratigraphic and basin formation/evolution studies, chronostratigraphic and lithostratigraphic schemes are lacking for the Oudtshoorn Basin. Some attempts based on the few facies studies and structural inferences (e.g., Holzförster, 2007; Muir et al., 2017a, b) have concluded that the stratigraphic relationship between the Enon and Kirkwood Formations established in other parts of the broader region stands in the Oudtshoorn Basin as well. However, very little has been published about the younger units. For example, the informal Buffelskloof Formation, is considered to share an angular unconformity with the underlying Kirkwood Formation, representing a different cycle and mode of sedimentation (Muir et al., 2017b; Viljoen, 1992), but this relationship has not been documented by systematic studies. A schematic cross-section of the Oudtshoorn Basin is reproduced in Figure 1.2.

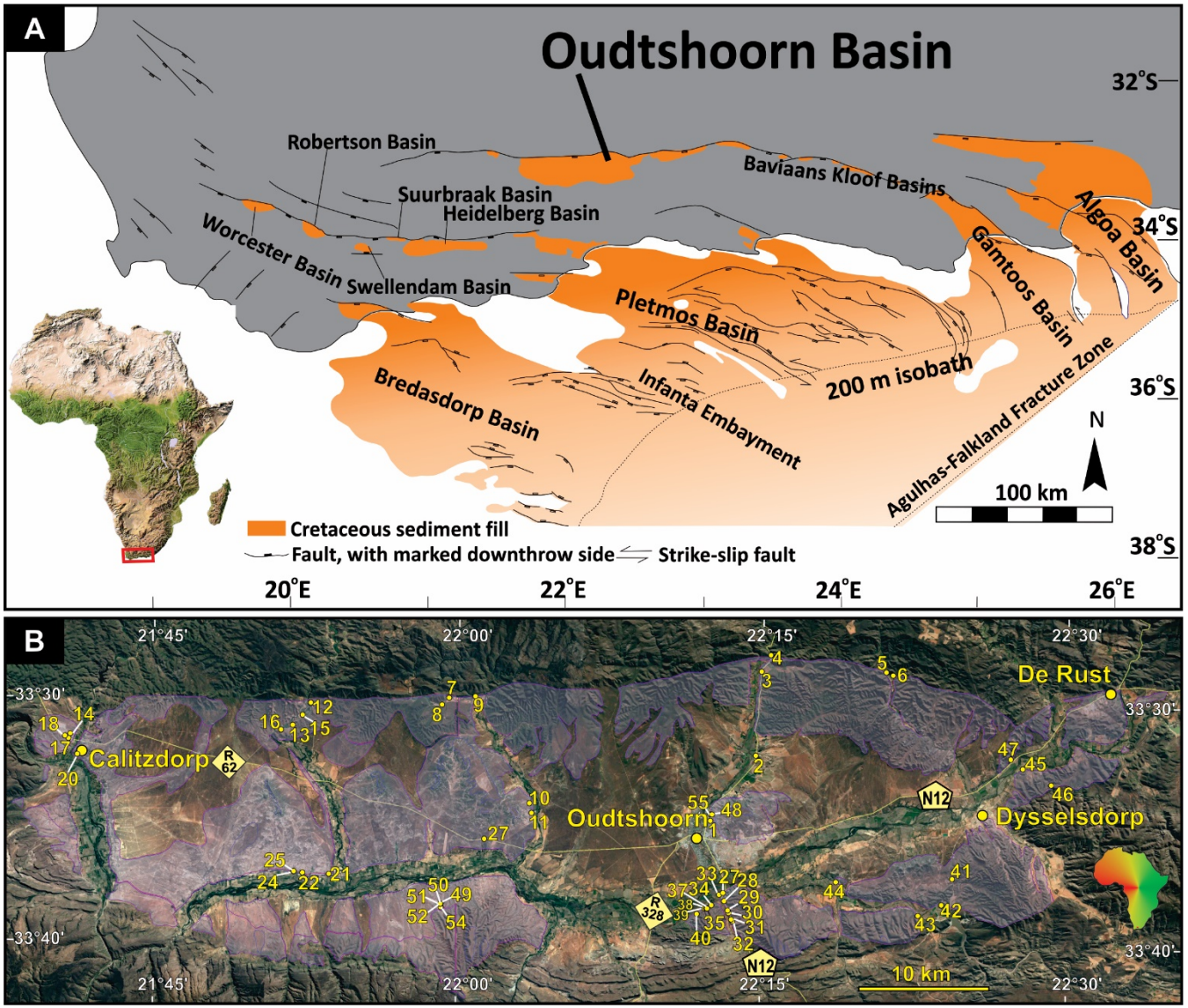

Figure 1.1. A: The location of the Oudtshoorn Basin within the other Mesozoic basins in the southern Cape region, South Africa. B: Map of the Oudtshoorn Basin and site localities from this study (numbers in yellow). Refer to Table 7.1 for corresponding site names and coordinates.

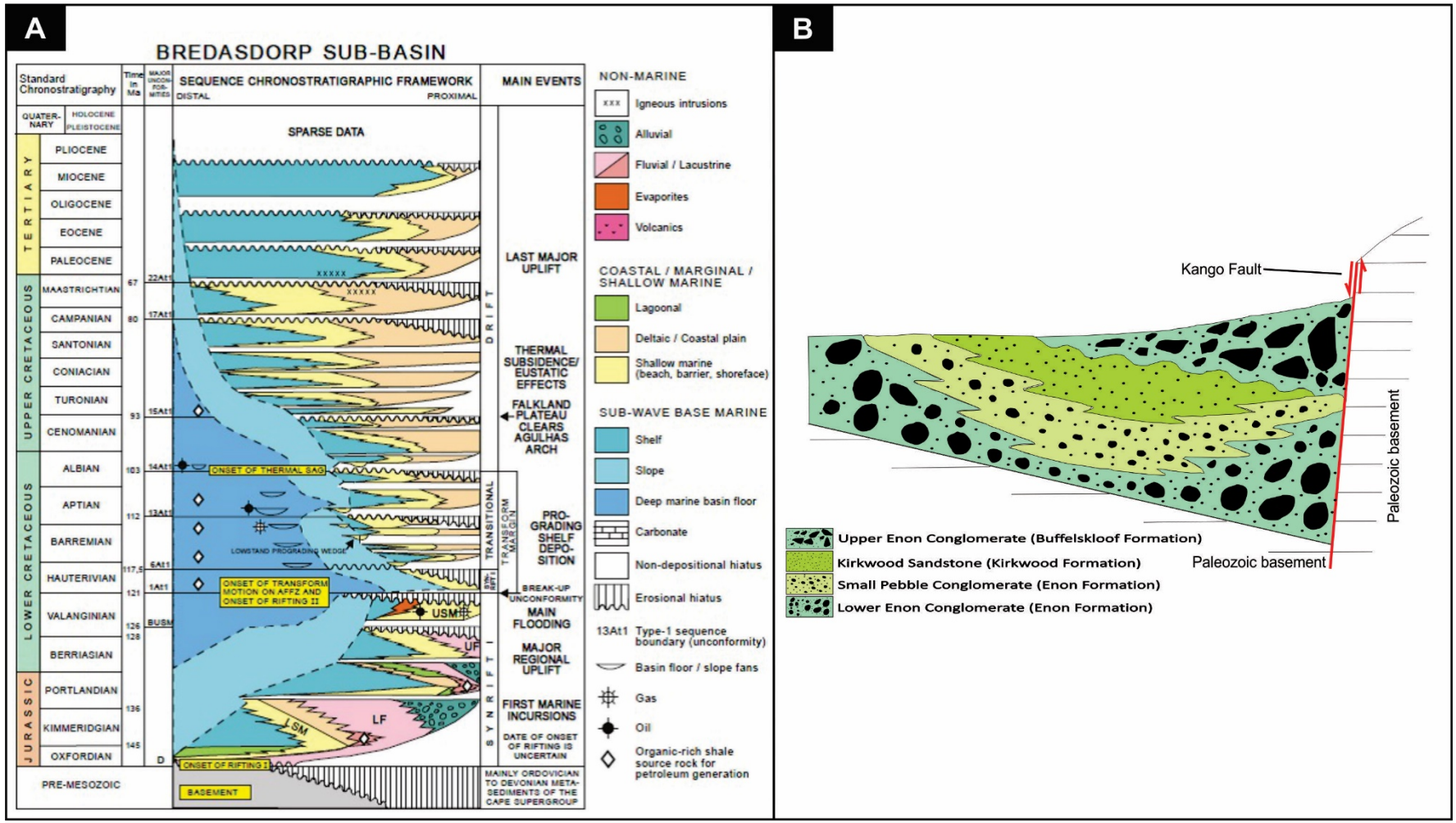

Figure 1.2. A: Generalised chronostratigraphy of the offshore Mesozoic Bredasdorp Basin, which contains units that are also preserved in the Oudtshoorn Basin (PASA, 2008). The geochronological ages of the onshore Mesozoic basins are being revised in more recent and ongoing studies (e.g., Marsh, 2016; Muir, 2018 in preparation). B: Schematic S-N cross-section of the Oudstshoorn Basin from Dingle et al. (1983) based on Du Preez (1944).

2. Methodology

Primary sedimentary structures result from specific sedimentary processes, which in turn reflect characteristic physical, chemical and biological conditions at the time of deposition (e.g., Nichols, 2009; Miall; 2013; 2016). With this principle in mind, in this project, the principles of sedimentary geology were applied to investigate the palaeoenvironment, sediment provenance (including the supply processes and source rocks) as well as palaeoclimate during the deposition of the sediments in the Oudtshoorn Basin. This integrated, multiproxy approach, which ultimately is aimed at assessing the early stages of basin evolution, consisted in the investigation of the following:

1. Qualitative and semi-quantitative sedimentary facies and architecture for the interpretation of depositional processes and environments;
2. Textural properties of gravelly facies (conglomerates, breccias) for the interpretation of provenance and the energy levels during deposition ;
3. Rock fabric indicators, predominantly clast imbrication for palaeocurrent patterns assessment;
4. Geochemical properties of the finer grained sediments for provenance and palaeoclimate interpretations.

2.1. Sedimentary facies analysis

Sedimentary facies are genetic units occurring as 3D rock products of specific sedimentary processes, and hence provide an understanding of the depositional processes and their respective spacio-temporal dynamics. The conceptual framework for sedimentary facies analysis in this study is adapted primarily from works by Hooke (1967), Allen (1983), Costa (1984), Shultz (1984), Miall (1985; 1988), Brierley et al. (1993), Liu and Cui (1999), Benvenuti (2002) and Colombera et al. (2013). This methodology, rigorously discussed by Miall (1985; 1988; 2013; 2016) follows a hierarchical approach to the analysis of sedimentary architectures, based on the scale and geometry

of bounding surfaces and the sedimentary facies packages enclosed therein (Table 2.1). The importance of bounding surfaces resides on their use as a proxy in establishing facies relationships and the respective hierarchies, representing broad physical and time scales (Miall, 1988; 2013). However, outcrop exposure and accessibility in the Oudtshoorn Basin allow mostly for 2-D field analysis with a good degree of vertical but poor lateral resolution, and thus bounding surfaces at the different scales could not be systematically classified in this study. In spite of the outcrop limitation, the first order data (low ranking features in Fig. 2.1A) such as grain/clast size, clast shape/roundness, clast-matrix ratio and primary sedimentary structures (e.g., cross-bedding in Fig. 2.1B) were documented in abundance, especially at sites indicated in the existing facies maps of Du Preez (1944) and modified by Holzförster (2007). The first order characteristics constitute important variables for considerations of flow type and energy, fluid density, fluid-particle ratios, etc. (e.g., Hooke, 1967; Costa, 1984; Shultz, 1984; Brierley et al., 1993; Liu and Cui, 1999; Miall, 2016). In addition, the following lithological characteristics were also documented in the field: rock type and colour; clast composition; palaeocurrent indicators; vertical and lateral geometry of lithological units; fossil occurrence; post-depositional features (i.e., structural deformation, attitude of strata).

From these first order data, sedimentary facies associations or architectural elements were identified with the aid of photomosaics of the best quality outcrops. The use of photomosaics (and the outcrop facies maps that were derived from them) aid the description, representation and interpretation of sedimentary facies and their associations (Wizevich, 1992; Miall, 1988) (Fig. 2.1). Where possible, the relationship between palaeocurrent data, bounding surfaces and lithofacies was used in reconstructing the geometry of architectural elements.

Once the spatial relationships of the mesoscale geometries (Figs. 2.1A-B) were assessed, the depositional systems (Figs. 2.1A-B) could be reconstructed using methods explained in Miall (1985; 1988;; 2013), Brierley et al. (1993), Benvenuti (2003) and Colombera et al. (2013). This

standard method constitutes the basis of sedimentary facies analysis and is summarized in Figure 2.1.

Quantitative facies analysis is another method developed for the objective characterization of depositional systems, and requires the documentation of measurable physical sedimentary quantities and their statistical analysis. The works such as those of Gibling (2006) and Colombera et al. (2013) review the method in depth and are not repeated here. Because 3D exposure of sedimentary structures (e.g., ripple marks, trough and planar cross-bedding) and architectural elements (e.g., downstream vs. laterally accreted units), which aid in 3-D geometrical reconstruction are relatively rare in the Oudtshoorn Basin, this method was not applied in this study. For example, in outcrops inferred to be channel deposits, channel margins and/or channel amalgamation are very rarely observable. This prevents the meaningful application of the quantitative methodology in the analysis of the sedimentary architecture in the present study. However, a facies map was constructed based on visual estimations of the modal percentages of architectural elements at the visited outcrop localities (see details in the Results section).

Table 2.1. Relationship between the hierarchy of physical processes in fluvial depositional settings and the resulting bounding surface (after Miall, 1988; 2014). See Fig. 2.1. for a graphical illustration of the bounding surfaces.

Hierarchy and significance of boundary		Physical processes
1st order	Encloses individual cross-bedded sets.	Migration of a train of similar bedforms under steady flow.
2nd order	Encloses co-sets of contrasting set types.	Contrasting lithofacies type in response to short term change in hydrodynamic conditions
3rd order	Low-angle cross-cutting erosion surfaces within co-sets or groups of co-sets.	Record changes in bedform orientation related to mid-term changes in hydrodynamic flow conditions by stage fluctuation or shift in flow
4th order	Low angle boundary, enclosing units of discrete accretionary coherence.	Reorganization of flow stability (e.g. during flood event), resulting in shift of bar or subordinate channel pattern.
5th order	Laterally extensive, may be erosional. Clear shift in lithology, bedform scale, etc.	Channel shift and erosion, recording channel migration and associated cut-and-fill erosion. Channel cutbanks may not be preserved.
6th order	Define discrete mappable stratigraphic facies divisions (e.g. major meander belts, palaeovalleys, etc).	Major change in fluvial regime/pulses. May record changes in base level, tectonic and/or climate regimes.

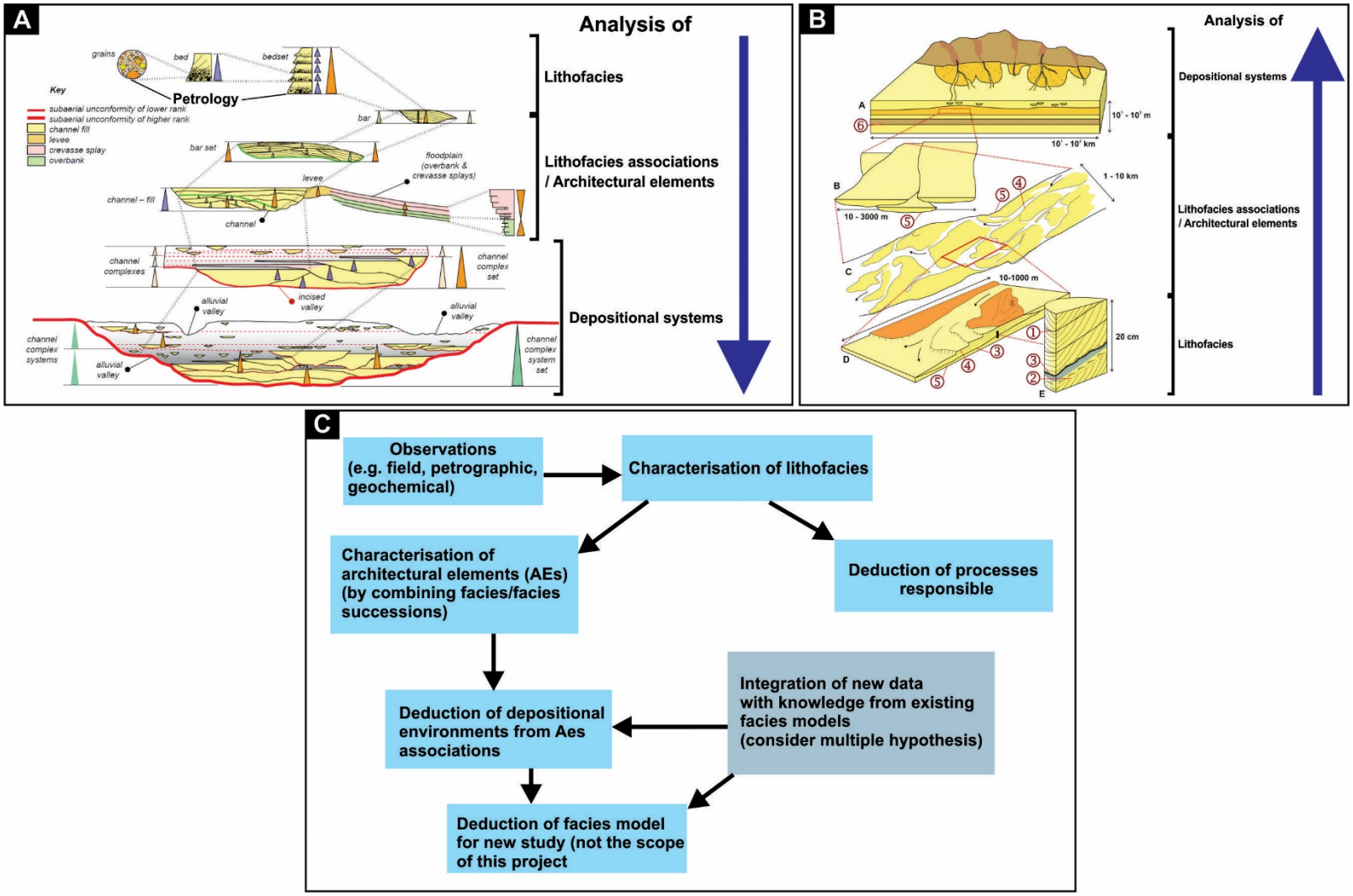

Figure 2.1. Hierarchy and physical scales of fluvial facies architecture (A) and bounding surfaces (B). Arrows show direction of increasing hierarchy. Numbers in B represent bounding surfaces explained in Table 2.1 (modified after Miall, 2014). B: workflow chart of the methodology followed in this project for facies analysis (modified after Walker, 1984 and Miall, 2014).

2.2. Petrographic analysis

The investigation of clast/grain composition, size and textural relationships of the studied sedimentary rocks (in conjunction with facies analysis) allowed an insight into the source rock geology as well as nature of the sediment transport and depositional processes (Ingersoll et al., 1984; Dickinson, 1985; Cox and Lowe, 1995; Bordy et al., 2016; Garzanti et al., 2010; Lindsey et al., 2007).

Petrological studies (with the aid of Folk, 1980) were carried out at macroscopic and microscopic scales for the coarse- and fine-grained lithofacies, respectively. For conglomerates and breccias, clast count yielded direct and specific information in the field regarding sediment source type, proximity and hydrodynamic processes during transport and deposition (Lindsey et al., 2007; Bordy et al., 2016). Clast count can also be used for assessing stratigraphic trends, fluvial channel depth estimations, comparison of multiple source terranes and for the study of fault offsets (e.g. Howard, 1993; Bordy et al., 2016). For this study, a simple semi-quantitative analysis was carried out primarily for the analysis of provenance and relative energy conditions during transport and deposition. More than 3000 clasts were counted and assessed for long axis length (and assessed using the classification scheme in Table 2.2), composition and roundness. In outcrops exposing strongly cemented gravelly facies, a full 3-D assessment of the clasts was not possible, and thus the longest visible clast axes were measured. To ensure maximum random selection of clasts, counts were done along horizontal transects of varied lengths, which depended on the length of the exposure of the facies of interest. A minimum of 150 gravel-sized (particle diameters > 2 mm) clasts per outcrop was recorded, a number considered to be statistically robust for the purpose of this study. An attempt was made to obtain as many vertically stacked and equally spaced transects as possible to account for changes in the clast properties though time and space (Howard, 1993). The data has been statistically analysed and presented graphically by means of volume and histogram plots (see Results section).

Optical microscopy is a standard semi-quantitative technique for the assessment of mineralogy and textural characteristics of sandstones. The direct observation of detrital modal composition, grain size and shape, sorting, grain to matrix ratio, cement type and alteration allows for inferences on the provenance of the sandstone samples. Using a transmitted light petrographic microscope, 30 µm thin sections and a point counter, petrographic analysis of the sand grains (particle diameters ranging from 0.0625 to 2 mm) was carried in conjunction with the Gazzi-Dickinson point counting method (Ingersoll et al., 1984; Dickinson, 1985). For statistically robust results, a total of 300 grains were counted in each sandstone sample. The modal composition data are shown in ternary diagrams of quartz-feldspar-lithic fragments (QFL), which were used for the classification of the sandstones and inferences about sediment provenance (see Results section). Coupling of QFL plots with qualitative observations of other petrographic data (e.g., grain angularity, average grain size and matrix content) allowed for a more complete characterization of the sandstones.

Table 2.2. Clast size categories of gravelly sediments applied in this study (modified after the standard Udden-Wentworth clast size classification scheme).

Granules and small pebbles	Medium pebbles	Coarse pebbles	Very coarse pebbles	Small cobbles	Large cobbles	Small boulders	Large boulders
0.2 - 0.8 cm	0.8 - 1.6 cm	1.6 – 3.2 cm	3.2 – 6.4 cm	6.4 – 12.8 cm	12.8 – 25.6 cm	25.6 – 51.2 cm	>51.2. cm

2.3. Palaeocurrent Analysis

Palaeocurrent indicators are primary sedimentary structures and fabrics used to estimate the direction of flow at the time of deposition. In conjunction with petrographic studies and facies analysis, palaeocurrent analysis aids in reconstructing the geometry of architectural elements, in the analysis of sediment source, dispersal patterns and gradient of the palaeoslope, resulting therefore in palaeogeographical and palaeotectonic assessments of a sedimentary basin (Potter and Pettijohn, 1963; Nichols, 2009; Yagishita, 1997; Miall, 2016). Data which can be extracted include geometry and azimuths of: cross-bedding, clast imbrication, observable channel scours and margins and azimuths of fossil debris.

Clast imbrication in coarse-grained facies is the most abundant and reliable palaeocurrent indicator in this study due the outcrop quality in the basin. However, dip direction of foresets in cross-bedded strata and long axes of coarse-grained plant debris (measuring up to 20 cm) were also noted wherever rock exposure allowed. The high reliability of clast imbrication (especially of boulders) as palaeocurrent indicators is not only because it is more readily measurable, but also because gravel size clasts represent flow conditions during high energy or peak fluvial discharge events (e.g., Costa, 1983; 1984; Potter and Pettijohn, 1963; Yagishita, 1997).

During imbrication measurements, the orientation of the a-b plane (Potter and Pettijohn, 1963) of preferably rod or disk-shaped clasts was recorded, and the data has been displayed in rose diagrams. The clast imbrication readings range from 3 to 109 per locality, and were determined by the quality of the outcrop. The rose diagrams and corresponding statistical parameters were derived using the ROSE.NET software, with 15^0 class interval. Correction for tectonic tilt was performed for tilted strata, by rotating the a-b plane dip about the strike through an angle equal to the dip of the bedding planes, assuming original horizontality (Potter and Pettijonh, 1963). However, correction for possible rotation about a vertical axis was not possible, due to absence of reference strata at the sites visited; it is therefore assumed that such rotation was minimal or non-existent.

2.4. Sedimentary geochemistry

Whole rock geochemical and mineralogical analysis is a valuable tool for constraining composition of sedimentary detritus, which in turn helps assessing the sediment provenance, tectonic setting, and palaeoclimate (Table 2.3), especially if the geochemical results are integrated with petrographic studies (e.g.,; Nesbitt and Young, 1982; Singer, 1984; Roser and Korsch, 1988; McLennan et al., 1993; Roser et al., 1996; Cox and Lowe, 1995; Cox et al., 1995; Goldberg and Humayun; 2010; Shao et al., 2012).

Sedimentary detritus undergoes physical and chemical changes from source to sink (Weltje and von Eynatten, 2004). For instance, at the source, alterations are due to erosion (mechanical breakdown) and chemical weathering, during the transportation processes are due to attrition, size-

selection, dissolution, etc. and at the site of deposition they occur because of diagenetic (burial) changes. Collectively these alterations define the final geochemical and mineralogical makeup of the sedimentary rock, and although the processes are complex, they can be assessed to some degree semi-qualitatively and semi-quantitatively using, among others, X-Ray spectroscopy (Cox et al., 1995; Garzanti et al., 2010; McLennan et al., 1993; Nesbitt and Young, 1982).

In this project, sandstone and mudstone samples collected in the field were crushed and milled using a jaw crusher and swing mill. Powder samples were then submitted for semi-quantitative and qualitative XRF and XRD analysis, respectively in the Department of Geological Sciences at the University of Cape Town. The sample preparation procedures are described in the Appendix. The geochemical samples were collected from the spatially isolated outcrops of specific facies occurrences within the basin, however the spatiotemporal relationship (i.e., stratigraphic correlation) of the samples is not possible because regional litho-, bio- or chronostratigraphic markers are absent in the Oudtshoorn Basin.

Table 2.3. Assessment of sedimentary processes and provenance based on petrological and geochemical data (modified from McLennan et al., 1993).

Sedimentary Processes /Provenance	Petrographic character	Geochemical character
Weathering (indirect measure of palaeoclimate)	Ambiguous. Some mineralogical effects (e.g. feldspar/clay ratios)	Possible to quantify in favourable conditions. Major elements (CIA). Rb/Sr (also Sr isotopes)
Sorting	Textural maturity, heavy mineral content and variety	Major elements (Si/Al). Quantity heavy mineral fractionation such as zircon (Zr, Hf) and monazite (REE)
Sedimentary recycling	Quartz content/ textural properties; sedimentary rock fragments	Various geochemical approaches (CIA, Zr, Hf, Th/U); Nd-isotopes
Diagenesis	Relative chronology and mineral reactions. Overgrowth, albitization, smectite/illite transformation	Potential but few studies. Major elements (CIA), redox elements (e.g. Fe^{3+}/Fe^{2+}), various isotopes (Rb/Sr, U/Pb)
Rock types in the source area	Rock fragments; quartz morphology	Little or no direct information
Terrane type in the source area	QFL (continental block, magmatic arc, recycled orogen)	Combined trace element/Nd-isotopes (Old Upper Crust, Young Differentiated Arc, Young Undifferentiated Arc)
Terrane identification	Little or no direct information	Pb isotopic composition of feldspars and whole rocks
Age of source rocks	Relative age of components in mean age in favourable circumstances	Mean age (Nd-model ages); favourable circumstances component ages (U/Pb ages of zircon, quartz, etc.)
Crust/mantle character	Little or no information	Nature of crust/mantle melting (Eu-anomalies, HREE-depletion). Nature of crust/mantle sources (Th/U, μ)

2.4.1. X-Ray fluorescence

X-Ray fluorescence is a standard technique and is routinely used for determining the bulk chemical composition of rock samples (Loubster and Verryn, 2008, McLennan et al., 1993). For major element analysis, powdered samples are used to make fluxed fusion disks, which are then subjected to an X-Ray source beam. The interaction results in emitted fluorescent X-Rays from the target sample, which are then detected and analysed. Each emitted X-Ray energy is characteristic of a specific element (oxide phase, for the current study), and the X-Ray count of each energy is determined by the elemental abundances in the target sample (Willis et al., 2011; Norrish and Hutton, 1969). X-Ray fluorescence analysis was carried with a Panalytical Axios X-Ray fluorescence spectrometer.

The Harker plots of provenance (Roser and Korsch, 1986) represent a measure of K-feldspar and mica content versus plagioclase. The plot of K_2O/Al_2O_3 versus silica is used in this study correlatively with QFL detrital mode diagram for the analysis of provenance. The $Si0_2/Al_2O_3$ ratio is used to indicate sediment maturity, given that the physical and chemical resistance of quartz results in its enrichment relative to other minerals (oxides) (Bathia, 1983; McLennan et al., 1993, Roser at al., 1996).

The alteration of primary silicate minerals (e.g., feldspar, mica) into clays constitutes the basis for palaeoclimatic studies. Proxies such as the Chemical Index of Alteration (CIA) of Nesbitt and Young (1982) and the Index of Chemical Variation (ICV) of Cox et al. (1995) are used to investigate the amount of weathering undergone by the sediment. The Chemical Index of Alteration (CIA) is a weathering index widely used as an indirect palaeoclimatic indicator (Goldberg and Humayun, 2010; Bahlburg and Dobrzinski, 2011; Shao et al., 2012; Sciscio and Bordy, 2016). Under surface conditions, CIA measures the progressive depletion of easily weathered mineral phases, and enrichment of more stable phases such as illite and smectite. It is calculated as the ratio of relatively immobile Al_2O_3 to more mobile cations Na^+, K^+ and Ca^{2+}, as shown by Equation 1:

$$CIA = \left(\frac{Al_2O_3}{Al_2O_3+Na_2O+K_2O+CaO^*}\right) * 100 \quad , \qquad \text{(Equation 1)}$$

where CaO* represents the CaO content of silicate minerals only, and all oxides are given in weight percentages.

A more sensitive measure of weathering, the CIA_{molar} (Equation 2 below), was proposed by Goldberg and Humayun (2010) and is used as an aridity indicator. Its sensitivity is based on the molar proportions between Al_2O_3, alkalis and CaO, which is obtained by dividing the wt% of the oxide by its molar mass, such that elemental abundance is given stoichiometrically at atomic level (Goldberg and Humayun, 2010; Sciscio and Bordy, 2016).

$$CIA_{molar} = \left(\frac{Al_2O_{3(molar)}}{Na_2O_{(molar)}+K_2O_{(molar)}+CaO^*_{(molar)}}\right) \quad , \qquad \text{(Equation 2)}$$

In this study, carbonate-containing samples were adequately noted and not included in the calculations of CIA_{molar}.

The ICV (Equation 3 below) measures the proportion of alumina relative to the other major oxides excluding silica, eliminating the effect of quartz dilution (Cox et al., 1995; Sciscio and Bordy, 2016). It shows a decreasing trend with increase in weathering of minerals: it is highest in less stable minerals such as pyroxenes and amphiboles, lower in alkali feldspars and lowest in kaolinite (Cox et al., 1995). Furthermore, inferences about relative tectonic activity are also possible assuming that the compositional maturity of sediments is greater in tectonically passive settings, hence yielding lower values of the index relative to tectonically active regions (Cox et al., 1995). Conversely, the CIA increases with increasing sediment maturity and prevalence of clay minerals (Nesbitt and Young 1982), a relationship which can be used as complementary between the two proxies. The ICV is calculated using the following equation:

$$ICV = \left(\frac{Fe_2O_3+K_2O+Na_2O+CaO+MgO+MnO+TiO_2}{Al_2O_3}\right) \quad , \qquad \text{(Equation 3)}$$

2.4.2. X-Ray diffraction

The X-Ray Powder Diffraction is an important and widely available laboratory X-Ray spectroscopy technique used in determining the crystalline phases in rock samples (Hillier, 2003; Loubster and Verryn, 2008; Singer, 1984). The main difference to XRF is the use of diffraction patterns generated by a sample in XRD, which are unique for every crystalline phase. The sample is subjected to X-Ray from a source cathode ray tube and the interaction between the incident X-Ray and the sample results in diffracted rays if conditions satisfy Bragg's Law (Equation 4, below). The sample is scanned though a range of 2-theta angles and the diffracted rays are detected and counted. Using Equation 4, the d-spacings can then be determined from each diffraction pattern, and the crystalline phase thus identified.

$$n\lambda = 2d\sin\theta, \qquad \text{(Equation 4)}$$

where: "λ" is the X-Ray wavelength, "d" is the interplanar spacing of multiple "n" of the lattice, "θ" is the Bragg angle (X-Ray angle of incidence).

For the scope of this study, XRD qualitative analysis was performed using a Phillips PW 1390 X-Ray Diffractometer on randomly oriented clay samples for the identification of their crystalline phases, given that clay mineralogy can complement in palaeoclimatic analysis (Singer, 1984, Chaudhri and Singh, 2012).

Clay fractions were separated from mudstone samples only, as sandstone samples did not yield sufficient amounts of clay. Fraction analysis increases resolution and the intensity of diffraction (Hillier, 2003). Clay-sized particles were separated by wet sieving, suspended on glass slides and dried at room temperature before analysis (Hillier, 2003). Sample preparation is described in more detail in the Appendix.

3. Results

3.1 Lithofacies analysis

The fluvial deposits of the Middle to Late Mesozoic Uitenhage Group in the Oudtshoorn Basin can be grouped into four lithology groups as explained in the following sections. Twenty-two lithofacies and nine facies associations have been identified in this study. Architectural Elements are the 3-D association of lithofacies (i.e., lithofacies associations), which have been generated under specific depositional conditions (Miall 1988; 2016; see Methods section). Lithofacies and architectural elements are described in detail in Table 3.1 and Table 3.2, respectively, and are illustrated in the figures of this section. It is important to note again that it is not possible to assess with certainty the stratigraphic relationships (i.e., correlation) among the lithofacies associations and all other results reported in this chapter (e.g., clast size, composition, palaeocurrents) due to the lack of stratigraphic markers within the Oudtshoorn Basin. Therefore, any spatial trends, or their lack thereof, shown on any of the maps of this chapter need to be carefully interpreted (see Discussion section).

3.1.1. Gravelly facies (facies code G-1 and G-2)

Conglomerates and breccias are the main lithological components of the gravelly facies (Table 3.1) and are primarily found along or close to the modern-day basin margins (Fig. 3.20). Distances between gravelly facies sites and the basin margins vary from a few tens of meters to a few hundreds of meters (e.g., Fig. 3.20; sites D12_S8 and D2_S1 in Fig. 1.1B). Weathering of these gravelly deposits typically results in the red and orange-brown colours of the rocks, often with a black surface coating probably caused by the abundance of ferrous minerals (Du Preez, 1944; Shone, 2006). Subdivisions within these facies are made based on textural properties (e.g., matrix content, clast roundness, average clast size; Table 3.1).

Conglomerates and breccias near the basin margins contain predominantly cobble and boulder-sized clasts (lithofacies G-1; Table 3.1; see section on Clast counts). Clast size ranges from 2 to 45 cm on average, and outliers of 60-100 cm in diameter are common (Fig. 3.1). The matrix is predominantly medium- to coarse-grained sandstone. Gravelly facies with angular clast (Figs. 3.1A-

D) are typically massive, very poorly to poorly sorted, clast- or matrix-supported. Crude bedding is only evident at large scale, where individual beds may attain thicknesses of up to 8 meters. Internally, these deposits are marked by localised variations in clast-matrix ratio and by clusters of clasts of comparable size, and are underlain by erosional surfaces that cut into the underlying sandstone layers (facies Sm/Smc and pebbly Sp; Fig. 3.4). Gravelly facies with increased clast roundness are usually crudely bedded (Figs. 3.1F, 3.5 and 3.6), and commonly contain imbrication and normal and reverse grading.

Gravelly facies away from the basin margins (Figs. 3.2A-G and K; Fig. 3.20; see section on Clast counts) are made up of pebble- and cobble-sized clasts and are mostly clast-supported. Here associations with lenses and ribbons of various sandy facies are common (e.g., Figs. 3.2D-E, 3.7 to 3.13). Internally, these facies may be massive or show localised grain size variation and sorting. Localised normal and reverse grading is common, and imbrication is abundant in some localities (Figs. 3.2E and F).

3.1.2. Sandy and fine-grained facies

Sandy facies (Table 3.1) are found in larger abundances in the centre of the basin (e.g., Figs. 3.14- 3.18 and 3.20). They occur as lenses, ribbons and sheets which often pinch out laterally. In association with conglomerates and breccias, basal boundaries are commonly sharp, non-erosive or gradational. Top boundaries are generally erosive and undulating. Interbedded successions with subordinate mudstones are common locally (see CH facies association code in the next section; Figs. 3.15 and 3.16). Subdivisions are based on grain size, sedimentary structures, composition, morphology and facies associations. Weathering causes colour change from grey, brown or cream to red and brown. Weathered units also tend to disintegrate easily and have porous texture, and often show hollow structures similar to those found in the conglomerates and breccias.

Fine-grained facies (code F; Table 3.1) occur mostly in the centre of the basin (Fig. 3.20) and are primarily associated with sandy facies (Figs. 3.15-3.19). Excessive scree cover in their exposures masks their external architecture. They are subdivided on the basis of sedimentary structures and fossil occurrence.

Table 3.1. Lithofacies in the fluvial deposits of the Middle to Late Mesozoic Oudtshoorn Basin. Conglomerates/breccias and clast-rich sandstones are differentiated by matrix percentage (>30% in the latter). Facies coding modified after Miall 1985, 1996 and Brierley et al., 1993).

Lithofacies code	Diagnostic characteristics	Inferred depositional processes and conditions
Gm-1; Gh-1 **(Fig. 3.1)**	Massive (Gm-1) or crudely bedded (Gh-1), clast- or matrix-supported (Gcm-1 or Gmm-1), very poorly-poorly sorted conglomerates and breccias. Long axis of clasts ranges from 2-70 cm, with outliers of 80-180cm. Very angular-rounded; rounded clasts can be spheroidal and discoidal in shape. Medium-coarse-very coarse-grained sandstone matrix. Normal and reverse grading is common. Typically occurs near the northern and southern margins of the basin.	- Hyperconcentrated and debris flows (breccia facies) with low to high-strength (variable clast content) or clast-rich debris flows (high strength) generated in very high energy, periodic and catastrophic events. - Traction currents (conglomerate facies) in very high energy, fast flows
Gm-2 **(Figs. 3.2A, C, D, G, K)**	Small boulder, pebble and cobble massive monomictic/polymictic conglomerates and breccias, mostly clast-supported (Gcm-2/Gmm-2). May form sheets, lenses or complex architecture associated with other lithofacies. Poorly-very well sorted. Very angular-well rounded; clasts tend to be more discoidal as roundness increases. Clast size range highly variable - seemingly related to proximity to basin margins and associated lithofacies, but typically 0.5-30 cm, with outliers of up to 50 cm. Imbrication and circling–flow structures (at boundary surface) are common.	- Longitudinal bedforms or gravelly bedload in very high energy, sediment laden currents either in confined channels or in unconfined, broad, shallow sheet-like flows.
Gi **(Figs. 3.1B, F, 3.2E-F)**	Imbricated boulder (Gi-1), gravel and cobble-sized (Gi-2) clasts, associated with Gcm-1, and Gcm-2 and Gh-2.	- Longitudinal bedforms or gravelly bedload in very high energy water current that was less sediment laden than those above.
Gt **(Fig. 3.6)**	Trough cross-bedded conglomerates, moderately sorted. Maximum clast size ~10-15 cm. Associated with Gm-2, Gp and sandy equivalents. May also occur at the base of Sm beds.	- Down-current migrating sinuous crested dunes/gravel bars in high to moderate energy water current that was confined to minor channels.
Gp **(Figs. 3.6 and 3.12)**	Planar (high and low angle) cross-bedded conglomerates, moderately sorted. Maximum grain size ~10cm. Common in crudely bedded Gh-1 sheets as thin lenses with subordinate Sp. Same association with Gm-2 and sometimes Gh-2.	- Transverse to down-current migrating straight crested dunes/gravel bars in high to moderate energy water current that was confined to minor channels.
Gh-2 **(Figs. 3.2A-C, E, and G)**	Horizontally bedded, normally and inversely graded, moderately sorted, ortho- (Gch) and paraconglomerates (Gmh). Commonly associated with coarse-grained Sm and Gm-2. Usually polymictic with very angular to subrounded clasts (maximum long axis: ~10 cm).	- Pebble stringers that accreted vertically in a gravel bar in high to moderate energy water current.
Sm, Scm **(Figs. 3.2D, E, F, G, J, K, L and 3.3B, C, D)**	Massive (Sm) and pebbly (Scm) sandstone with very fine-to very coarse grain sizes. In association with Gm-1/Gh-1, occur mostly as interbedded coarse-grained sandstone lenses or laterally continuous sheets, and may show basal circling-flow structures. Thin tabular, laterally continuous lenses in sandy facies. Pebble stringers and Gm-2 lenses are common associations. Form tabular laterally continuous beds and lenses in association with Fm and Fl facies. May contain rip up clasts as well as charcoal and bioturbation structures. Sm may contain fossils.	- When co-occurring with gravelly facies: Relatively rapid deposition ("dumping") at the end of a high energy event (e.g., winnowing of floods). - When co-occurring with fine grained facies: relatively short-lived, upper flow regime pulses of flow (may lead to antidunes) in a predominantly very low energy setting (e.g., crevasse splay on a floodplain) or bioturbation of previously laminated sandy sediments

		- Charcoal suggests wild fires (see Muir et al. 2015).
Facies code	**Diagnostic characteristics**	**Inferred depositional processes and conditions**
St/Sct, Sp **(Figs. 3.2J)**	Trough (St/Sct - pebbly) and planar (Sp) cross-bedded sandstone. Occur mostly as basal facies in coarse-grained sandy deposits with complex architecture and commonly associated with Sp, Sh ,Sm/Scm and as St-Sm-Sp. Also common as faint features at the base of sandy tabular sheets and lenses in the architectural element F.	- Down-current migration of sinuous (St) and straight (St) crested sand dunes in moderate energy water currents.
Sh **(Figs. 3.2H and M; 3.3B, C e E)**	Horizontally laminated (Sh) sandstone, typically medium-grained. May contain charcoal fragments (Fig. 3.3E) Associated with sandy and G-2 facies, occurring as sheets or lenses up to tens of meters long. Also found in tabular laterally continuous sandy beds or lenses engulfed in Fl/Fm deposits. May contain fossils.	- Vertical accretion of flat, thin sand sheets in plane-bed flow (upper to moderate flow conditions). - Charcoal suggests wild fires (see Muir et al. 2015).
Fl **(Figs. 3.3, 3.16 and 3.17)**	Laminated mudstone, mostly siltstones, with thin clay horizons (1-5 cm maximum recorded). Often interbedded with sandstone sheets and lenses; may overlie normally graded sandy sheet deposits.	- Settling from suspension under very low energy conditions.
Fm **(Figs. 3.3, 3.16 and 3.17)**	Massive mudstone, mostly siltstones. Often interbedded with sandstone sheets and lenses; may overlie normally graded sandy sheet deposits. It may contain locally bioturbation structures. B bentonite occurrences were also recorded.	- Massive structure might result from mud flows (mass movement deposits), however bioturbation of previously laminated suspension sediments is more likely.
Fp **(Fig. 3.3A)**	Mudstones with pedogenic carbonate nodules (rare), variegated colours and greenish-grey mottles in red mudstones.	- Post-depositional pedogenic alteration of fine-grained sediments.

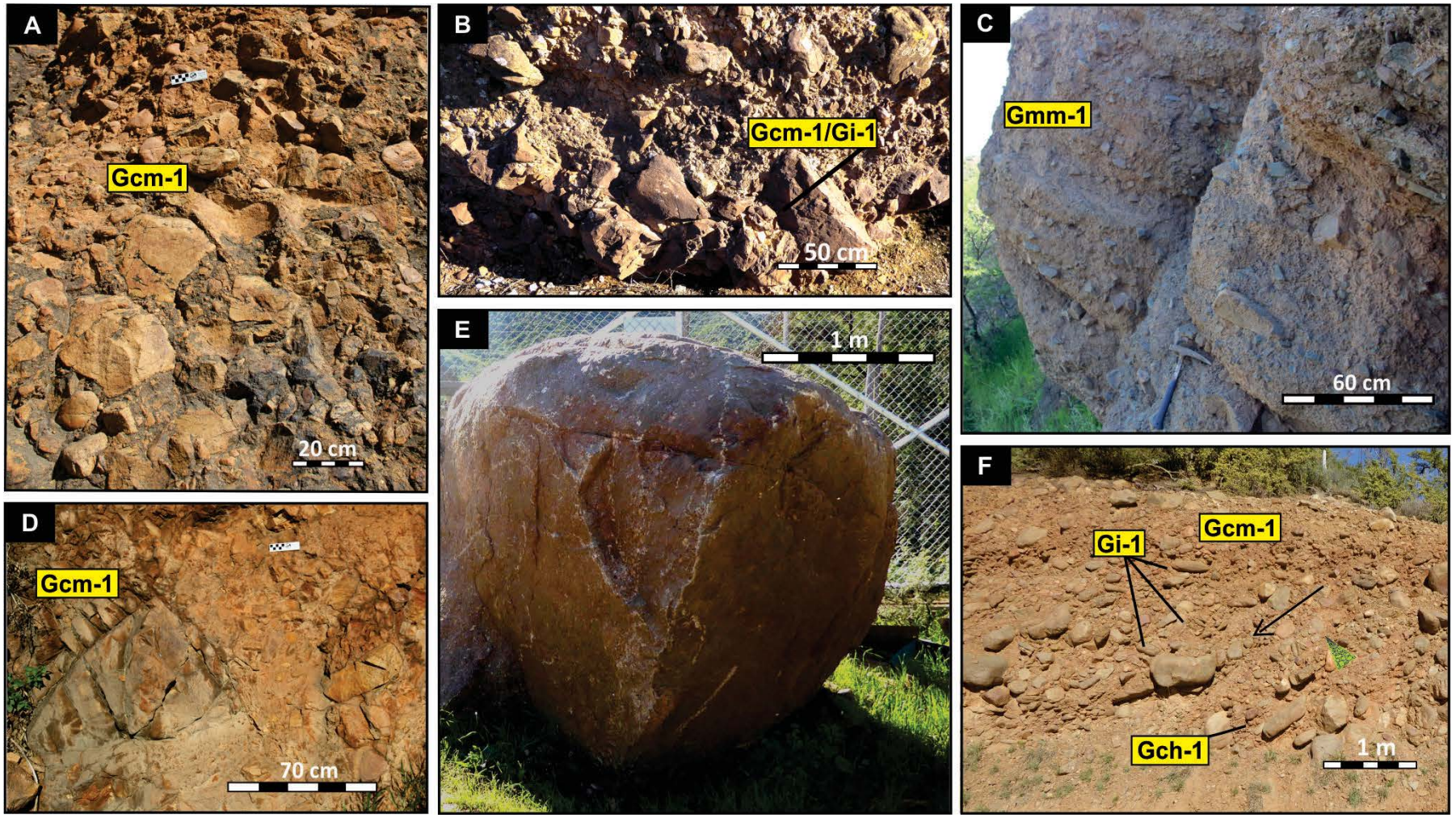

Figure 3.1. A: Crudely bedded facies Gcm-1 dipping towards fault scarp at ~25˚ at site D5_S1 near the northern basin margin B: Facies Gcm-1 and Gi-1 at site D12_S8 in the eastern part of the basin. Normal-to-inverse grading is also common here (Fig. 3.5). C: Crudely bedded facies Gmm-2 is dipping towards fault scarp at ~35˚ at site D3_S2. D: Crudely bedded facies Gmc-1 is dipping towards the fault scarp at site D2_S6 near the northern basin margin. E: Very large, rounded boulder probably originates from nearby architectural element D-2 at site D3_S3. F: Facies Gi-1, Gmc-1 and Ghc-1 at site D3_S3. Arrow indicates dip of crude bedding (~35˚). For detailed description and interpretation of the facies see Table 3.1; for site localities see Figure 1.1B.

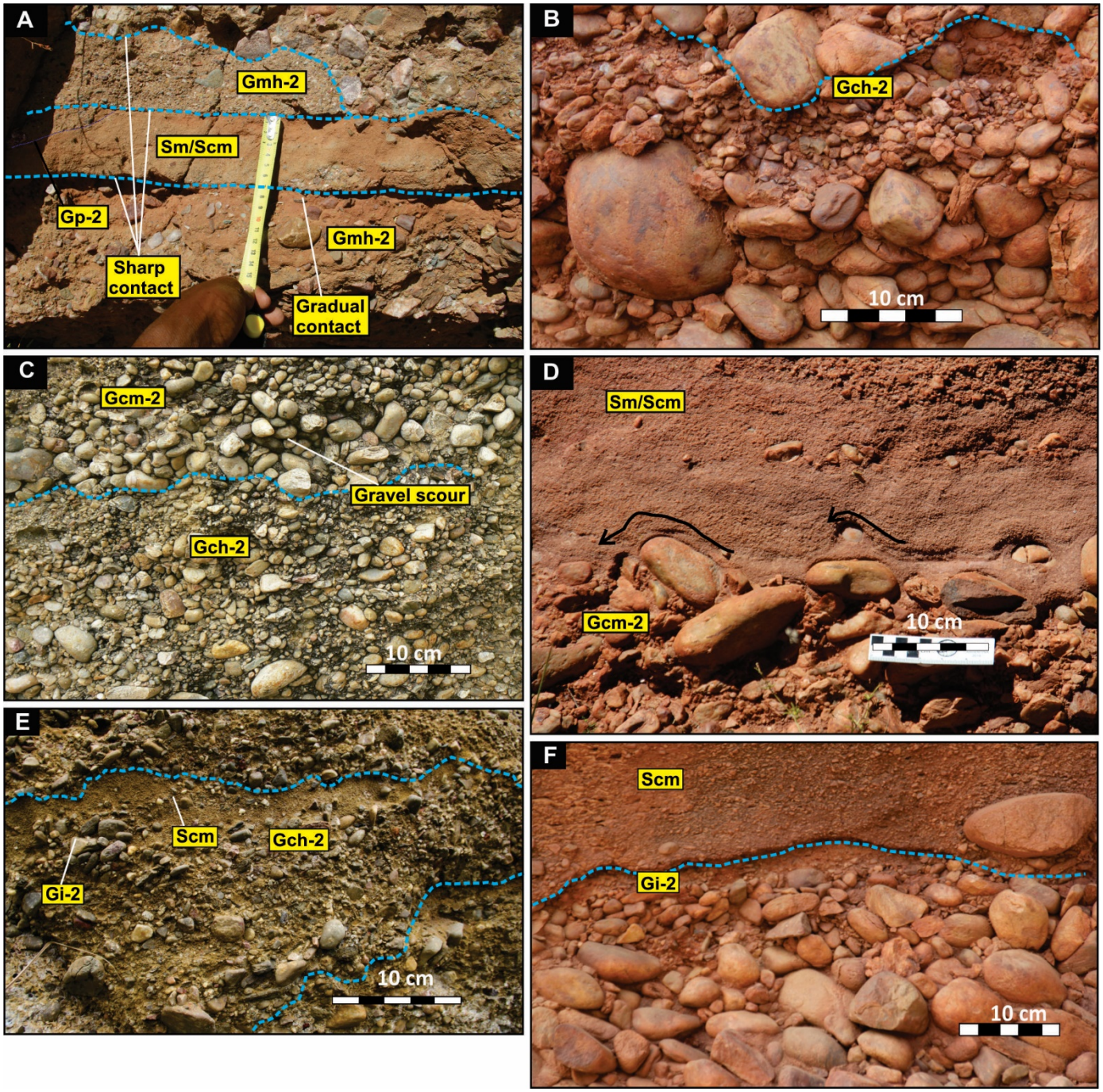

Figure 3.2. A: Breccia facies Ghm-2 and associated facies Sm/Smc and Gp-2 at site D5_S3 in the central-eastern part of the basin. B: Facies Ghc-2 at site D11_S1, close to the southern margin of the basin. C: Facies Gmc-2 and Ghc-2at site D13_S2. D: Association of facies Sm/Scm and Gmc-2 at site D9_S2. E: Facies associations Gi-2, Ghc-2 and Smc are common in conglomeratic GB at site D6_S4. F: Facies Gi-2 (here normal graded) and overlying facies Smc at site D11_S2 close to the southern basin margin. G: Facies Ghm-2 with normal and reverse grading and interbedded with facies Smc at site D8_S1 in the central-eastern part of the basin. H: Facies Sh and Sm/Sh in sheet-like beds are overlain by GB at site D17_S2. I: Facies Sp at site D8_S7. J: Facies Sm/Sh and basal St facies (faint with the overlying facies Sm/Sh and Sm form an overall upward coarsening succession at site D23_S3. K: Top view of facies Gmm-2 at site D23_S3. L: Facies Smc/Sp and Sm are normal graded at site D8_S7. M: Facies Sh and Smc at site D7_S2. For detailed description and interpretation of the facies see Table 3.1; for site localities see Figure 1.1B.

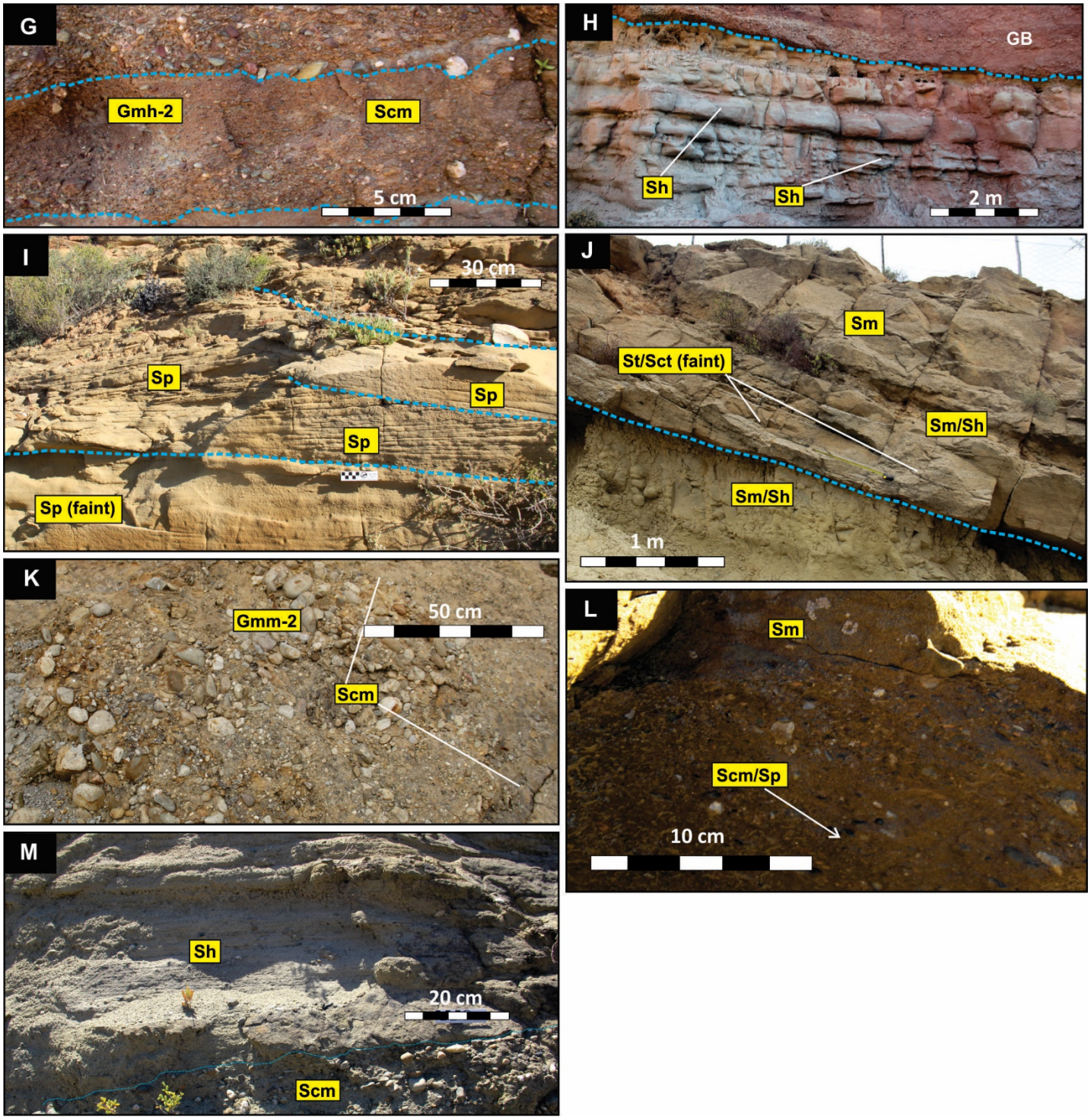

Figure 3.2 ctd. G: Facies Ghm-2 with normal and reverse grading and interbedded with facies Smc at site D8_S1 in the central-eastern part of the basin. H: Facies Sh and Sm/Sh in sheet-like beds are overlain by GB at site D17_S2. I: Facies Sp at site D8_S7. J: Facies Sm/Sh and basal St facies (faint with the overlying facies Sm/Sh and Sm form an overall upward coarsening succession at site D23_S3. K: Top view of facies Gmm-2 at site D23_S3. L: Facies Smc/Sp and Sm are normal graded at site D8_S7. M: Facies Sh and Smc at site D7_S2. For detailed description and interpretation of the facies see Table 3.1; for site localities see Figure 1.1B.

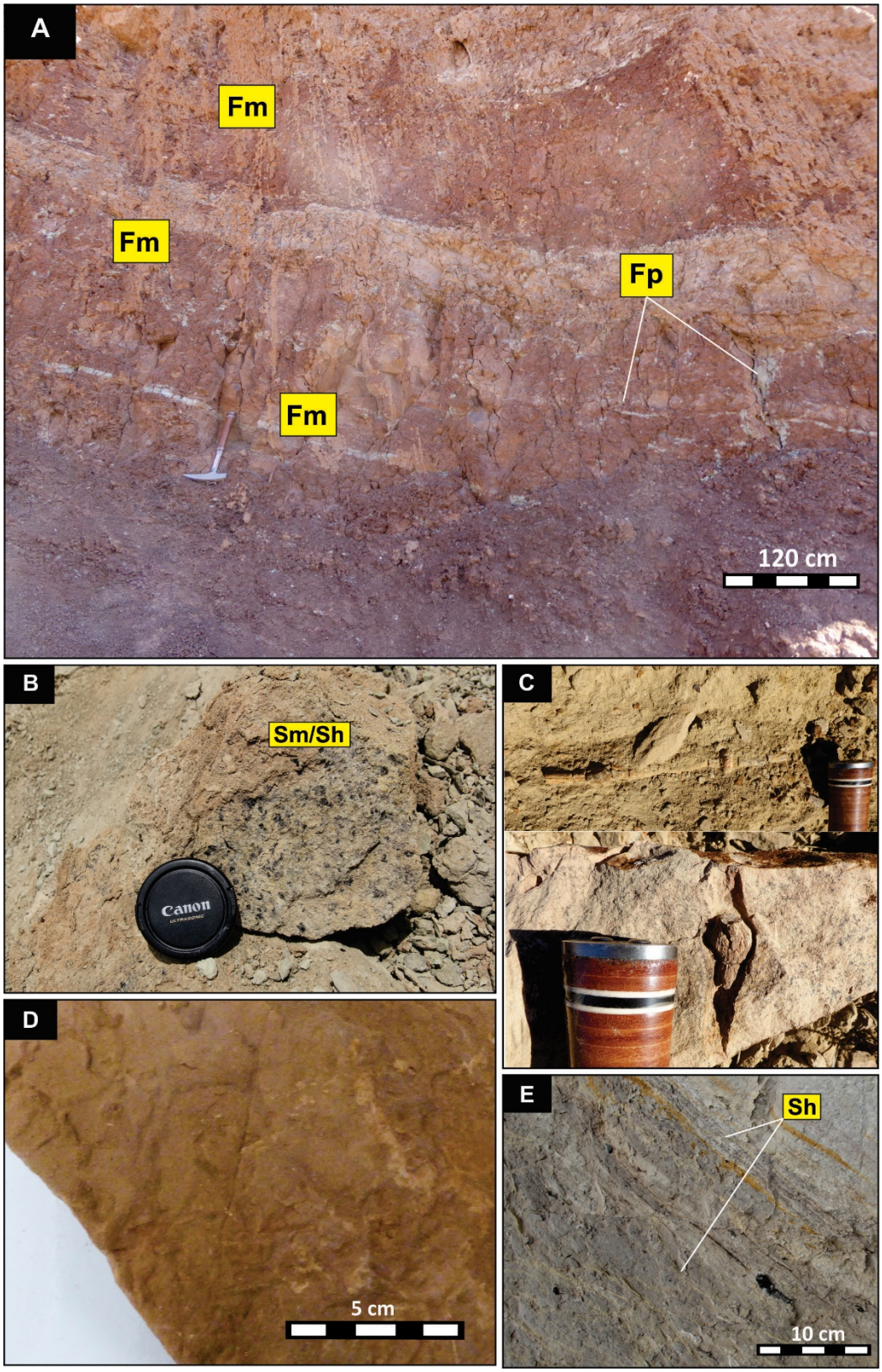

Figure 3.3. A: Facies Fp and Fm, which are interbedded with ribbons and lenses of architectural element CS at site D1_S2. B: Charcoal fragments in facies Sm/Sh at site D17_S2. Here, the charcoal-bearing sandstones are associated with GB and CH-1 deposits (Fig. 3.12). C: Fossil plant material in facies Sm and Sh at site D8_S7. D: Horizontal invertebrate burrows in facies Sm (element CS), which is interbedded with facies Sm, Sh and Gmm-2 (CS), at site D6_S1 (Fig. 7.2 in the Appendix). E: Charcoal laminations and charcoal fragments in facies Sh, which is part of co-ocurring SB- GB elemets at site D6_S4. For detailed description and interpretation of the facies see Table 3.1; for site localities see Figure 1.1B.

3.1.3 Facies associations

The facies described in Table 3.1 and shown in Figures 3.1 to 3.3 belong to nine facies associations (or architectural elements), which are detailed in Table 3.2. The distribution of the architectural elements in the Oudtshoorn Basin could not be mapped, because the studied outcrops are spatially isolated and lack stratigraphic markers. This meant that the stratigraphic relationship of the neighbouring outcrops (and by extension that of the architectural elements) is difficult to establish. As an example, there is no direct field evidence for contact relationships between sites D12_S8 (D-1, Fig. 3.4), D12_S6 (GB and SB, Fig. 3.9) and D12_S7 (D-2, Fig. 3.5; for site localities see Fig. 1.1B). However, using structural dips and their geographical proximity to each other (Fig. 3.20), it may be assumed that strata at site D12_S7 (dip 073/15N) stratigraphically underlies those at site D12_S6 (dip 060/30N), which is in turn overlain by site D12_S8 (dip 142/24N). Post-depositional normal faulting (Fig. 3.5) is common in the sites near the basin margin throughout the study area, with rotated, shattered clasts within the fault gauge.

Given the above, the best attempt to illustrate the spatial distribution of the facies associations is Figure 3.22, which shows the visual estimates of the abundance of the architectural elements within the studied outcrops. This suggests that outcrops with gravelly facies are common in outcrops close to the basin margins, whereas those with sandy sandy facies are more common in the centre of the basin. For example, architectural elements D-1 and D-2, which are dominated by lithofacies Gmm1, Gcm-1, Gh-1, and Gi-1 (e.g., Fig. 3.1, Figs. 3.4-3.6) and form very large, crudely bedded sheets or complex channelized deposits (Figs. 3.4 to 3.6), are common in basin margin sites: D2_S1, D2_S6, D3_S2, D3_S3, D5_S1, D12_S7 and D12_S8 (for site localities see Fig. 1.1B). Architectural element GS (e.g., Figs 3.7, 3.8 and 3.10) occurs in the centre, southwest and west of the basin (Fig. 3.20) and may be associated with architectural elements CH-2, F and CS (e.g., Figs. 3.11 and 3.14), where it is characterised by facies Gmc-2 and Gmm-2 (most common) and subordinate facies Sm and Scm. It occurs as three main geometries: 1. highly stratified pebbly breccia sheets associated with sandy lens facies (Figs. 3.2A and 3.7, west of the basin – see Fig. 3.22); 2. massive and imbricated pebble-cobble conglomerate sheets associated with sandy beds (Fig. 3.10, centre-south of the basin – see Fig. 3.22); 3. massive pebbly conglomerate associated with elements SB and CH-2

(Fig. 3.8, centre of the basin – see Fig. 3.22). Sandstone lenses and sheets have erosional relationships with all gravelly facies associations; scour-and-fill structures can occur (Fig. 3.8D).

Architectural element GB, in similarity to some GS, form large complex units and are largely associated with subordinate sandy facies (e.g., St/Sct, Sp, Sm, Scm), as well as architectural elements SB, CH-1, CH-2 and F, and may show lateral accretion and vertical stacking of bar sets (e.g., Fig.s 3.9, 3.12 and 3.13). At sites D17_S1/2 (Fig. 1.1B), GB is associated with architectural element CH-1 (Fig. 3.12), showing an upward coarsening succession and is engulfed in F architectural element (Fig. 3.19). Barsets display lateral accretion and vertical amalgamation, although the bounding surfaces between bars were not easily identified due to exposure (Fig.s 3.12 and 3.19).

Architectural element CH-2 at sites D1_S1 (Fig. 3.14) and D23_S3 (Fig. 3.16) are located about 420 m apart (see Fig. 1.1B), and both sites contain upward coarsening successions composed of F-CH-2-GS, better observed at sites D23_S3 and D13_S2 (see Fig. 3.20, centre of the basin), which seems to terminate in the element GS, similar to site D13_S2 in the centre of the basin (Figs. 3.8 and 3.20). Architectural element CH-2 at site D4_S4 (Figs. 1.1B and 3.15) appears to have a vertically amalgamated architecture. Element SB is possibly co-occurring and displays some lateral accretion (sandy lenses stacked vertically and laterally at low angles – see left-hand side of Fig. 3.15), although the actual geometry of both elements is not evident due to the incomplete exposure of the outcrop (Fig. 3.15).

Architectural element F forms outcrops up to 30 meters thick and a few tens of meters long. It contains facies Fp (Fig. 3.3A) as well as bentonite horizons at sites D6_S2 and D17_SZ (Fig. 1.1B). It often co-occurs with architectural element CS, and less commonly with GB (Figs. 3.15-3.19). However, due to excessive scree, identifying the internal geometry of the facies within architectural element F or its relationships to other architectural elements is difficult. The upper contact with overlying coarse-grained architectural elements is mostly erosional (Figs. 3.11, 3.16 and 3.17) and basal contacts are sharp, non-erosional or gradual. Element CS, which may contain fossils, is always engulfed in architectural element F (e.g., Fig. 3.3C).

Table 3.2. Architectural elements in the Mesozoic Oudtshoorn Basin (modified after Schultz 1984 and Miall 1985).

Architectural element code	Characteristics	Depositional setting
D **(Figs. 3.4-3.6)**	Contains facies: Gm-1, Gh-1 and G-2 (and less predominantly Gi-1). Crudely bedded boulder breccias (D-1) and conglomerates (D-2). Bed termination is sometimes marked by sandy facies. Beds often have sharp, erosional base. Very poorly sorted Gm, upward fining successions are common.	- D-1: debris and hyperconcentrated flows representing quick deposition on fan lobes. - D-2: fluidised flows in braided fan lobes - D-1 probably more proximal than D-2.
GS **(Figs. 3.7 and 3.8, 3.10 and 3.11)**	Contains facies: Gm-2, Gi-2, Gh-2, Sm, Sh, Sp, Smc, Spc.Pebble-to large cobble-sized, polymictic conglomerates and breccias, forming laterally continuous sheets. Normal and inverse grading is common. Basal contacts may be gradational, sharp non-erosional and scoured (up to 38 cm).	- Channel fills in broad, deep braidplain channels with vertically stacked sheet flood deposits. - May also be part of lobes on distal alluvial fans. - Transverse or longitudinal successions in gravelly fluvial deposits. - Outwash plain deposits, channelized lobes on proximal fans, where fan lobe were recycled and redeposited in narrow channel scours.
GB **(Figs. 3.6, 3.9, 3.12, 3.13 and 3.19)**	Contains facies: Gmm-2, Gcm-2, Gh-2, Gi-2, Gp, Gt, Sm, Scm and Sp. Convex down (top) and concave up (base) lenses with lateral pinch-outs. Sm/Sh lenses of up to 5 m are common as bedtop terminations. Gp and Sp often occur as sets. Subangular-subrounded clasts, polymictic and range from pebbles to large cobbles.	- Gravelly longitudinal or transverse bars in gravelly channels. May display lateral accretion (Fig. 3.19). - Channel fills in large gravel-bed fluvial systems such as trunk rivers at the toes of alluvial fans.
SB **(Figs. 3.8, 3.9 and 3.13)**	Contains facies: Sm, Smc, laterally change to Scm or Gcm-2. Amalgamated sandstone lenses with lateral pinch outs. Associated with D-2, GB and CH-2.	- Sandy bars bars in sandy/gravelly channels.
CH-1 **(Fig. 3.12)**	Contains facies: Sm, Sh, Sp and Fl. Basal St are less common and Scm as pebble stringers. Form laterally continuous tabular sandstone sheets. Bed thickness ranges from 30 cm to 1 m. Separated by a sharp bounding surface from the overlying GB architectural element (latter common in proximal sites; see Fig. 1.1).	- Channel fill deposits in broad sandy axial rivers. Association with GB architectural elements may suggest sudden increase in energy levels in the basin (due to tectonic and/or climatic reasons).
CH-2 **(Figs. 3.14-3.16)**	Contains facies: Sm/Scm, St, Sh, Fm, Fl and Sp. Basal Gm, Gt (or Stc) and Gp are common, as well as Sh beds interbedded with v.f-grained Sm and Fm. Sandstone beds may show amalgamated geometry. Post-depositional, <1 cm thick gypsum layers are very common in these deposits in the centre of the basin.	- Longitudinal or transverse bars in low-to-moderate sinuosity fluvial channels.
CS **(Figs. 3.11 and 3.15-3.18)**	Contains facies: Sm, Sh and Gm-2; sometimes Sh and Sm interbedded with Fm. Basal St are rare. Typically, up to tens of meters long and up to 1 m thick. Occurs engulfed in architectural element F or underlies architectural element CH-2. May contain fossils (Fig. 3.3).	- Crevasse splay deposits on a low energy floodplain.
F **(Figs. 3.11 and 3.15-3.19)**	Contains facies: Fm and Fh (common); Fp and Fg (rare). Bentonite noted at sites D6_S2 and D17_SZ (see Fig. 1.1B). Post-depositional, <1 cm thick gypsum layers are very common in these deposits in the centre of the basin.	- Low energy floodplain deposits.

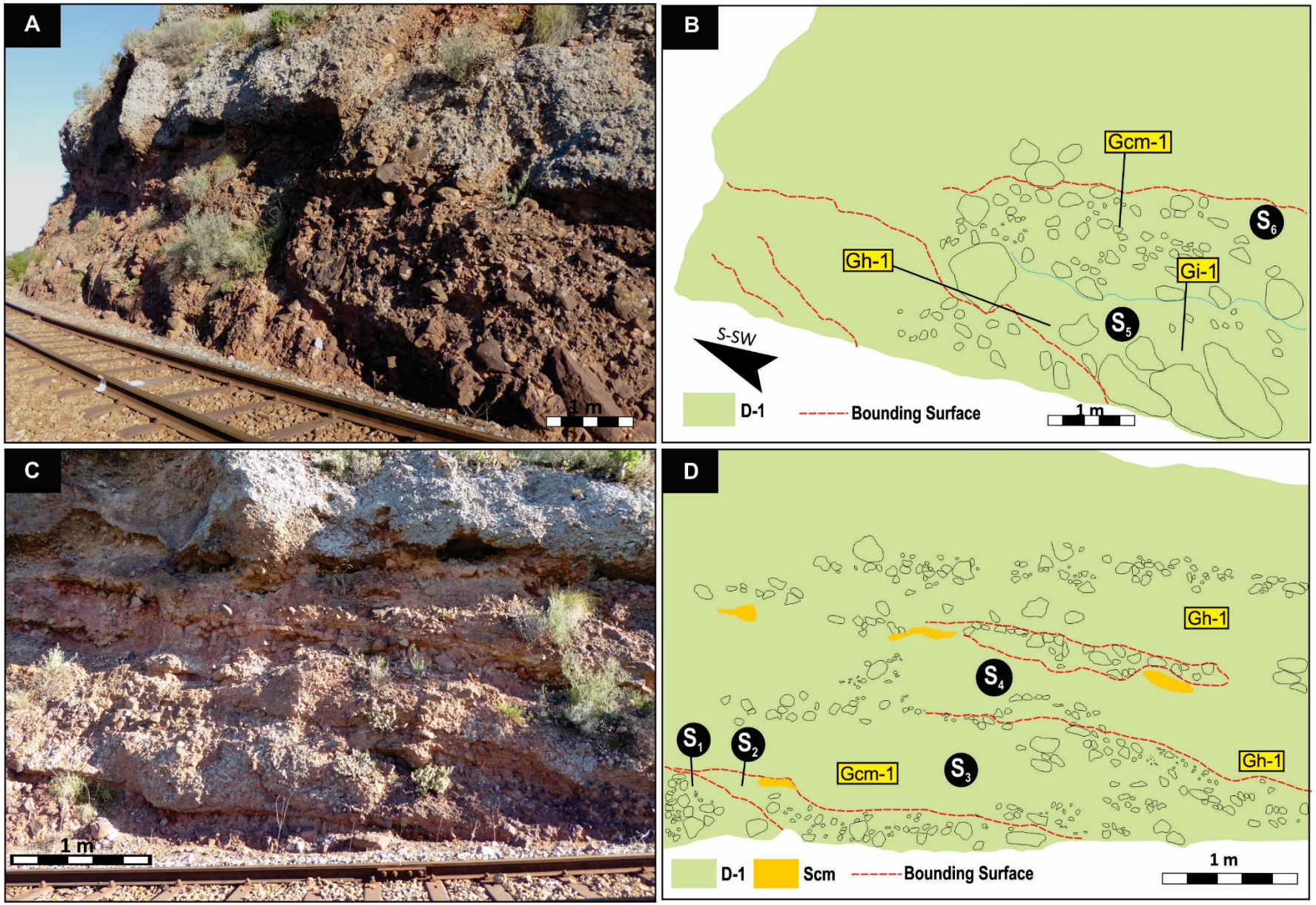

Figure 3.3. Architectural element D-1at site D12_S8. Sandy facies are rare and scoured by facies Gmc-1 and Gmm-1. Six debris flow successions have been tentatively identified (S1 to 4). For site localities see Figure 1.1B.

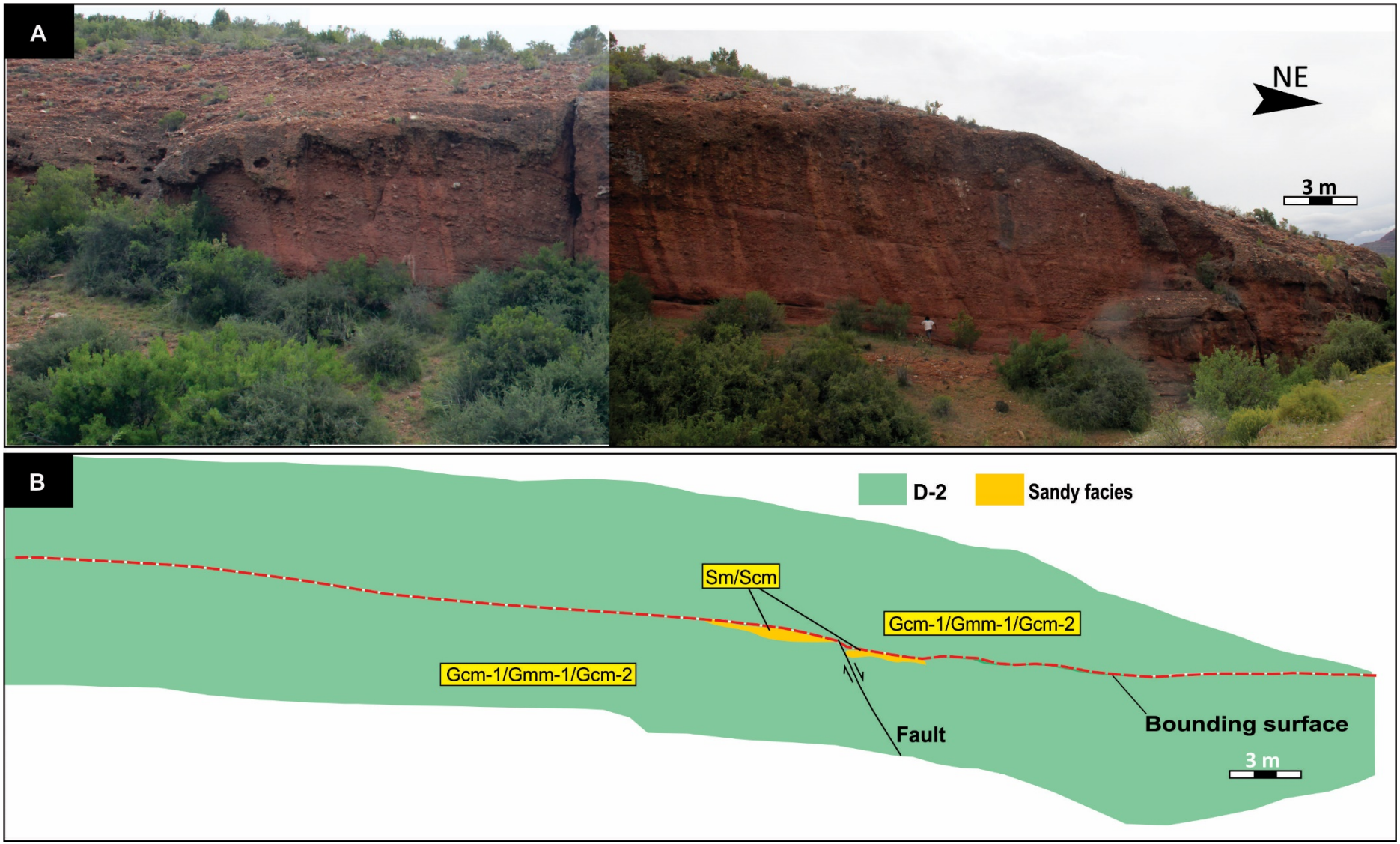

Figure 3.4: Architectural element D-2 deposits at site D12_S7. Sandy facies occur at bedtop terminations (see B) and are downcut by the overlying facies Gmc-1and Gmm-1. The clast sizes at this site show both upward-fining and -coarsening trends on a smaller scale (see D) and an overall upward-coarsening trend, concurrent with a greater occurrence of large clasts (see C and D). Average clast diameter changes from 13 cm at the bottom, to 8 cm and 26 cm in the middle and top, respectively. For site localities see Figure 1.1B.

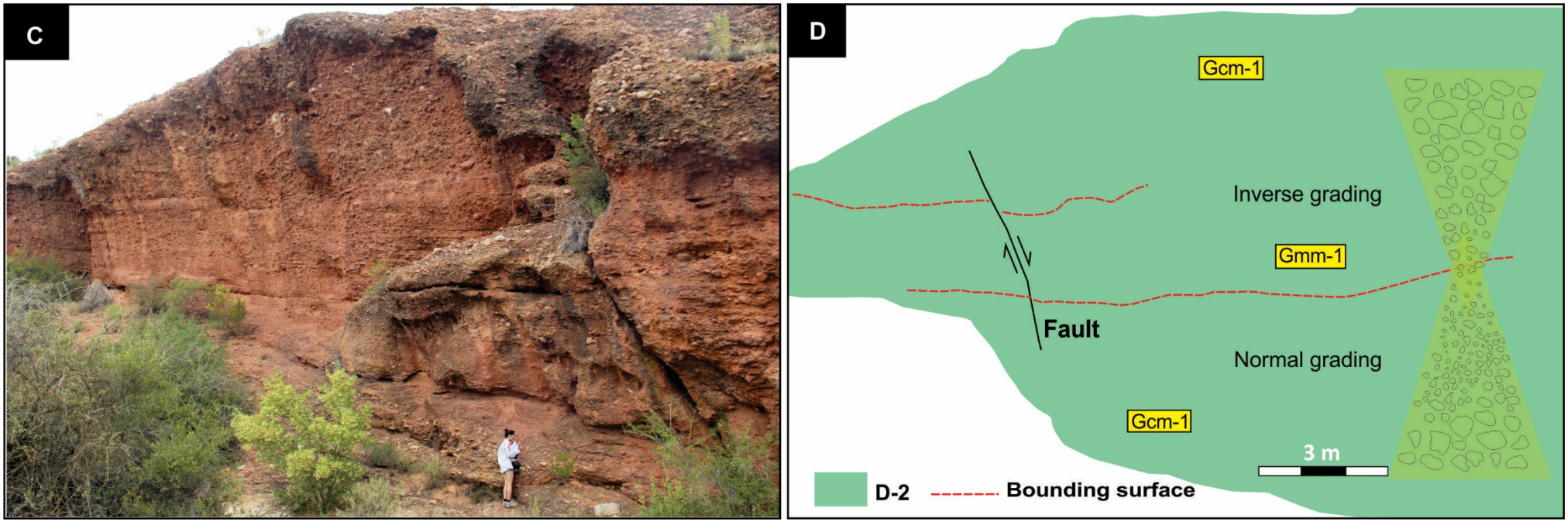

Figure 3.5 ctd: Architectural element D-2 deposits at site D12_S7. Sandy facies occur at bedtop terminations (see B) and are downcut by the overlying facies Gmc-1and Gmm-1. The clast sizes at this site show both upward-fining and -coarsening trends on a smaller scale (see D) and an overall upward-coarsening trend, concurrent with a greater occurrence of large clasts (see C and D). Average clast diameter changes from 13 cm at the bottom, to 8 cm and 26 cm in the middle and top, respectively. For site localities see Figure 1.1B.

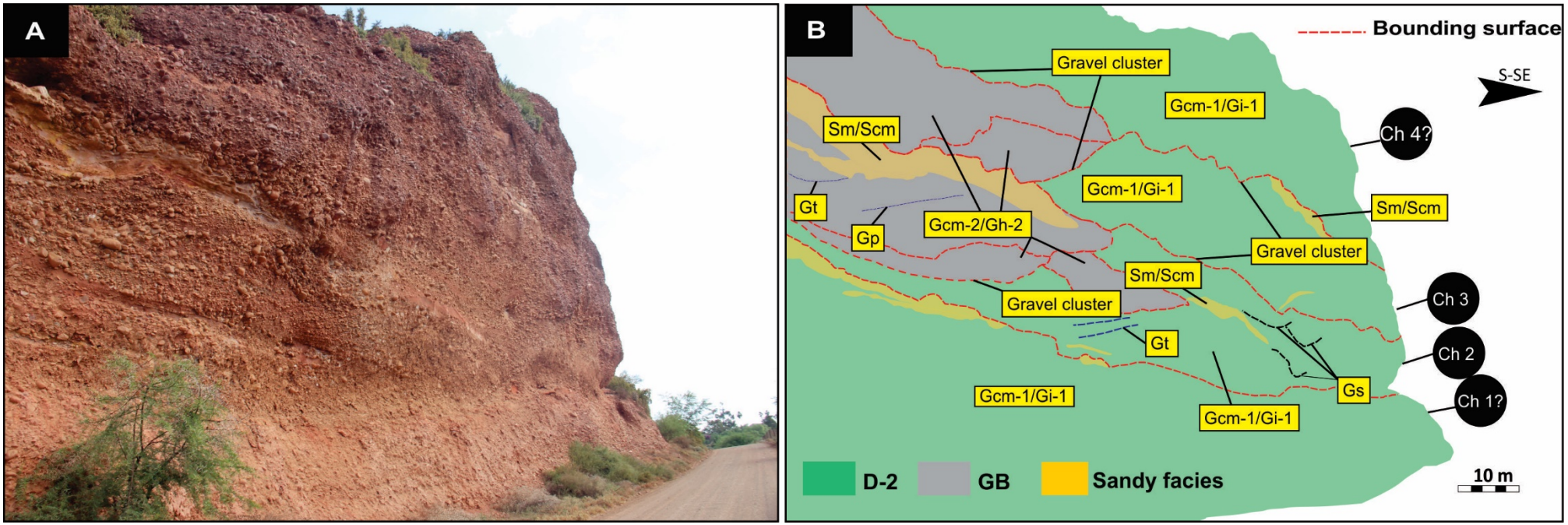

Figure 3.6. Architectural elements D-2 and GB at site D11_S2 in the southern part of the basin. Imbrication suggests N-NW palaeoflow (see Fig. 24E). Very crude bedding is marked by the bounding surfaces in B and clusters of imbricated clasts. Four channel fill successions have been tentatively identified (Ch 1 to 4). For site localities see Figure 1.1B.

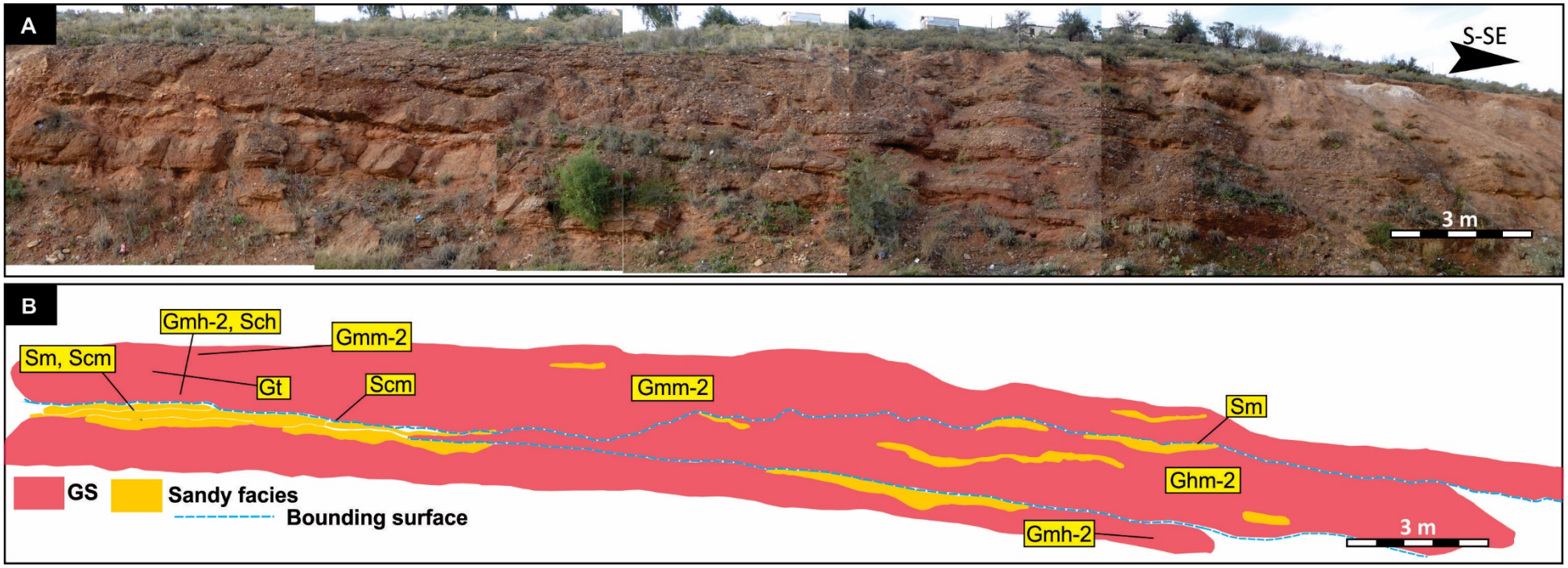

Figure 3.7. Architectural element GS at site D5-S3, dipping at 152/10 E. The structural measurements suggest that site D5_S3 is stratigraphically above sites D6_S1, which displays floodplain deposits (see Appendix Fig. 7.2). For site localities see Figure 1.1B.

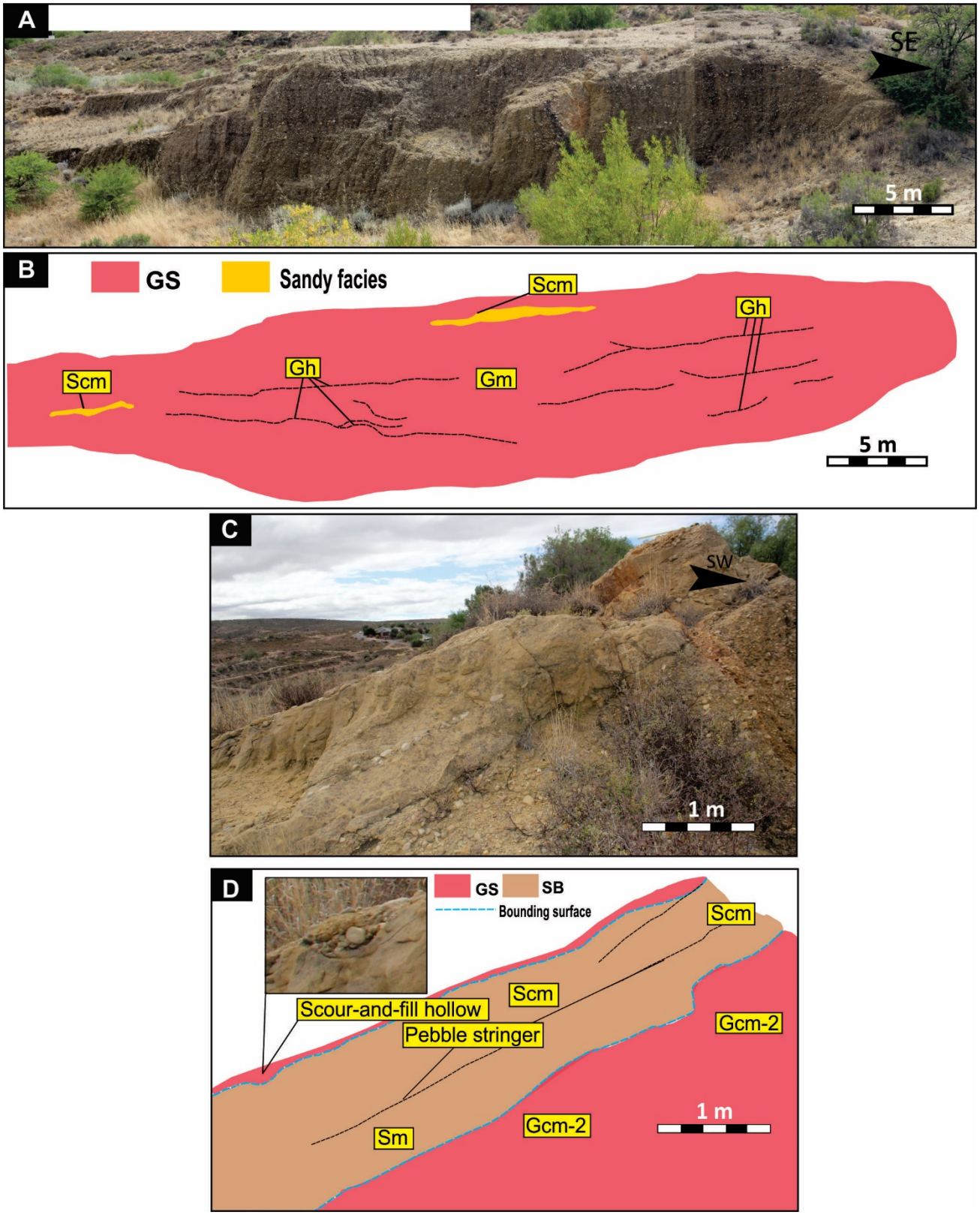

Figure 3.8. Architectural element GS at site D13_S2. This site is located stratigraphically above site D23_S3 (Fig. 3.16). Strata in A and B dips ~35˚ NE. C and D show architectural elements GS and SB, which are overlying those in A and B. For site localities see Figure 1.1B.

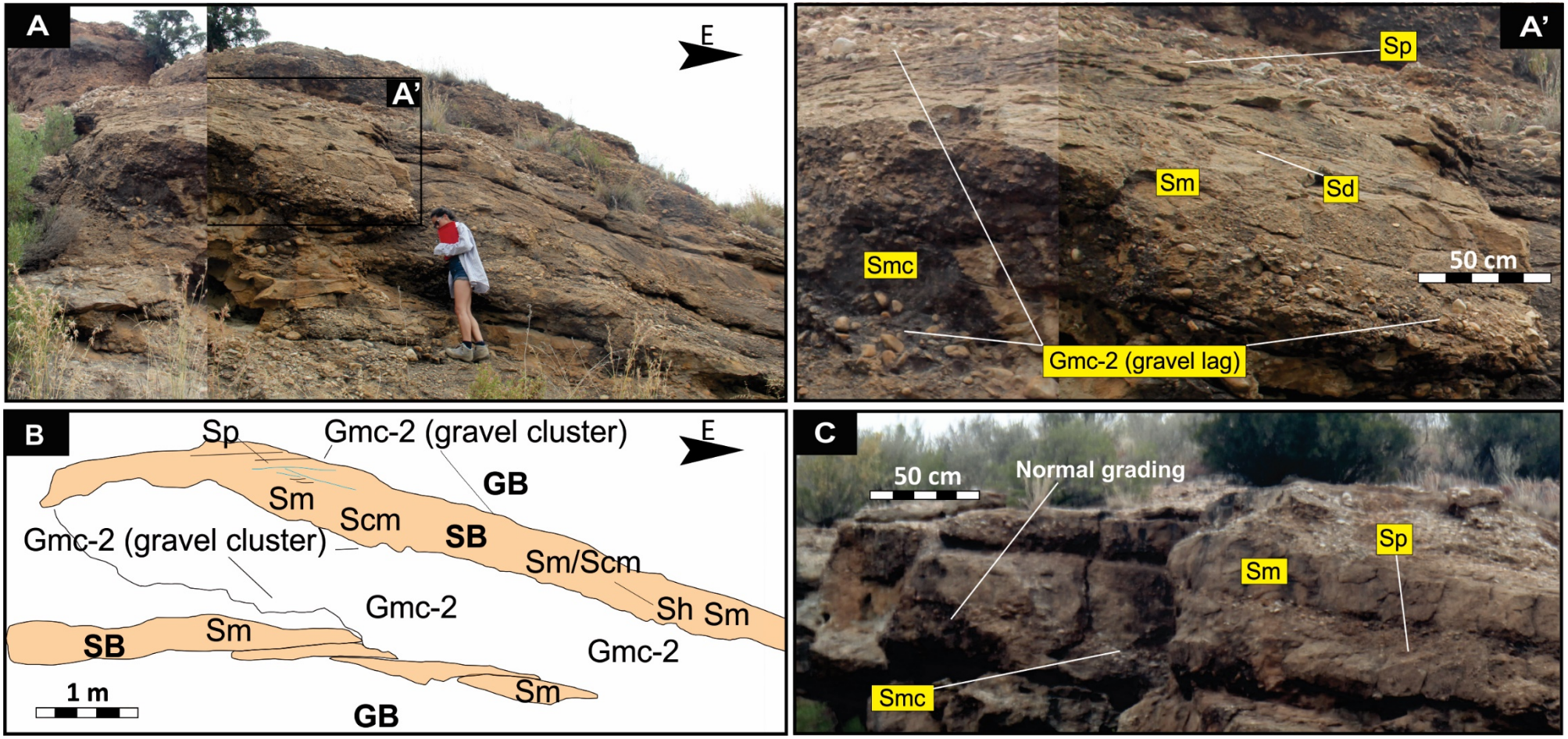

Figure 3.9. Architectural elements SB and GB at site D12_S6 in the eastern part of the basin. C and D show the internal structure of architectural element SB. Strata dip 25˚ N-NW. For site localities see Figure 1.1B.

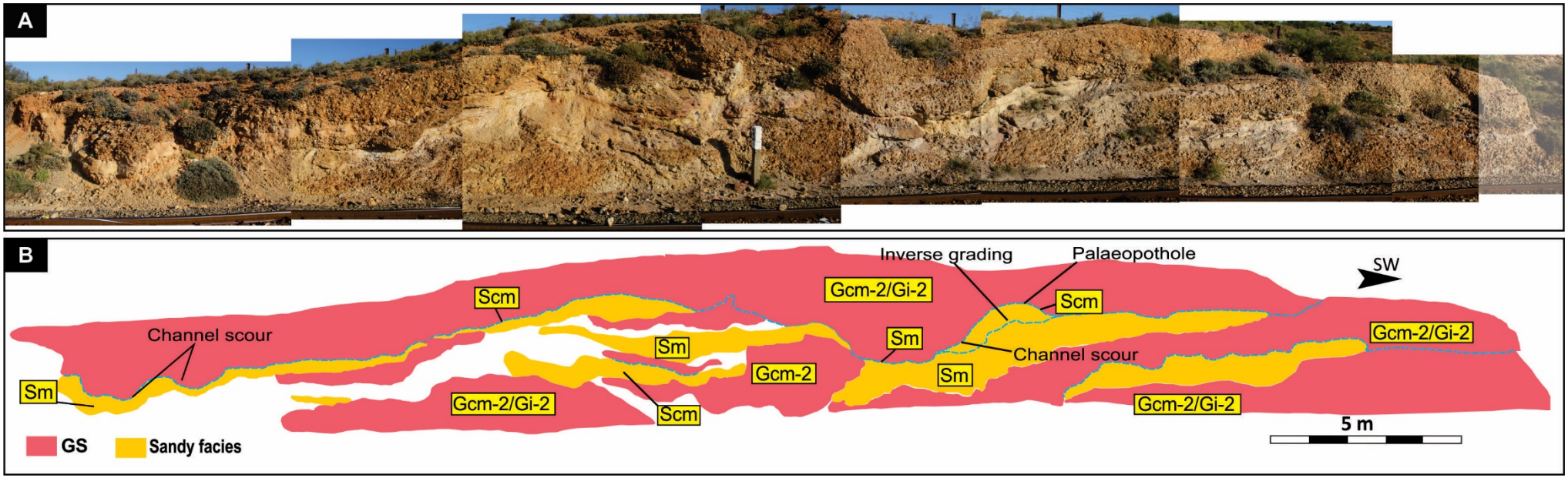

Figure 3.10. Architectural element GS at site D9_S1. Main palaeoflow was to NW. For site localities see Figure 1.1B.

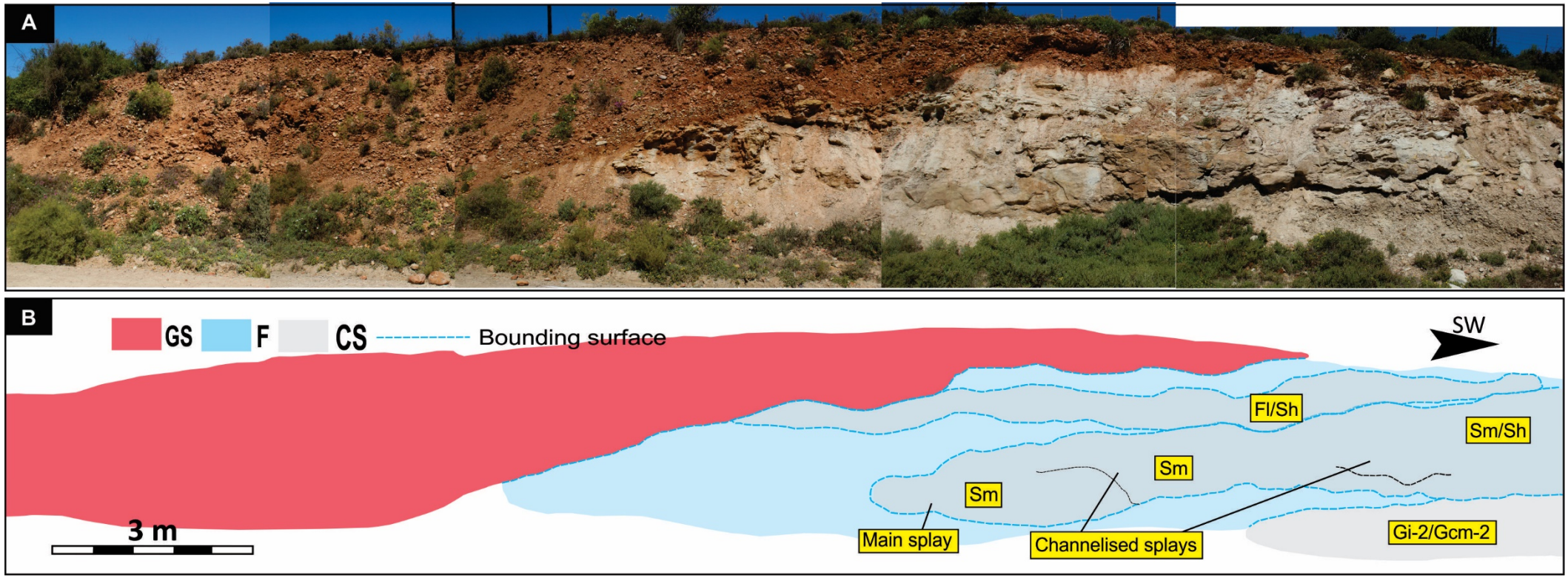

Figure 3.11. Architectural elements GS, F and CS at site D10_S3. For site localities see Figure 1.1B.

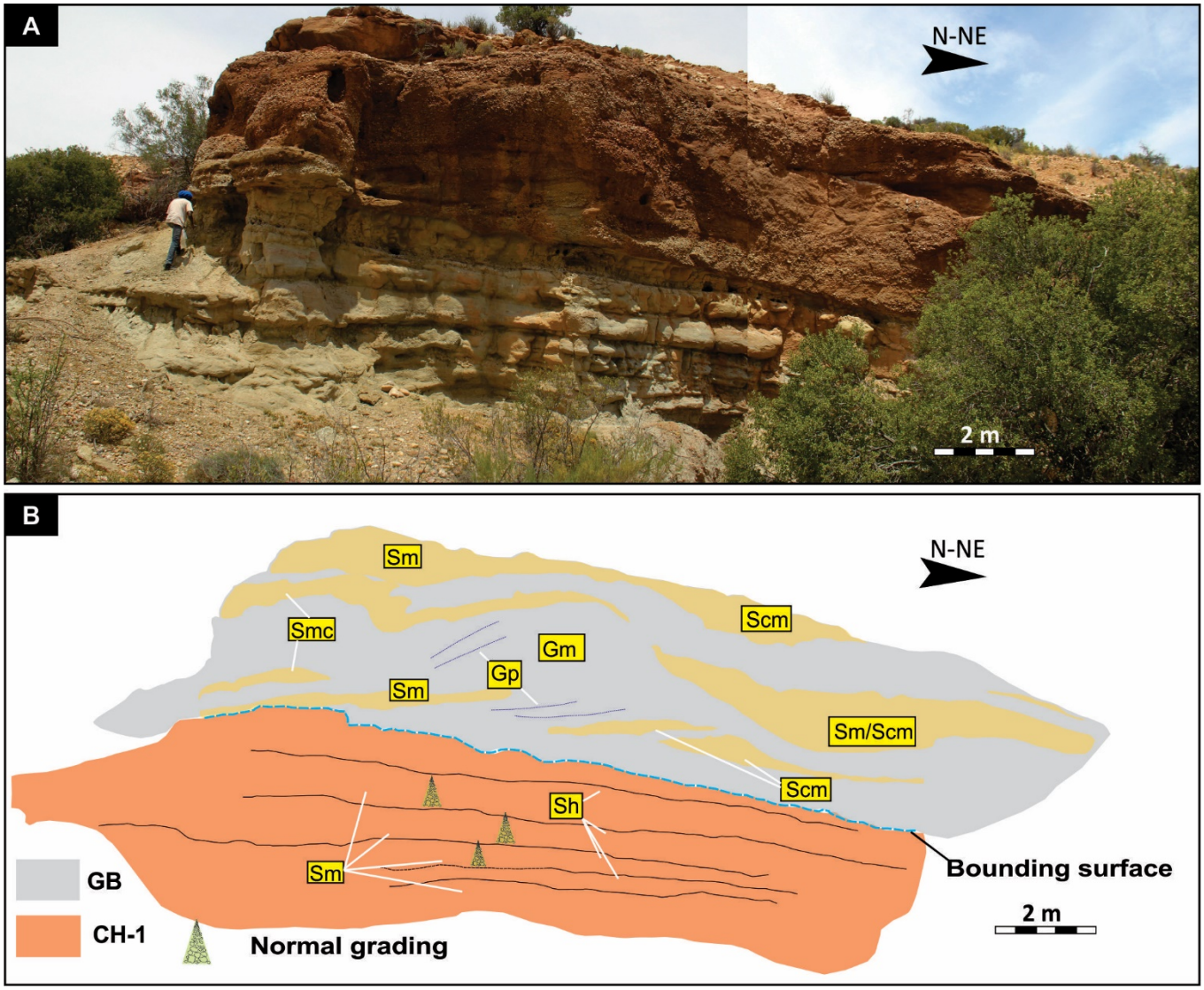

Figure 3.12. Architectural elements GB and CH-1 at site D17_S2. Strata dip 20˚ N-NE.

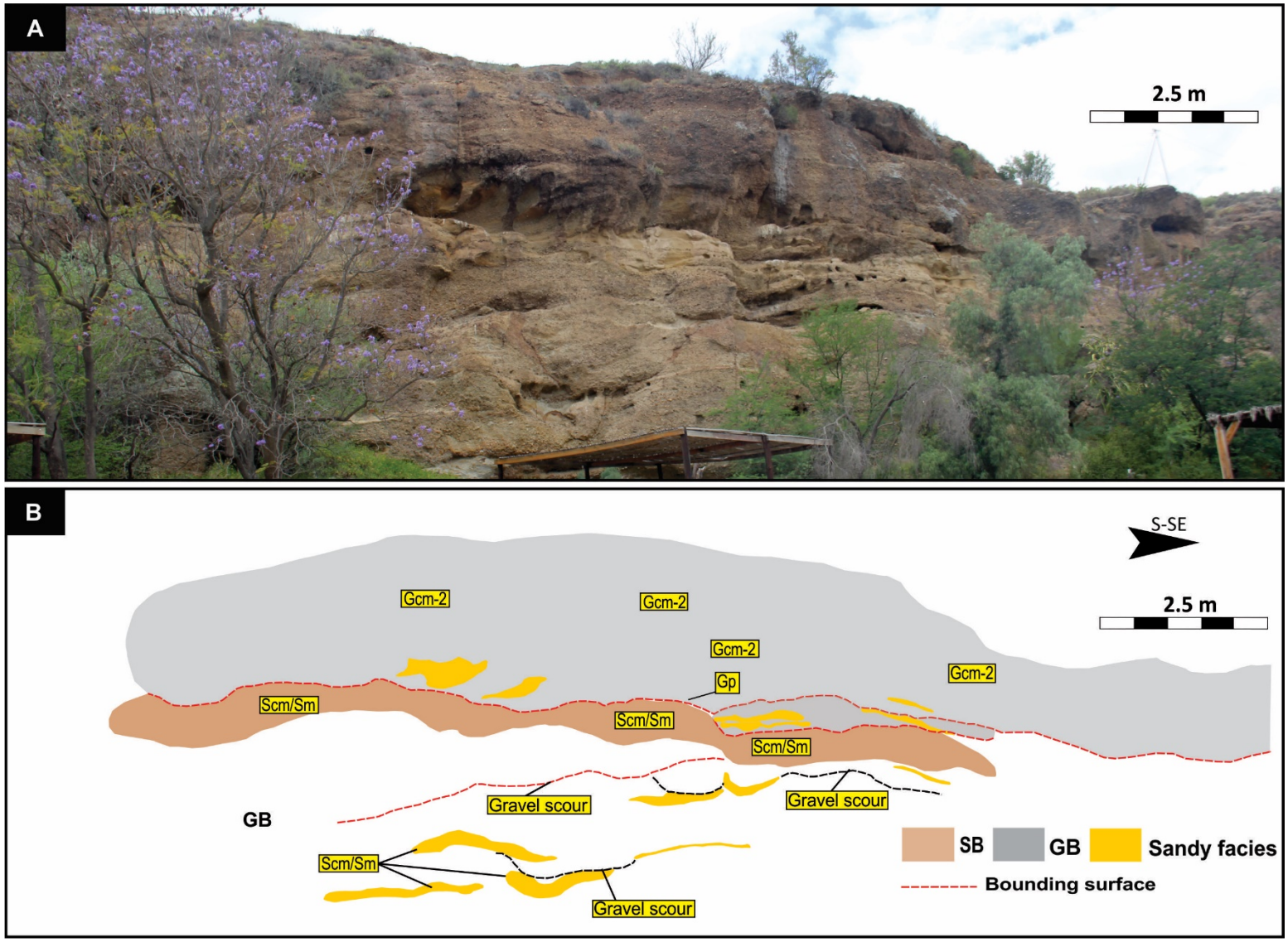

Figure 3.13. Architectural elements GB and SB at site D6_S4. Due to tree cover, the lower half could not be mapped out. Strata dip 30˚ NE-E. GB is most likely made up of amalgamated compound bars (e.g. Fig. 3.2E) which could not easily be mapped out. Gravel scours in the lower half mark the bounding surfaces between individual bars. For site localities see Figure 1.1B.

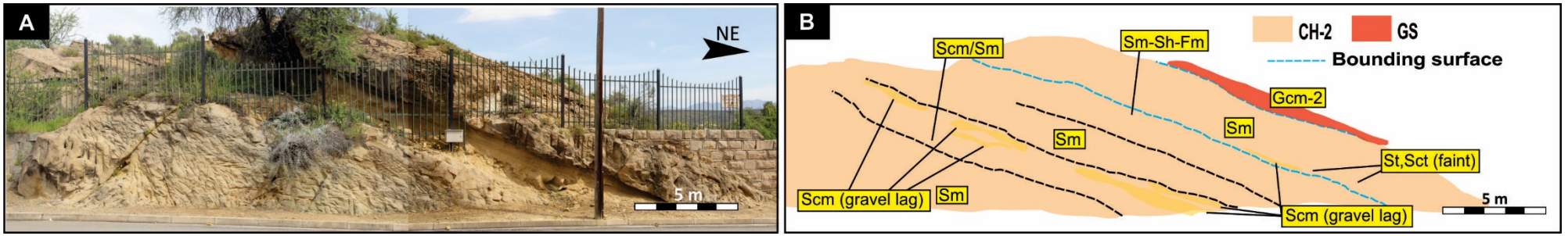

Figure 3.14. Architectural element CH-2 at site D1_S1, with a thin veneer of overlying architectural element GS. Strata dip 35˚ NE. Site D23_S3 (Fig. 3.16) is located 420 m to NE from this site. For site localities see Figure 1.1B.

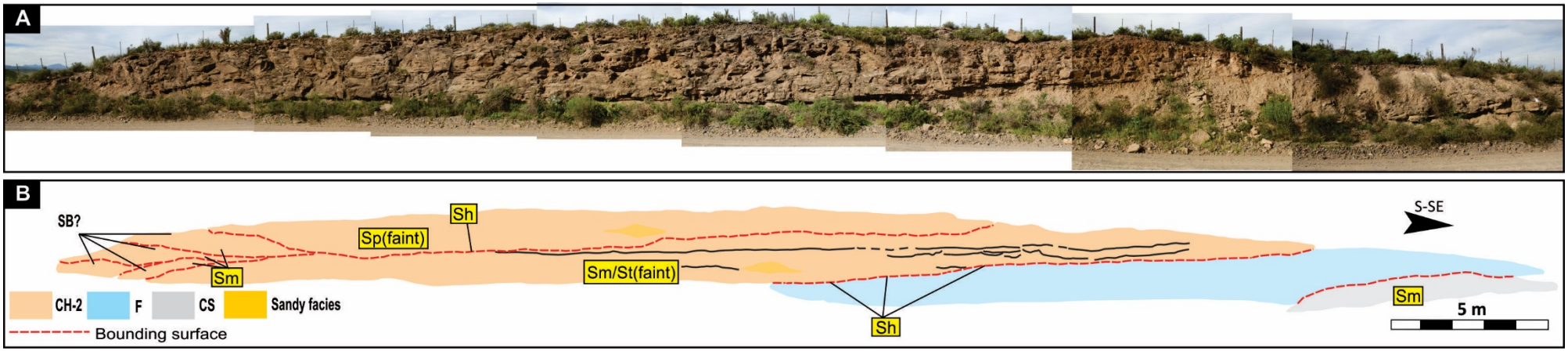

Figure 3.15. Architectural elements CH-2 and F at site D4_S4. Amalgamation of lenses of facies Sm on the left may be due to lateral accretion, but due to outcrop quality further identification is not possible. Faint, rare trough cross-bedding indicates palaeoflow from SW to NE. For site localities see Figure 1.1B.

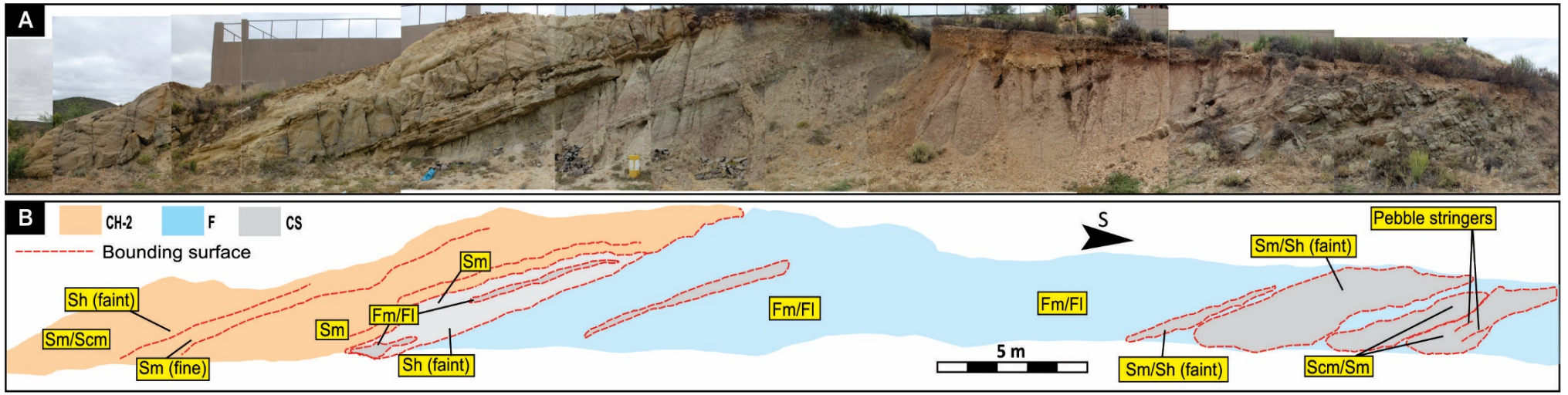

Figure 3.16. Architectural elements CH-2, F, CS and L at site D23_S3. There is a very thin veneer of Gmc-2 overlying CH-2, similar to that at site D1_S1 (Fig. 3.14). Strata dip 28˚ NE. For site localities see Figure 1.1B.

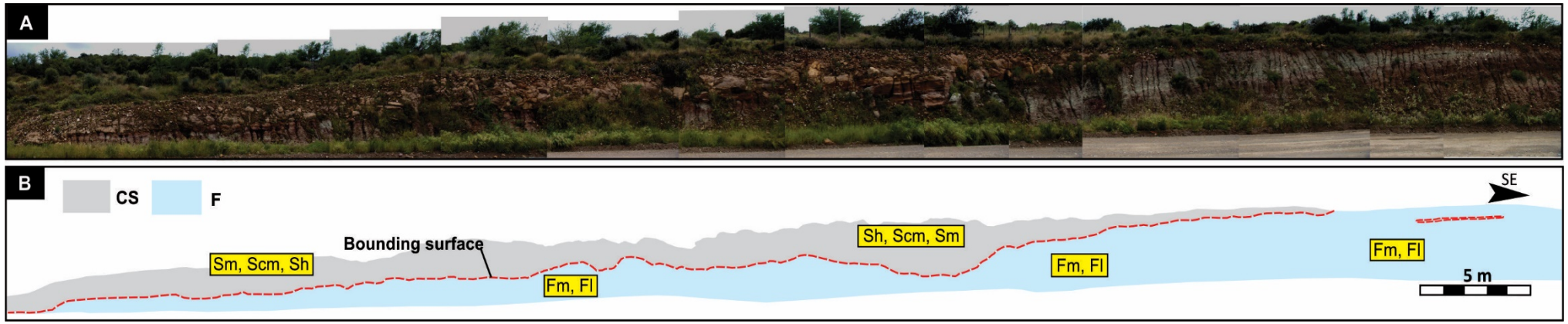

Figure 3.17. Architectural elements CS and F at site D12_S4. For site localities see Figure 1.1B.

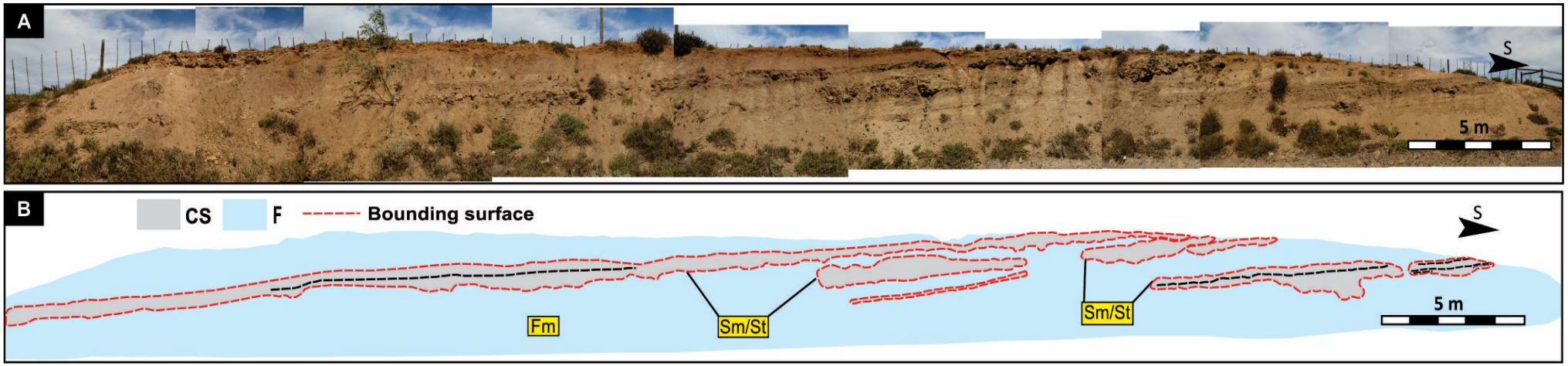

Figure 3.18. Architectural elements CS and F at site D4_S3 in the central-eastern part of the basin, just north of site D4_S4 (Fig. 3.15). Compared to site D12_S4 (Fig. 3.17), architectural element CS here is thinner and comprises different facies. For site localities see Figure 1.1B.

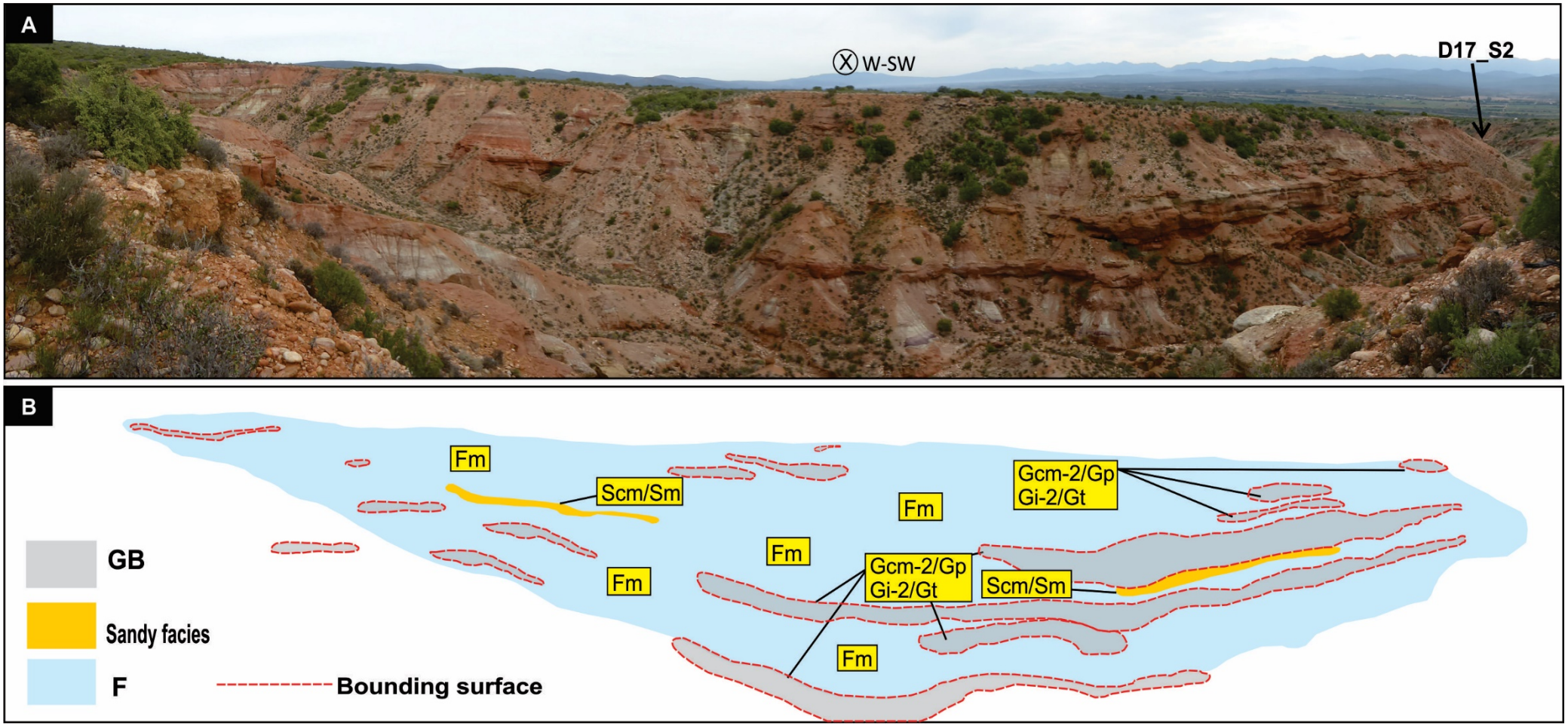

Figure 3.19. Architectural elements GB and F at site D17_S2_Z in the south of the basin. The total length of the photomosaic is about 150 m. The height of the valley in the centre of the photomosaic is ~40 m. For site localities see Figure 1.1B.

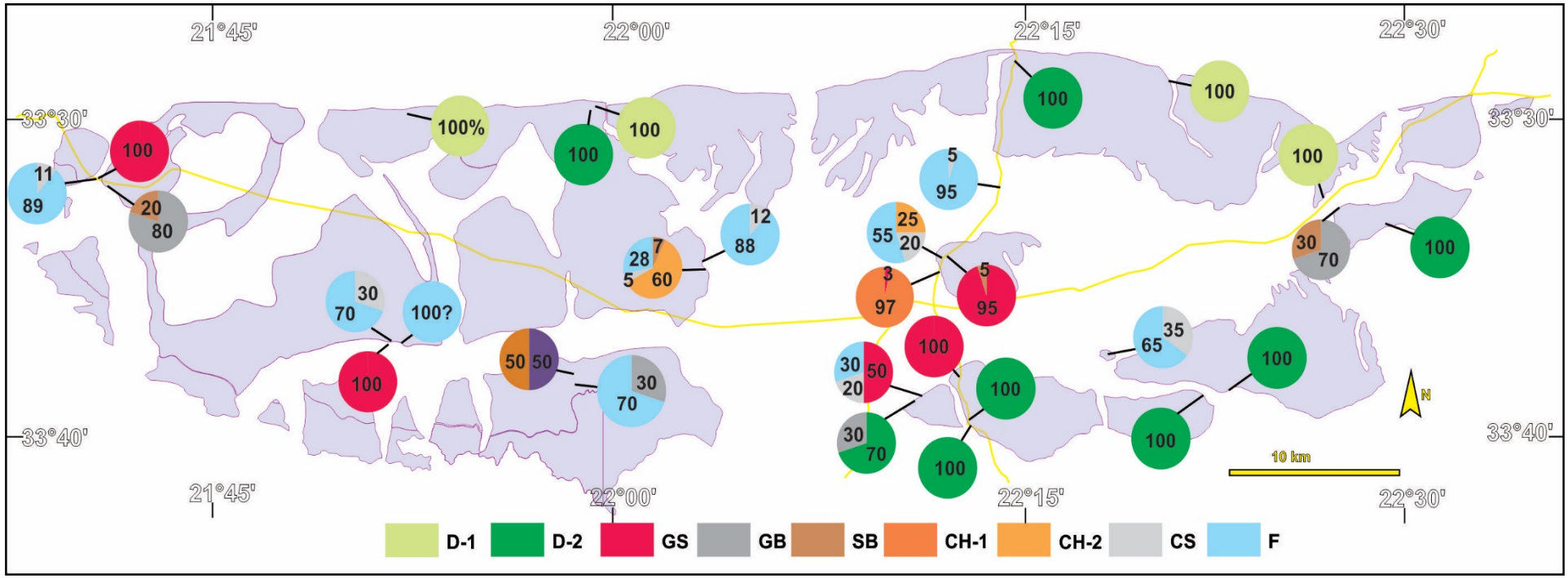

Figure 3.20. Distribution of the facies association in the Oudtshoorn Basin. Pie charts are visual estimates in % of the relative abundances of architectural elements in the studied outcrops. Because the outcrops are spatially isolated and contain no stratigraphic markers, regional mapping of the facies associations is not practical. For site localities see Figure 1.1B.

3.2. Clast counts

3.2.1. Clast size of the gravelly facies

To evaluate the grain size variation in gravelly facies (lithofacies G- and Smc/Stc), as discussed in the Methodology chapter, the standard Udden-Wentworth clast size classification scheme was used in the field, where at least 150 clasts were measured (long axis) at each of the 18 clast count sites (Fig. 1.1B). The results are shown as a comparative distribution plot and map in Figures 3.21 and 3.22.

Very coarse-grained, and very poorly sorted breccias (facies D-1) in the north of the basin (Figs. 3.1A and D) show a very broad range of clast class distributions from small pebbles to large boulders. Very coarse-grained conglomerates (facies D-2) are also very poorly-to-poorly sorted (Fig. 3.1F); however, overall, clast class range is relatively narrower and clast class percentage difference is greater in conglomerates than in the very coarse-grained D-1 breccias, except for sites D12_S7 (far east of the basin) and D9_S4(south-centre of the basin). The conglomerates also show a greater percentage of boulder-sized clasts (≥medium boulder), although in both type of deposits these can constitute outliers. Clasts in element GB (e.g., Figs. 3.2D, E, 3.9 and 3.12) conglomerates range from medium pebble to small boulder, and very coarse pebble to large cobbles account for more than 80% of the clast count. Very coarse-grained lithofacies in GS deposits are moderately-poorly sorted (Figs. 3.2A, C, G, 3.7, 3.8 and 3.10) and clasts range from small pebble to large cobbles, with a small percentage of small boulders (D9_S1, Fig. 3.21). Clasts in CH-2 architectural element are associated with Smc (gravel lags, pebble stringers) and basal Stc lithofacies (e.g., Fig. 3.2J) and are prominently made up of poorly sorted small-very coarse pebble, with coarse pebble making up more than 50% of the clast count.

There seems to be a relationship between clast size range and lithofacies association. Very coarse-grained breccias in element D-1 show relatively smooth distributions with clasts spanning 6-7 classes and the maximum percentage for a single class is rarely more than 20%, except for site D12_S8 (Fig. 3.1B). Clast class in very coarse-grained D-2 element conglomerates span over 5-6

classes and the distributions are closer to symmetrical bell-shape, and some maximum class percentages are equal to or greater than 20% (D12_S7 and D9_S4, which also show a broader distribution of classes). Medium-grained conglomerates in GB facies (D17_S2, D12_S6, D6_S4) have near-symmetrical bell-shaped distributions and clasts range 4-5 classes. With the exception of D9_S1, medium-grained conglomerates (D13_S2) and breccias (D5_S3) of facies GS have asymmetrical distributions and 5 clast classes. The clast class percentages in D5_S3 seem to be segregated in three main clusters, and this could be related to very well-developed normal-reverse grading successions in those deposits (Figs. 3.2A and 3.7). The distributions in clast-rich (lithofacies Smc and Stc) CH-2 element sandstone are also bell-shaped and near-symmetrical (D7_S2 and D23_S3) and span 4 classes. Although the distribution of facies and corresponding associations seems to be related to their relative proximity to the basin margins (see Fig. 3.22 below), it is not easily evident whether there is proportionality between clast size and distance from the basin margins in the gravelly facies associations (e.g., site D17_S2 in Figs. 3.19 and 3.22, circle in the SW of the by 22^{o}E, sites D5_S3 and D6_S4 in the western end of the basin in Fig. 3.22).

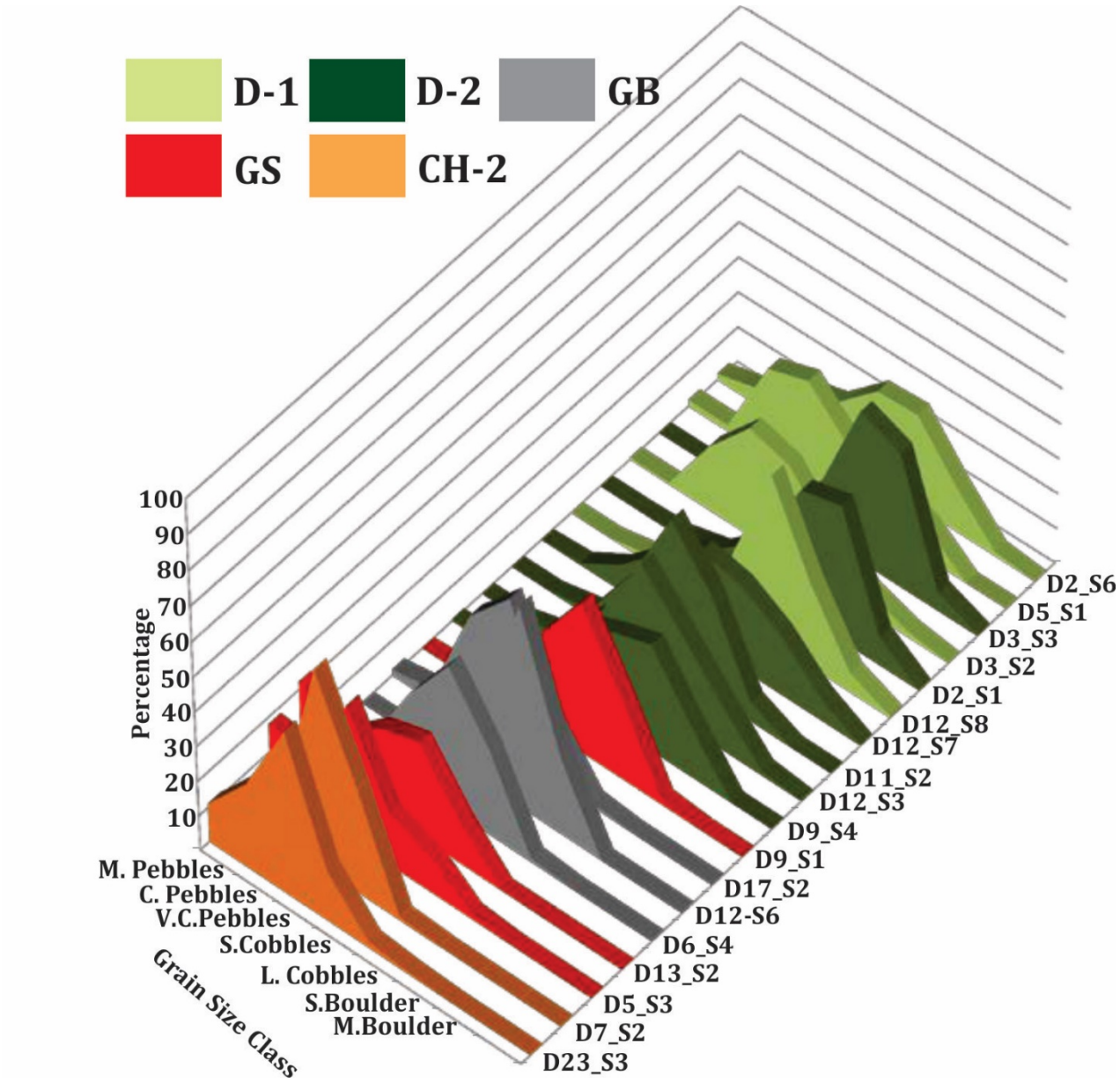

Figure 3.21. Distribution of clast sizes in the gravelly facies in the Oudtshoorn Basin. Number of measurements taken at each site is indicated in individual plots in Appendix Figure 7.3; for the location of the clast count sites, see Figures 1.1B and the map in Figure 3.22 below. The cm value of the grain size classes is shown in Table 2.2 in the Methods chapter.

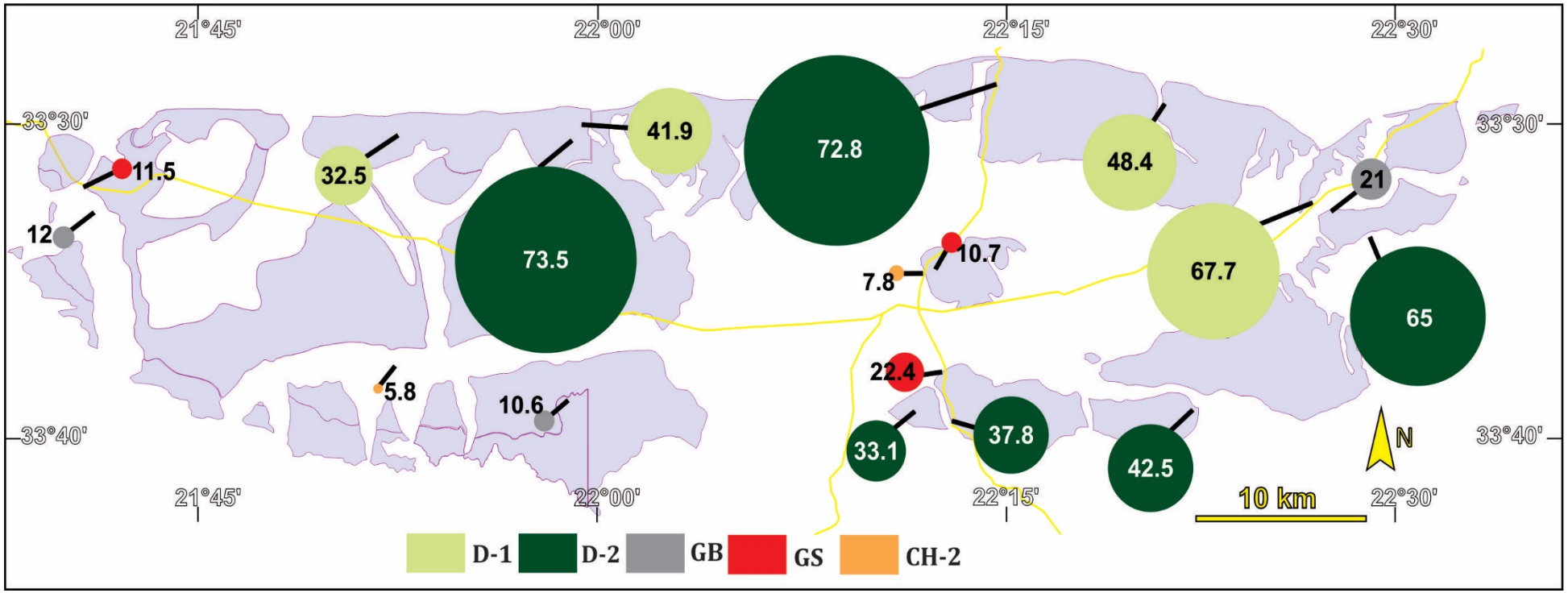

Figure 3.22. Average diameter of the 10 largest clasts in the gravelly and pebbly sand facies in the Oudtshoorn Basin. The numbers inside or next to the circles indicate the rounded up average diameter in cm at each clast count locality.

3.2.2. Clast composition of the coarse-grained facies

The pebble-to-boulder sized clasts in lithofacies G- and Smc are primarily composed of quartzite, which makes up about 73% of the clast composition in coarse-grained conglomerates and breccias. Approximately 56% of all quartzite is light and dark grey (Fig. 3.23A), with the remaining being white, pink and red. Coarse and medium-grained sandstones make up 5% of the clasts, followed by conglomerate (1.7%) and mudstone/shale. One occurrence of a sandstone rip up clast was also noted at site D9_S4 (Fig. 3.23A; see Fig. 1.1B for site locations). Because of strong masking by a red, orange and sometimes yellow weathering crust (also mentioned in Du Preez, 1944), the lithology of many clasts could not be identified, and these are labelled "unidentified" in the clast counts (Fig. 3.23A). Due to strong cementation and the hardness of these clasts, they could not be split up to investigate the lithology under the crust. However, based on the composition of the few that did split, it is very likely that most of the crusted clasts are also quartzite. Sandstone clasts are medium-to-coarse grained, massive, horizontally and ripple cross-laminated, and locally can have slate-like in texture. Cobble-to-boulder sized conglomerate clasts are grey and white, and contain gravel-sized granule-to-coarse pebble sized clasts. Mudstone/shale clasts are dark grey-black, and are either massive or horizontally laminated.

Compositional variability of the gravelly facies in the Oudtshoorn Basin (Figs. 3.23A and 3.24A) is greater in the north (sites D2_S1, D3_S3), south basin (D9_S1, D9_S4, D11_S2) and west of the basin (D5_S3 and D6_S4; see Fig. 1.1B for site locations). Poorly sorted breccias in element D in the north and east of the basin do not show great compositional variation, assuming that most unidentified clasts are quartzite (D2_S2, D5_S1, D3_S2 and D12_S8). In contrast, conglomerates in element D in the north show greater compositional variability (examples are sites D3_S2 and D2_S1) than those in the south (D11_S2, D25_S2, D9_S4), and south-east (D12_S7). Facies GS (D9_S1) and GB (D17_S2) in south, as well as GB (D12_S6) east of the basin comprise primarily monomictic conglomerates, made up of quartzite and minor occurrences of sandstone. Site D6_S4 close to the western margin shows similar composition, with minor occurrence conglomerate clasts.

Polymictic conglomerates and breccias in facies GS at sites D5_S3 and D13_S2 and CH-2 (D7_S2 and D23_S3) show the largest percentages of sandstone clasts in the basin, with minor occurrences of shale clasts (D5_S3).

Breccias in facies D-1 at sites D5_S1 and D2_S6 show great difference in clast roundness despite their compositional, textural and grain size similarities (Figs. 3.23B and 3.24B), as well as their relative proximity to the fault scarp along the northern basin margin. The clast roundness distribution of site D12_S8 (breccia facies D-1, east of the basin) is closer to that of site D2_S6 than D5_S1 (Figs. 3.23B and 3.24B). Polymictic conglomerates close to the northern basin margin (sites D2_S1 and D3_S3) show common textural, compositional (Figs. 3.23A and 3.24A), grain size (Figs. 3.21 and 3.22) and roundness (Figs. 3.23B and 3.24B) characteristics.

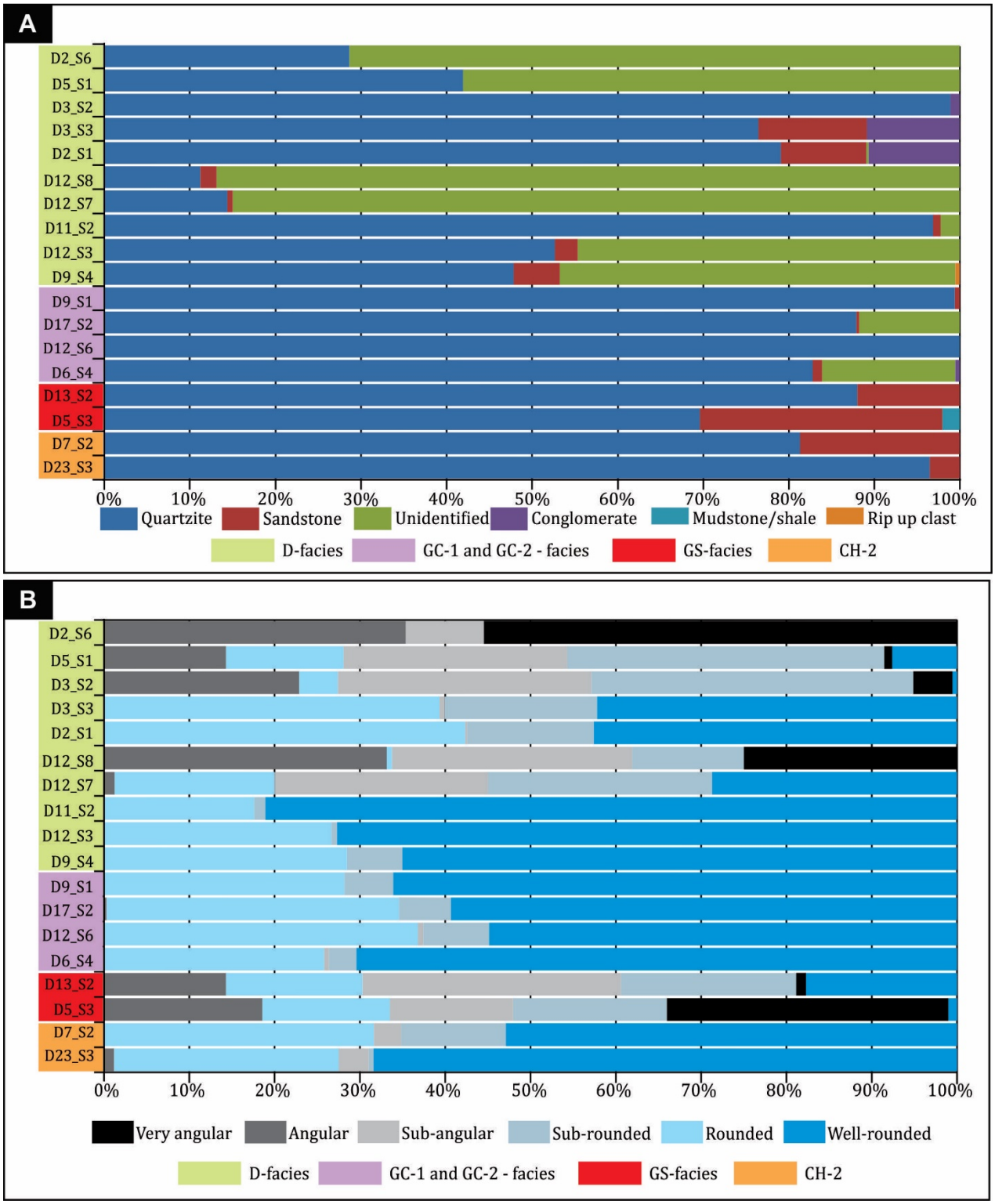

Figure 3.23. Distributions of clast composition (A) and roundness (B) in coarse-grained facies (architectural elements D, GS, GB and CH-2) in the Oudtshoorn Basin. Note the most likely lithology of clasts marked "unidentified" is also quartzite.

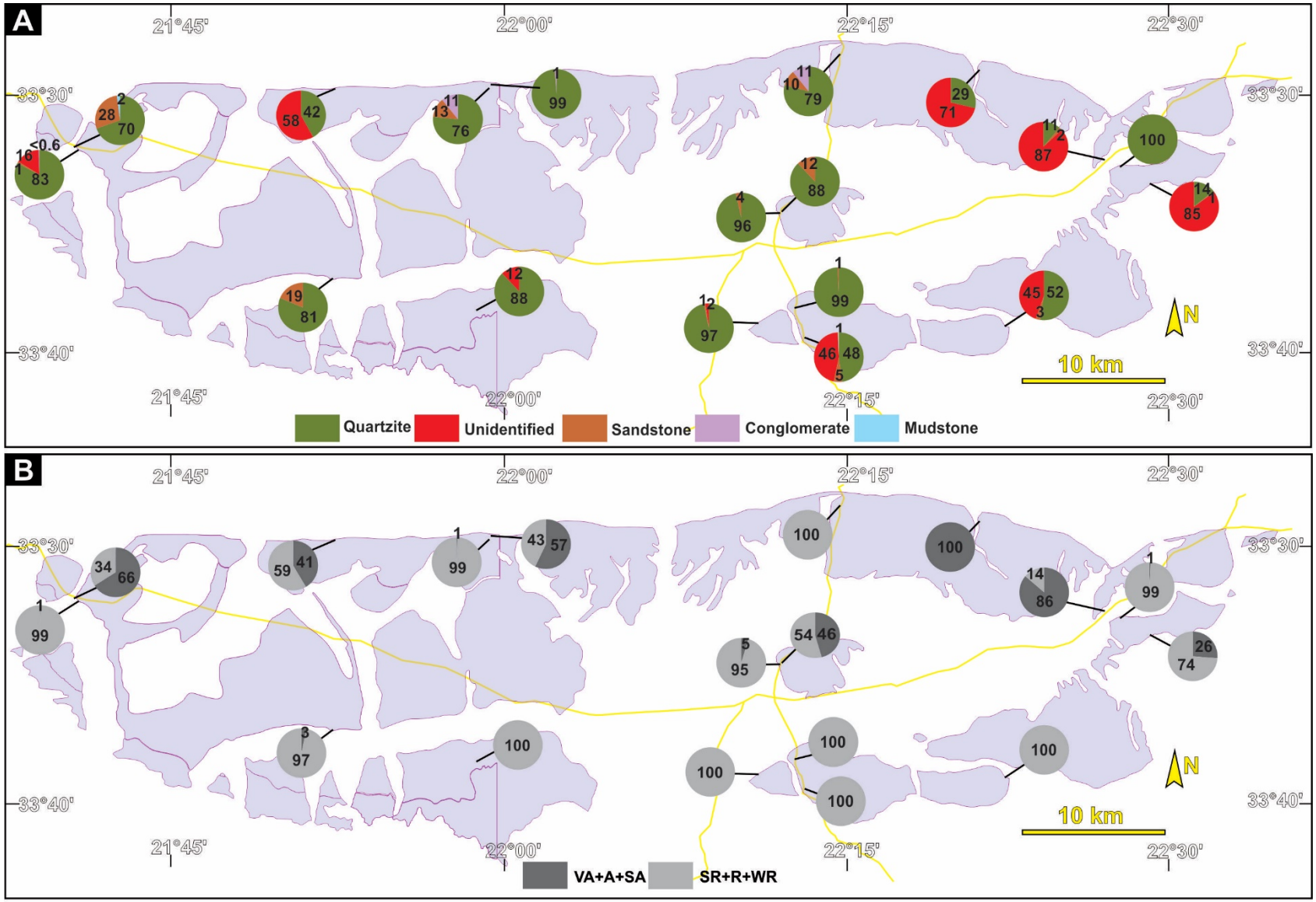

Figure 3.24. Clast composition (A) and roundness/angularity (B) map of the coarse-grained facies in the Oudtshoorn Basin. VA: very angular, A: angular, SA: sub-angular, SR: sub-rounded, R: rounded, WR: well rounded. Numbers are in %.

3.3 Petrography

Seventeen sandstone samples were analysed petrographically to determine their respective quantitative modal compositions, using the Gazzi-Dickinson method of point counting (Ingersoll et at., 1984; Dickinson, 1985).

Quartz, both mono- and polycrystalline quartz (Qm and Qp, respectively; e.g., Appendix Figs. 7.4A and B) is the dominant mineral in all sand sized grain fractions (0.0625 - 2 mm). Undulose extinction in quartz is very common, particularly in the coarser-grained samples. The common feldspar (F) types are plagioclase (Pk; multiple-twinned, cross-hatched twinning) and alkali feldspar (Ak; perthite alteration and simple twinning; e.g., Appendix Figs. 7.4C, D and E) t. Lath-like inclusions in feldspar are common and are often in association with reaction rims and etching by surrounding cement and matrix (e.g., Appendix Figs. 7.4F, H). Lithic fragments (L) are herein defined as particles comprising of micro- or phenocrysts and groundmass of varying sizes and textures, respectively. Sedimentary lithic fragments (Ls) are mostly composed of interlocked Qm, F and accessory minerals (e.g., mica), seldom set in a very fine-grained groundmass, which most often shows reaction textures with the microcrysts (e.g., Appendix Figs. 7.4G and H). Metasedimentary lithic (Lm, Appendix Fig. 7.4J) fragments show foliated texture defined by the alignment of clays wrapped around coarser grains. Metaquartzite was distinguished from Qp by the etched and strained grain boundaries, as opposed to anhedral-subhedral granular texture in Qp (Lm, Appendix Fig. 7.4I). Recognisable accessory minerals include chlorite, minor mica, calcite, zircon and oxides.

The samples mostly fall in the litharenite/arenite compositional fields (Fig. 3.25A; Appendix Table 7.2). Based on their matrix content (classification scheme of Williams et al., 1982 as in Boggs 2009), litharenites and wackes make up two-thirds and one-third of the samples, respectively (Appendix Table 7.2). Samples in the south of the basin (red circles in Figs. 3.25A and B; map in C) are more quartz rich (i.e., most mature) compared to samples in the centre of the basin (blue circles in Figs. 3.25A and B; map in C), which are rich in lithics and are more feldspathic. Other spatial trend in the compositional distribution of the samples could not be identified within the basin. Most samples plot in recycled orogen provenance field of Dickinson (1985) except for the samples from the south of the basin (Fig. 3.25C), which fall within the continental block provenance field (Fig. 3.25B).

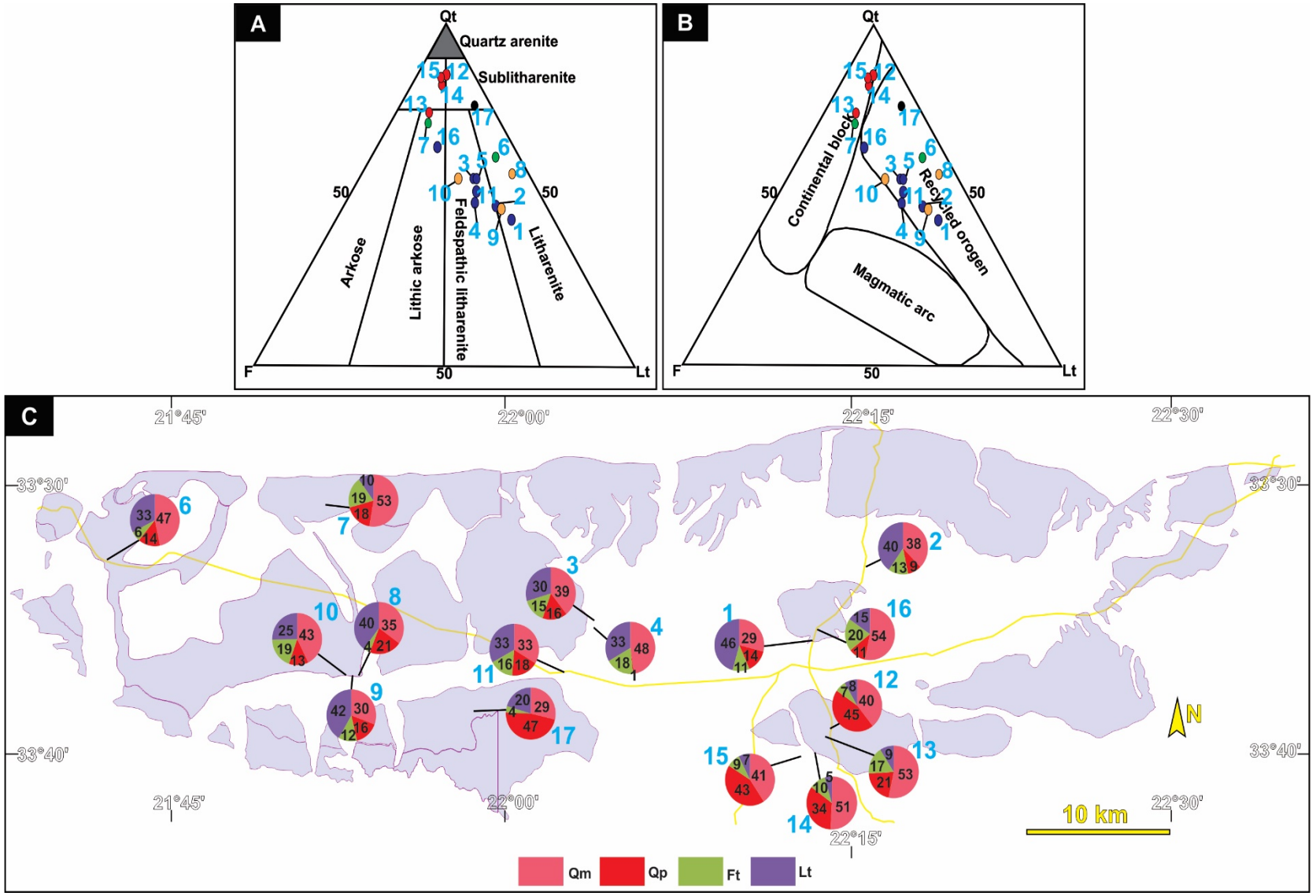

Figure 3.25. Sandstone QFL ternary plots for classification (A) (Folk, 1980) and provenance analysis (B) of 17 samples from the Oudtshoorn Basin (modified after Ingersoll et al. 1984; Dickinson 1985). Dots indicating the samples are coloured according to their locations in the basin: blue - centre; green - northwest; orange and grey (sample 17): southwest; red: south. C: sandstone compositional map based on point counting results. In C, numbers in the pie charts are given in %. Sample numbers are shown in blue next to the pie charts.

3.4. Palaeocurrent analysis

A total of 387 imbrication and 10 trough cross-bedding readings in the Oudtshoorn Basin were plotted in a total of 19 rose diagrams (Fig. 3.26), some of which are semi-regional summaries (like rose E; see below). The mean palaeocurrent vectors of 10 rose diagrams are also shown on the map of the Oudtshoorn Basin (Fig. 3.27).

Palaeocurrent measurements in the gravelly facies in the northern (roses A and B and corresponding arrows in Figs. 3.26 and 3.27), eastern (rose C), south-eastern (rose D) and southern (rose E) parts of the basin show bimodal palaeocurrent distributions. Mean vector azimuths (V.A.) in these roses are orientated towards S and SW in the northern facies, towards SW in the eastern facies and towards NE in the south-eastern and southern facies (Figs. 3.26 and 3.27). Palaeocurrent measurements at site D6_S4 (rose F in Fig. 3.26) in the west indicates palaeocurrent from NE to SW, low St.D. and V.M., and high C.R. However, this rose diagram may not be representative of the western part of the basin, because limited accessibility only allowed for 8 measurements in two, poorly exposed gravelly facies at this site (possibly part of architectural element GB, Figs. 3.2E and 3.13).

Imbrication measurements from architectural element GB (roses G and H in Fig. 3.26) in the south-south western part of the basin (Fig. 3.27) show polymodal distribution, high V.M. and St.D. and low consistency ratio. Site D17_S2.1 (rose H in Fig. 3.26) is located stratigraphically above and 142 m NW from site D17_ S1.1 (rose G in Fig. 3.26). There is a ~100˚ change in the overall palaeocurrent direction up the stratigraphy from ~156 to ~55˚ azimuth. It is difficult to establish their vertical distance, due to outcrop quality and structural dip of strata at both locations. Architectural elements GS in the south of the basin display two main trends: 1. low consistency ratio (C.R) and vector magnitude (V.M), and high standard deviation (St.D.) (roses I , J , K, L, M); 2. high C.R, low St.D and V.M (roses N, O, P, Q). Rose R displays low CR, high V.M and St.D; it's deviation from the two patterns could be a result of the large number of measurements relative to the other localities. Rose Q in Figure 3.26 summarizes all palaeocurrent measurements at the sites

(roses I, J, K, L, M, N, O, P, Q, R) that are in the southern-central cluster of the basin (Fig. 3.27) and indicates palaeocurrent from south to north, high St.D. and V.M. and low C.R., and polymodal distribution.

Very few and faint foresets in trough cross-bedded sandstones (facies St) present at site D4_S4 (centre-east of the basin) suggest palaeoflow from the east (azimuth ~230˚). Although the resultant vector in facies St (architectural element CH-2) at site D8_S7 has a 94˚ azimuth, the rose diagram (rose V in Fig. 3.26) displays a NE-SW bimodal trend, which agrees with axis orientation of the rare trough cross-beds at this site, where the plan view exposure of some of the foresets suggest palaeoflow from ~ENE to WSW.

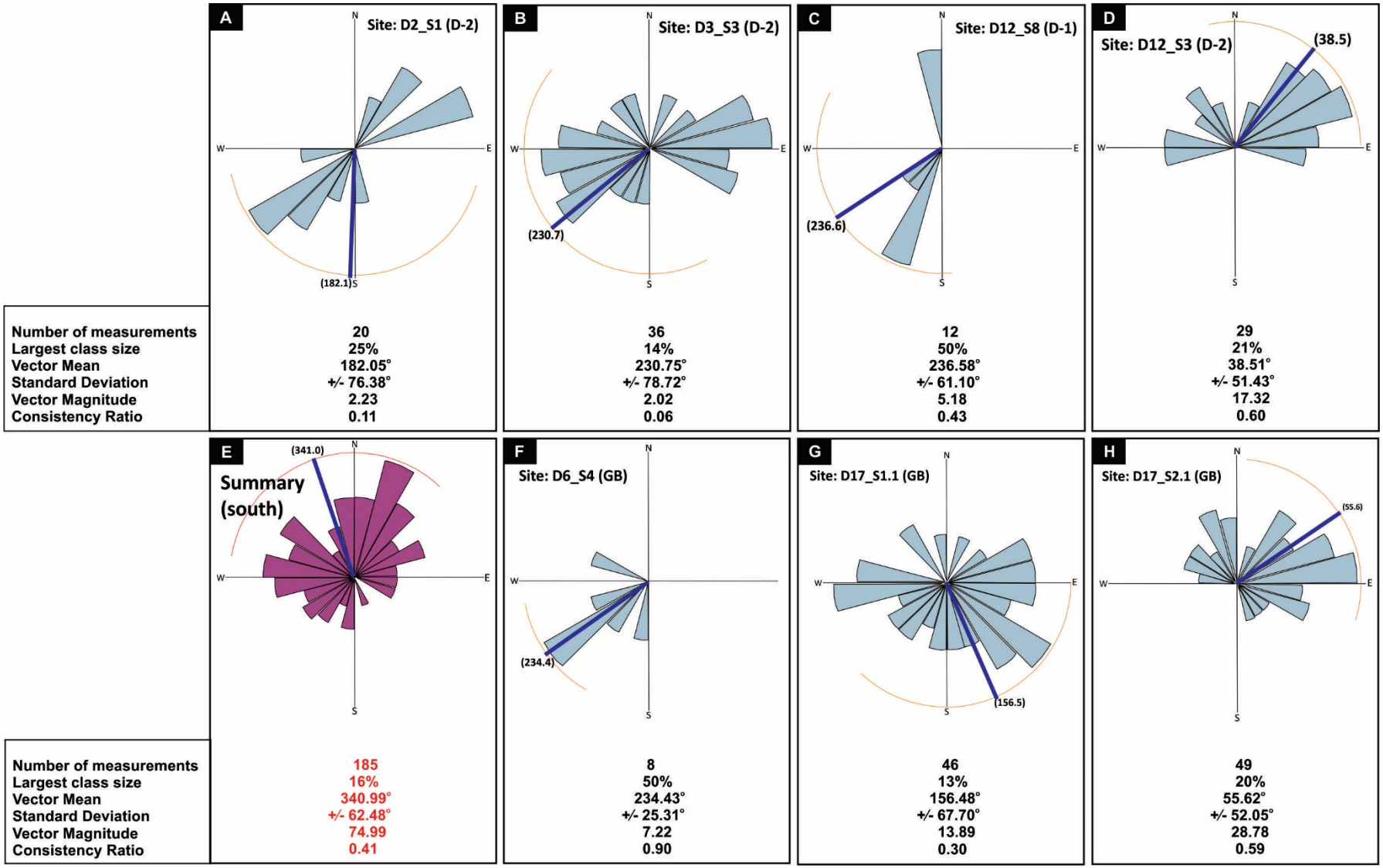

Figure 3.26. Rose diagrams of clast imbrication measurements taken in gravelly and sandy facies associations in the Oudtshoorn Basin (D, GS, GB and CH-2). Except for rose V, readings from planar cross-bedding, trough cross-bedding and plant fossil orientations are not represented here because they are very rare.

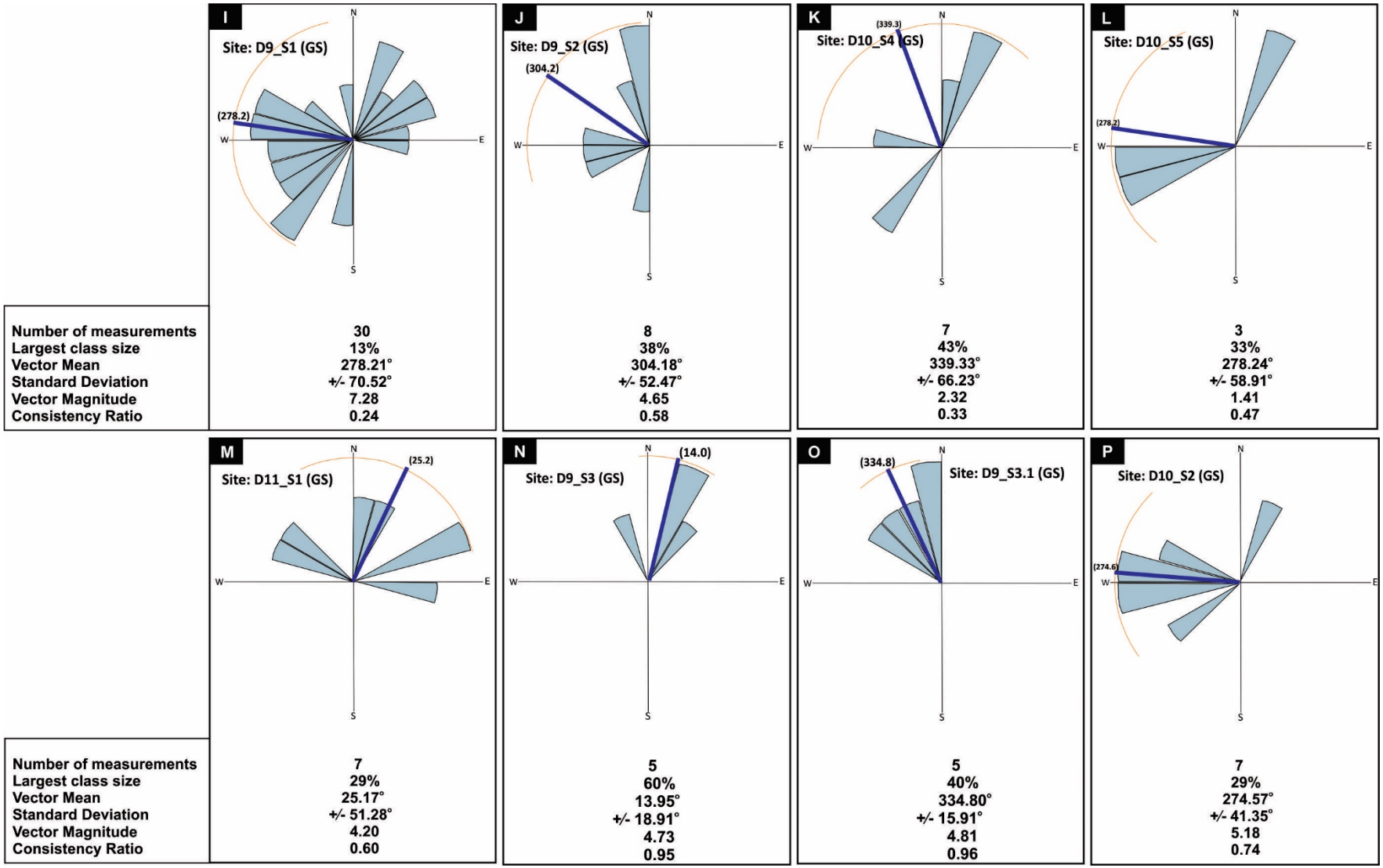

Figure 3.27. Rose diagrams of clast imbrication measurements taken in gravelly and sandy facies associations in the Oudtshoorn Basin (D, GS, GB and CH-2). Except for rose V, readings from planar cross-bedding, trough cross-bedding and plant fossil orientations are not represented here because they are very rare.

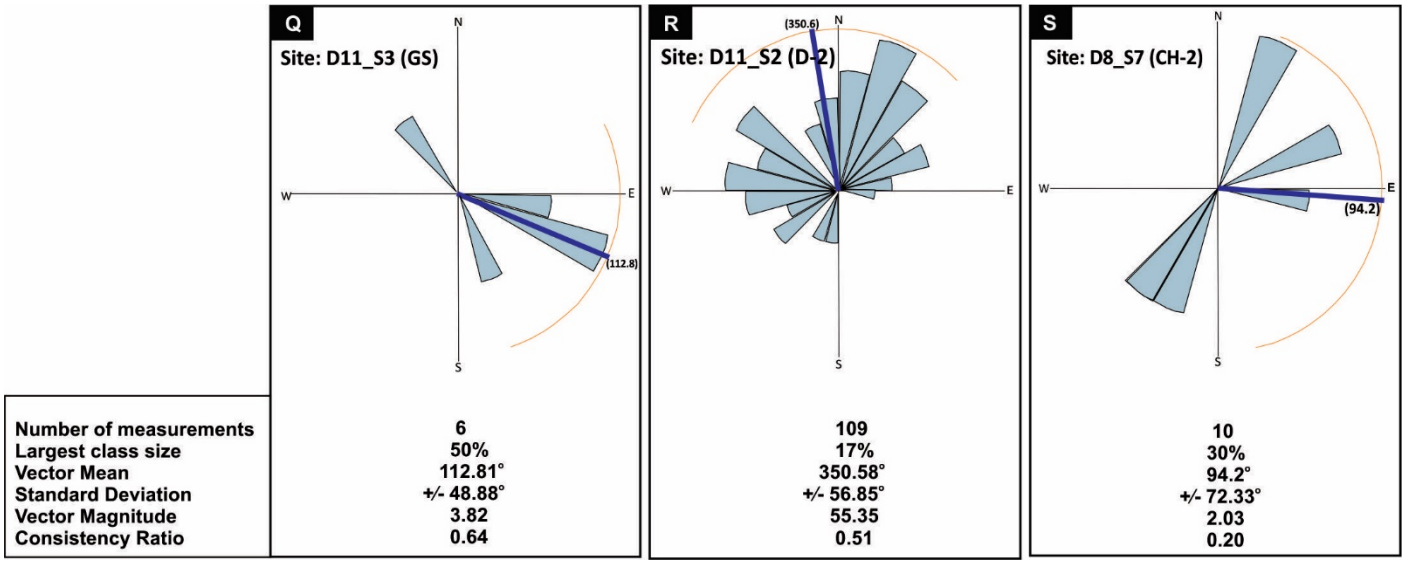

Figure 3.28. Rose diagrams of clast imbrication measurements taken in gravelly and sandy facies associations in the Oudtshoorn Basin (D, GS, GB and CH-2). Except for rose V, readings from planar cross-bedding, trough cross-bedding and plant fossil orientations are not represented here because they are very rare.

Figure 3.29. Palaeocurrent map of the Oudtshoorn Basin. Arrows indicate mean palaeocurrent vectors. Purple arrow in the south represents the summary of the mean vectors for a cluster of closely spaced sites. Numbers and letters next to arrow represent the number of measurements and corresponding rose diagrams in Figure 3.26. Some vectors (south-centre of the basin) were not shown as they are too closely spaced, which would render them unreadable. Measurements from facies St are marked with a dashed line and arrows (see text for details).

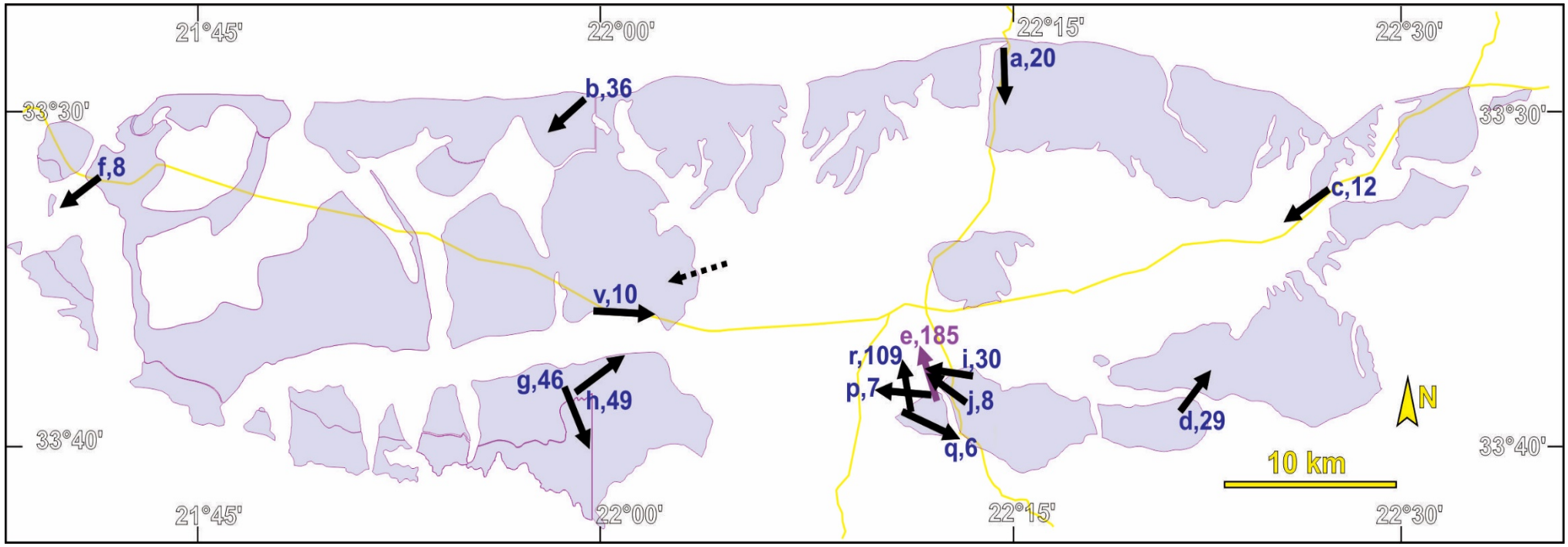

3.5. Geochemistry

3.5.1. X-Ray fluorescence

Major oxide XRF data of the of the Oudtshoorn Basin samples are presented in Figures 3.28, 3.29 and Appendix Table 7.3. Silica and alumina are the most abundant oxides by weight percentage (75.4±9.77 and 10.8±3.90, respectively), followed by sodium, iron and potassium oxides (3.8±2.18, 2.9±1.43 and 1.9±0.70, respectively). Calcium oxide standard deviation is enhanced by outlier samples 7, 13 and 22: average wt% CaO changes from 0.5±0.64 to 0.4±0.35 when these samples are excluded from the calculations (Appendix Table 7.3). The high CaO values in samples 7 and 13 are attributed to their calcite cement (Appendix Fig. 7.4K) as well as the associated gypsum, because both samples were taken from deposits that are interbedded with post-depositional (Recent) gypsum layers that are <3 cm in thickness. Major oxide ratios K_2O/Na_2O, Al_2O_3 and SiO_2 were used as proxies for evaluating sediment provenance (Fig. 3.28), maturity (SiO_2/Al_2O3, Appendix Table 7.4) and palaeoclimate (Fig. 3.29). Average wt% Si_2O is higher in sandstones than in mudstones (79,7±5,03 vs 62,1±9,5), whereas Al_2O_3 averages show an opposite (15,8±4,7 for mudstones and 9,3±2,4 for sandstones). Mudstones show a more variable SiO_2 content and a broader silicate modal compositional spectrum than that of the sandstones (Fig. 3.28). The SiO_2/Al_2O_3 ratio ranges from 2.22 to 17.6 (Appendix Table 7.4), in samples 1 and 12, respectively, with an average 8.35±3.58, reflecting low-moderate maturity (Roser et al., 1996); the K_2O/Na_2O ratio is higher in the sandstones than in the mudstones (4,02±2,74 vs 1,62±0.99). The high K_2O/Na_2O and SiO_2 contents of the Oudtshoorn Basin sandstones (Fig. 3.28) are similar to those in samples derived from passive margin sources based on global comparative data shown in Bathia (1983) and Roser and Korsch (1986).

Calculated CIA values range between 65.7 and 88.7 (average of 75.9±6.3; Appendix Table 7.4), fall within the intermediate weathering field (Fig. 3.29B), and trend toward the illite compositional zone (Nesbitt and Young, 1982). The trend is poorly defined for mudstones due to the small number of fine-grained samples that could be collected from the study area. Molar CIA (CIA_{mol}) values

range between 1.3-5.6 (average of 2.7±1.2; Appendix Table 7.4) and the samples plot in the arid and subtropical fields in the aridity plots (Fig. 3.29A). The ICV values range from 0.28 to 5.23 (average 0.75±0.21; Appendix Table 7.4). The weathering indexes show no considerable difference between mudstones and sandstones (for average values see Appendix Table 7.4).

3.5.2. X-Ray diffraction

XRD analysis focused on the identification of clays, due to their importance as palaeoclimate proxies; however, other non-clay phases present were also noted (Appendix Table 7.5 and Appendix Fig. 7.5). Clay fraction from the samples were separated and analysed from mudstone and very fine-grained sandstone samples only.

Qualitative analysis of eight powdered samples yielded the following mineralogical results, in order of abundance: quartz; micas (muscovite, phlogopite, lepidolite); illite; smectites (montmorillonite, sauconite, beidellite, nontronite); vermiculite; mixed layer clays (chlorite-vermeculite-montmorrilonite); oxides (ilmenite, hematite, goethite); feldspars (microcline, albite, orthoclase); pyrophyllite; gypsum, and kaolinite. No major differences were observed with respect to sample lithological composition (mudstone vs. sandstone) or their location within the basin.

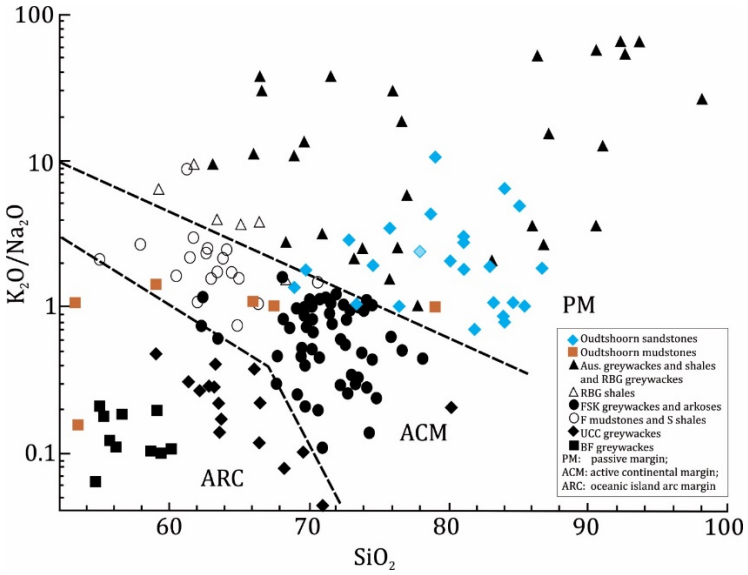

Figure 3.30. Harker plot for tectonic discrimination of Oudtshoorn sandstones and mudstones based on their K2O, Na2O and SiO2 contents. Data from this study were superimposed onto published data quoted in Roser and Korsch (1986). Aus: Australian; RBG: Robertson Bay Group; Franciscan, Santa Ynez and Kodiak; F and S: Franciscan and Santa Ynez; UCC: Uyak/Cape Current; BF: Baldwin Formation.

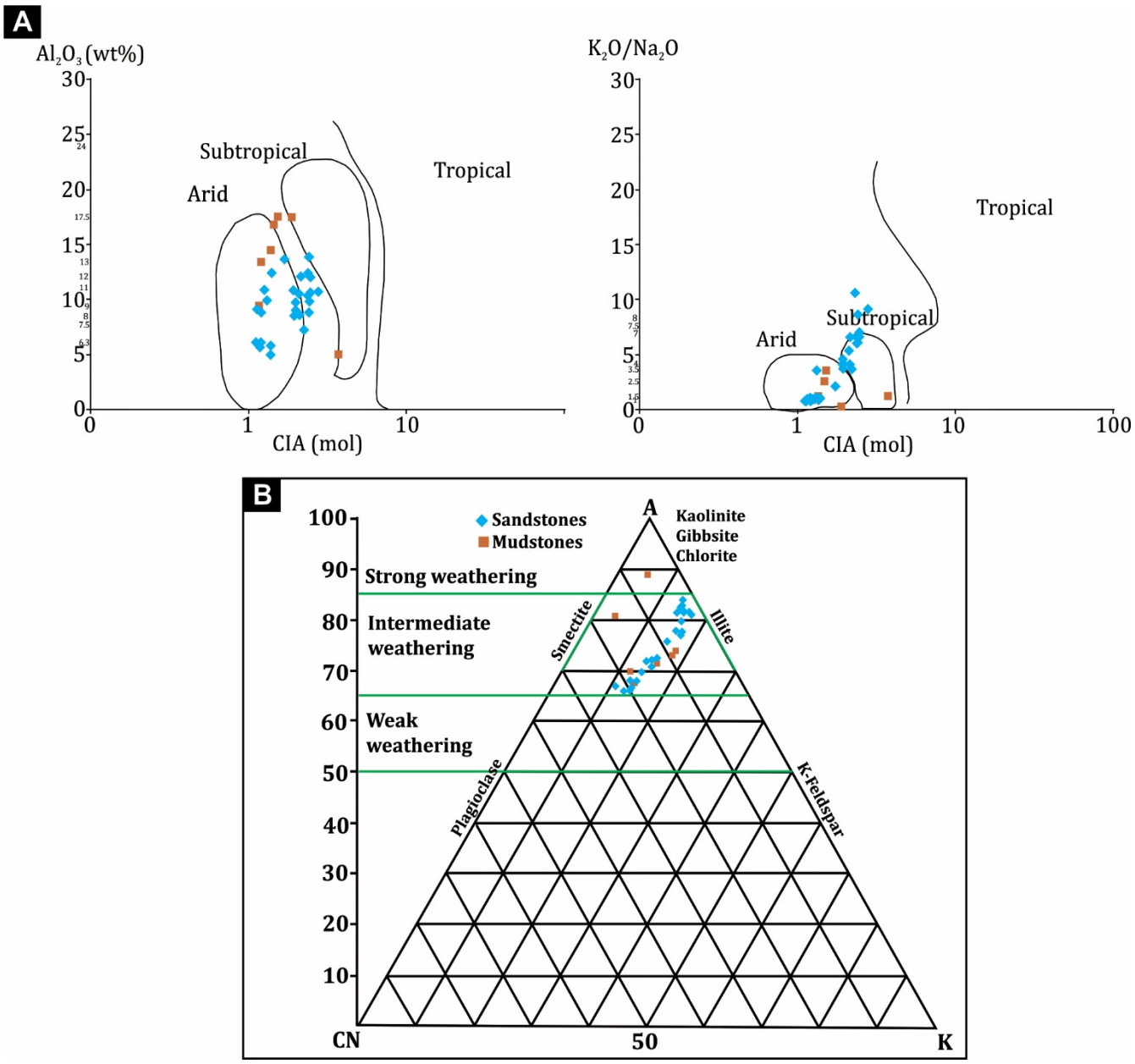

Figure 3.31. A: K2O/ Na2O and Al2O3 vs CIAmolar aridity plots of samples from the Oudtshoorn Basin, which straddle the subtropical and arid fields (modified from Goldberg and Humayun, 2010). B: Al2O3-(CaO*+NaO)-K2O (A-CN-K) diagram of CIA and weathering trends of samples in the study area (modified after Nesbitt and Young, 1984 and Fedo et al, 1995).

4. Discussion

4.1. Facies interpretation

4.1.2. Gravelly facies

Facies Gm-1 and Gh-1 dominate the cobble-boulder D-1 and D-2 architectural elements, and occur exclusively close to the present margins of the Oudtshoorn Basin (see Fig. 3.20). Texturally immature, very poorly-to-poorly sorted breccias with facies Gmm-1 and Gcm-1 are indicative of proximal debris and non-cohesive hyperconcentrated flows with varying amounts of matrix. The sediment could have been sourced from unconsolidated colluvium during major flood events (Miall, 1985, Blair and McPherson, 1994; Benvenuti, 2003; Nichols, 2009). The association of amalgamated Gcm-1 and Gch-1 beds and the erosional relationship with Scm lenses in very poorly-poorly sorted cobble-boulder breccias (site D12_S8, Fig. 3.1 B) suggest multiple pulses (S1 to S4 in the Fig. 3.4) in non-cohesive hyperconcentrated flows. The occurrence of facies Gi-1 in S5 at this site and the erosional relationship with Scm lenses indicate traction currents, whereas the non-erosional Gmm-1 lithofacies at site D3_S2 (Fig. 3.1C) and possibly at D5_S1 and D2_S6 (Figs. 3.1A and D) suggest debris flow lobes, although the bounding surfaces and other stratigraphic relationships at these two sites could not be conclusively assessed due to lack of suitable exposure.

Similarly, Gcm-1-Gmm-1-Gch-1/2-Gi-1/2 and subordinate Scm lenses associations in crudely bedded or graded cobble-boulder conglomerates (e.g., Figs. 3.1F, 3.5C-D and 3.6) also indicate traction currents (Miall, 1985, Blair and McPherson, 1994; Benvenuti, 2003; Nichols, 2009). However, the increased clast roundness (D-2) suggests more distal sources, or more abrasion and recycling of the material prior to deposition than the breccia facies (D-1). Grading and conglomerate-Scm lenses couplets close to the upper bedding surfaces (in normally graded beds, e.g., lower bed in Figs. 3.5C and D) could indicate density-driven layered flows dominated by basal clast collisions, and a more turbidity-dominant upper reach characterised by Gch-2 and Scm (Benvenuti, 2003). Basal alignment of clasts in normally graded Gcm-Gch-1 (and less frequently

Gi-2) facies conglomerates could indicate horizontal laminar shear flow (Benvenuti, 2003; Nichols, 2009).

Pebble-cobble conglomerates (facies Gt and Gcm-2) with concave-up basal scours and overlain by facies Gcm-2/Gh-2 constitute channel scours and traction flows in the formation of gravel bars. Compound gravel bars composed of Gp-Sp/Gch-2-Scm (e.g., Figs. 3.2 and 3.12) couplets and are typically capped by Sm/Scm (e.g., Figs. 3.2D and F), indicating waning stages of gravely bar deposition, possibly after flood events (Miall, 1985; Nichols, 2009). Deep scours filled by Gcm-2 and Gi-2 that are cut into facies Sm/Scm and G-2 indicate highly erosive events resulting in the channelling and erosional "palaeo-potholes" (e.g., Figs. 3.10 and 3.13). Couplets of horizontally stratified and graded facies Gh-2 and Scm in pebbly breccias (Figs. 3.2A and 3.7) probably resulted from bedload deposition of rapid and turbulent upper regime flows. Facies Scm indicates decrease in flood flow energy, and its truncated upper part and succeeding coarse-grained gravelly facies suggest episodic reoccurrence of high energy, erosive flood events (Fig. 3.2A).

4.1.2. Sandy and fine-grained facies

Sandy facies are associated with all lithofacies, and the type of association is a function of the transportation and depositional processes and their energy levels (Miall, 1985). Medium-coarse grained Sm and Scm commonly overlay G-1 ad G-2 facies (e.g. Figs. 3.2G and 3.6) or are enclosed in gravelly facies (Fig. 3.8), suggesting waning stages or decrease in flow regime. In sandy deposits, beds are typically characterised by basal medium-coarse grained Scm/Sm/St overlain by and terminating in Sm, and less frequently Sp and Sh (Figs. 3.2I, J and 3.16). The association St-Sm-Sp is indicative of migrating sand dunes in high and intermediate energy currents. Lenses and ribbons of faint basal St or Scm vertically changing into Sm, engulfed in F-facies result from short-lived high energy pulses in a predominantly low energy environment, likely during flooding events (Miall, 1985, 2013). They may form as a result of a loss in discharge energy of a confined flow, as it becomes unconfined (by breaking out of the main channel), hence forming sheet floods (Miall, 2013). Charcoal fragments and thin laminae in sandy beds (e.g., Figs. 3.3B and E) within gravelly

facies were probably deposited during the waning stages of flood events, and point to the occurrence of wild fires (Muir et al., 2015).

Fine-grained facies Fl, Fm and Fp (e.g., Figs. 3.3, 3.16 and 3.17) are found mostly in the centre of the basin, with the exception of site D17_SZ in the southwest (see map in Fig. 3.20). These facies may co-occur with tabular sheets or lenses of sandy facies (e.g. Figs. 3.17 and 3.18) and less frequently with gravelly facies (e.g. G-2 in Figs. 3.19 and Appendix Fig. 7.2). Although, the internal geometry of these deposits is commonly obscured by surface weathering, facies Fm seems to be the most common. The absence of sediment deformation structures may suggest that the original sediment was bioturbated after deposition (e.g. Fig. 3.3D; cf. Miall, 1985). Evidence for subaerial exposure of fine-grained deposits and development of soils (Fisher and Nichols, 2013) is shown by the rare carbonate nodules and greenish-grey mottled appearance of facies Fp (Fig. 3.3A).

4.1.3. Architectural elements

Architectural elements contain distinctive lithofacies assemblages with 3-D arrangements specific to various hydrodynamic processes, and are therefore the building blocks for the reconstruction and interpretation of depositional systems (Miall, 1985). This study identified nine architectural elements, the relative abundance of which seems to be associated with their location relative to the basin margins, as discussed below.

Architectural element D corresponds to the coarsest-grained facies associations and occurs exclusively at or close to the basin margins (Fig. 3.20). Massive D-1 breccias in the northern basin margin (D5_S1, D3_S2, D2_S6 in Figs. 3.1D, A and C respectively) are interpreted as rapid deposition of hyperconcentrated and laminar debris flow lobes with varying matrix content, resulting from hydration of slope colluvium during catastrophic high discharge events, and short travel distances (Bull, 1972, Nemec and Steel, 1984, Blair and McPherson, 1994). Site D12_S8 in the east (Figs. 3.4 and 3.20) shows multiple surges of debris flows (S_1-S_5) interpreted to having been by: basal traction, shown by crude normal and reverse grading (better observed in S_1-S_3, Fig. 3.4D); turbulent flows, resulting in imbrication of basal clasts (S5, Fig. 3.4B) (Nemec and Steel, 1984; Liu

and Cui, 1999). Crudely-bedded D-2 conglomerates (D3_S3 in Fig. 3.1F and D2_S1, not shown) show imbrication and basal clasts commonly show alignment subparallel to the resultant palaeoflow (Fig. 3.26B), evidencing highly sheared laminar debris flow (Nemec and Steel, 1984; Liu and Cui, 1999). In spite of the geographical proximity (northern basin margin, at about $22^{0}00$, see Figs. 1.1B and 3.20) deposits at sites D3_S3 (D-2) and D3_S2 (D-1) have different sediment compositions (Figs. 3.23A and 3.24A) and structural dips (~35^{0}E vs ~35^{0}N) and represent distinct sedimentary processes, which were mostly likely diachronous. As no imbrication was observed at site D3_S2 (Fig. 3.1C), a comparison of palaeocurrents is not possible to further support this assumption. Furthermore, no stratigraphic correlation (i.e. a common stratigraphic marker) could be established between the two sites form the field observations.

Architectural element D2 comprising massive cobble-boulder conglomerates in the east (D12_S7, Fig. 3.5), south (D11_S2, Fig. 3.6) and south-east (D12_S2 and D12_S3, see Fig. 3.20 and for locations, Fig. 1.1B) associated with stratified sandy lithofacies (waning traction flow), show grading and stratification locally (e.g. Figs. 3.5C and D), imbrication (e.g. Fig. 3.26D), and are interpreted as braided alluvial fan deposits (Bull, 1972; Collinson, 1996). Vertically amalgamated gravelly bedforms (GB) occurring within D-2 element (Fig. 3.6) point to the formation of compound bars during catastrophic, periodic flooding events of these gravelly streams. At the waning stages of these floods, sandy lenses were deposited (Nemec and Steel, 1984; Collinson, 1996).

Breccias and conglomerates in architectural element D along the northern margin of the basin are interpreted as proximal debris flow lobes deposited downdip of alluvial fan apexes (Bull, 1972; Collinson, 1996; Blair and McPherson, 1994). The cobble-boulder D-2 conglomerates (facies Gm-1, Gh-1, Gi-1 and G-2) in the south-east and south-centre of the basin indicate high energy, sediment poor flows, pointing to deposition on fluvial fan surfaces (Collinson, 1996). The multi-storey sheet architecture (e.g. Fig. 3.6) and the absence of element F points to high-energy mobility of the gravelly channels (Collinson, 1996).

Architectural element GS has three main geometries, as explained in the Results section. The strong stratification and grading of the breccia-sandstone couplets (type 1 geometry), with sharp planar or erosional bounding surfaces between couplets (Fig. 3.2A) are interpreted as sheets in distal unconfined mixed gravel-sand, deposited under turbulent upper regime flows (Blair and McPherson, 1994; Collinson, 1996). Type 2 geometry (e.g. Fig. 3.10) are interpreted as channelized fan lobes formed on mid fluvial fans (Collinson, 1996) and suggest highly erosive, fluidised flows formed during high discharge events (Blair and McPherson, 1994; Collinson, 1996). The sandy lenses mark the waning stages of each lobe depositional events, while channel scour fills and erosional potholes reveal the highly erosive nature of proceeding events. Type 3 geometry in the GS sheets are typically massive with small channel scour fills and localised normal grading (Fig. 3.8), associated with elements F (Fig. 3.11), SB and CH-2 (Figs. 3.8, 3.14 and 3.16). These are interpreted as streambed composite gravel-sand bars with small cross-cutting gravel channels in deep gravel rivers, or streambed bars developed during flash flood events (Miall, 1985; Collinson, 1996). This element overlies CH-2 at sites D23_S3/D13_S2 and D1_S1, 420 meters north of it (Figs. 3.16/3.8 and 3.14 respectively; see also Fig. 3.20), in centre of the basin in which fine-grained facies predominate (Fig. 3.20). It was not possible to confidently assess whether the bounding surface between GS and CH-2 is erosional, or the presence, depth and extent of erosional scours. The existence of at least two cycles of coarsening upward successions in the basin centre (at sites D1_S1, D23_S3 and D13_S2 – see Results chapter) is interpreted as resulting from a change in depositional gradient and hence transport energies, or because of changes in sediment supply possibly due to increase in discharge (Miall, 1985; Collinson, 1996; Nichols, 2009). The formation of elements CH-2 and F is favoured by gentle gradients, whereas element GS is more indicative of steeper gradients or greater sediment supply and shorter distance from source rock.

Compound gravel bars (element GB) in pebble-cobble conglomerates show amalgamated geometry and are associated with fine grained facies (e.g. Figs. 3.9, 3.12, 3.13 and 3.19), and are interpreted as gravely bars in mixed gravel-sand rivers (Miall, 1985; Collinson 1996). The laterally

accreted and vertically stacked bar sets at sites D6_S4 (Figs. 3.2E and 3.13) and D12_S6 (Fig. 3.9), west and east of the basin (Figs. 1.1B and 3.20) suggest braided gravelly streams, possibly in distal fan areas (Miall, 1985; Collinson 1996). The dip of the strata (average 25^0 N-NW) at and the geographical proximity (see Fig. 3.20) of sites D12_S7 (D-2, Fig. 3.5), D12_S6 (GB and SB, Fig. 3.9) and D12_S8 (D-1, Fig. 3.4) could suggest a stratigraphic relationship between the three facies (younging from D-2-GB/SB/D-1); however, no direct field evidence was found to support this possibility. The lateral accretion and vertical amalgamation geometry of GB sets engulfed in element F at site D17_S2_Z in the southwest of the basin (Figs. 3.19 and 3.20) indicate channel avulsion, possibly because of upstream channel belt abandonment or changes in tectonic/climatic regimes (Miall, 1985; Fisher and Nichols, 2013).

Element CH-1 (Figs. 3.12 and 3.20) are laterally continuous tabular sandstone beds, and are interpreted as unconfined channel flows resulting from flash floods (Miall, 1985), with each bed representing individual events. The upward coarsening succession resulting from the association with GB bars alludes to the variations of sediment supply, progradation of source areas (possibly fluvial fans in the south of the basin) or tectonically driven changes to the depositional gradient (Miall, 1985; Fisher and Nichols, 2013). The vertically stacked sandy beds of element CH-2 (Figs. 3.14 to 3.16), found in the centre of the basin (Fig. 3.20), are interpreted as bedload sandy sheets or bars deposited at fluctuating energy levels (Miall, 1985; Collinson, 1996). Although some lateral accretion is apparent at site D4_S4 (Fig. 3.15), the incomplete section and the lack of palaeocurrent indicators makes it difficult to interpret these beds as laterally accreted bars. Element F represent floodplain deposits within which crevasse splays (CS) were deposited during high energy flash floods events (Miall, 1985; Collinson, 1996). Similarly to GB and F in Figure 3.19, the erosional relationship between CH-2 and F suggests channel avulsion, resulting from changes in allogenic (tectonic or climatic) factors, or due to channel abandonment driven by autogenic processes (Miall, 1985; Collinson, 1996; Fisher and Nichols, 2013).

4.2. Sediment grain texture, composition and palaeocurents

The gravelly facies in the Oudtshoorn Basin display highly variable grain sizes, which seems to be controlled by architectural element type and hence processes (see Figs. 3.21 and 3.22). Element D-2 in the north and east of the basin display the largest clast sizes, and the largest populations of cobble and boulder-sized clasts, followed by D-1 (Figs. 3.22 and 3.21). The maximum clast size in facies D-2 is smaller in the south of the basin, and there is also a decrease in proportion of cobble and bounder-sized clasts. Pebble-cobble facies are noted in the centre, west, east and south of the basin (Fig. 3.22). The relatively greater clast size in the northern and eastern facies (except for GB) indicate higher energy regimes and steep gradients, whereas greater roundness predominantly in the south of the basin could suggest gentler gradients and greater transport distances. The large grain size difference in the upward coarsening succession at sites D1_S1 and D23_S3 (Figs. 3.14 and 3.13), from sand-pebbly sand to pebble-cobble conglomerate (Figs. 3.21 and 3.22) indicates an increase in transport energy over time, possibly due to the aggradation of coarse-grained facies towards the basin centre resulting from upstream gradient, or an interplay of sediment availability vs. starvation periods driven by climate (Miall, 1985; Fisher and Nichols, 2013). Elements GS and GB in the west, east and south of the basin also indicate high transport energy and relatively steep gradients, compared to the finer grained facies.

The finer grained architectural elements (CH-2, CS, F) in the centre of the basin (Fig. 3.20 and 3.22) are interpreted as having been deposited on relatively gentler slopes by fluvial and overbank floodplain processes (Miall, 1985; Collinson, 1996).

The maximum grain size distribution in the basin is indicative of very high energy processes dominating closer to the basin northern and southern margins, and a relative decrease toward the centre and west. This can be attributed to be a function of depositional gradient or sediment supply, as a direct result of tectonic activity in basin margin areas and the climate contribution (Miall, 1985; Fisher and Nichols, 2013; Miall, 2013).

The palaeocurrents display general southerly and northerly directions close to the northern, southern, eastern and western basin margins. Most of data shows bi- or polymodal distributions (Fig. 3.26), which is attributed to the data collection procedure. The data at each site was not treated taking into consideration possible individual beds, bedsets or architectural elements mainly due to poor exposure. The spread of data could therefore represent, for example, geometrical arrangement of architectural elements within a bed or bedset (Potter and Pettijohn, 1963; Yagishita, 1997). The change of ~100˚ azimuth from site D17_S1.1 to D17_S2.1 could be an indicative of deposition on an alluvial fan, with each site hence representing different stages of deposition. The general palaeocurrent trend, from both north and south, toward the centre of the basin, where sandy fluvial and floodplain facies predominate, suggest a fluvial drainage parallel to the axis of the basin (Lock et al, 1975; Smoot, 1991). Trough cross-bedding at site D8_S7 in the centre of the basin (Fig. 3.27) and the geometry of element CH-2 at site D4_S4 also in the centre of the basin (Figs. 3.15 and 3.20), although insufficient, give an indication that this drainage pattern was directed to the centre and the axial river was flowing to the east. Based on the palaeocurrent data, it is suggested that site D4_S4 represents a tributary, whereas D8_S7 represents the main channel.

The predominance of quartzite clasts in the gravelly facies (Fig. 3.24A) could suggest that the source rock that surrounded the basin were most likely the quartzite rich stratigraphic units in the Cape Supergroup. Sites D2_S1 (D-2, N-NE), D3_S3 (D-2, N-NW) and D6_S4 (GS, far NW) display very similar composition and compositional abundances, despite their relative location (Fig. 3.24). Furthermore, sites D2_S1 (bedding dip at ~118/47 NE) and D3_S3 (bedding dip at ~140/40E) conglomerates show very similar clast size characteristics (Fig. 3.22) and are interpreted as having been formed by similar sedimentary processes (see section 4.1.3 above). A stratigraphic relationship is difficult to establish due to their geographical locations and lack of direct field evidence (see site locations in Figs. 1.1B and 3.20). The clast composition and modal abundances, together with palaeocurrent trends and the structural attitude of the beds at these three sites could indicate a

common sediment source north of the basin. It not possible, as explained above, to determine the relative ages of these deposits.

Clast angularity (Figs. 3.23B and 3.24B) is greatest in facies at or close to the northern (except sites D2_S1 and D3_S3) and eastern margins, suggesting short transport distances and steep gradients in accordance with the interpreted debris flow processes (Bull, 1972; Miall, 1985; Blair and McPherson, 1994). In contrast, the fluvial D-facies clasts close to the southern basin margin are predominantly rounded (Figs. 3.23B and 3.24B), suggesting greater transport distances and hence more distant sources that were positioned father to the south.

4.3. Petrography and geochemistry

The petrographic (Fig. 3.25B) and geochemical analysis (Fig. 3.28 and Appendix Tables 7.3 and 7.4) of sandstones in the study area point to provenance within passive margins (Fig. 3.28), recycled orogen and continental block (Bathia, 1983; Ingersoll et al. 1984; Dickinson 1985; Roser and Korsch, 1986). Samples in the south-east are mostly poorly sorted quartzitic sublitharenites and wackes (Fig. 3.25A and Appendix Table 7.2A), showing the highest percentage of polycrystalline quartz and total quartz, and lacking lithic fragments (Fig. 3.25C). The percentage of lithic fragments is greater in the centre (poorly to well-sorted litharenites and wackes) and west (poorly to moderately-sorted litharenites, wackes and arkoses) of the basin (Appendix Table 7.2B), and that of feldspar does not vary greatly throughout the samples (Fig. 3.25C). The greater compositional maturity of samples in the south (Fig. 3.25B) is interpreted to be a result of greater transport distances; alternatively, the sediment could have been sourced from quartz-rich source rocks (Ingersoll et al. 1984; Dickinson 1985). The high percentage of polycrystalline quartz can further support the second hypothesis; however the roundness of clasts in fluvial D-facies suggest that the two scenarios could have occurred simultaneously (i.e., greater transport distances from quartz-rich source rocks in the south). Samples in the rest of the basin display a relatively high percentage of sedimentary lithic fragments (Appendix Table 7.2B), hence suggesting a more heterogeneous

source. The mineralogical modal composition of sandstone samples point to recycled orogen source, which given the proximity of the Cape Fold Belt is a plausible result (Fig. 3.25) (Ingersoll et al. 1984; Dickinson 1985; Roser and Korsch, 1986). This composition reflects that of the source rock suites (i.e., predominantly Cape Supergroup), which are dominated by mature, quartz arenites (quartzites) which formed along passive continental margins in the Palaeozoic. It should be noted however, that the amount of feldspar could have been underestimated due to the associated high degree of alteration of the samples in general (Appendix Table 7.2B and Fig. 7.4).

Major oxide ratios and weathering indexes (CIA/CIAmolar) point to intermediate weathering (Fig. 3.29 and Appendix Table 7.4) and most likely arid to semi-arid palaeoclimates (Nesbitt and Young, 1984; Fedo et al., 1995). The greater occurrence of smectite-group minerals and mixed layer clays, and the relative lack of kaolinite and feldspars (Appendix Table 7.5), further supports moderate weathering and hence less likely humid climates (Singer, 1984; Chaudhri and Singh, 2012). Secondary oxidation due to post-depositional could be responsible for the presence of oxide phases in many samples (Du Preez, 1944, Bull, 1972, Blair and McPherson, 1994; also note weathering colour in photographs in Chapter 3.1).

The textural (Appendix Table 7.2A and Fig. 7.4), compositional (Appendix Table 7.2B) and chemical characteristics (e.g. low average SiO_2/Al_2O3, Appendix Tables 7.3 and 7.4) of the fine-grained facies point to overall low sediment maturity, which could indicating short transport distances and moderate chemical weathering (Ingersoll et al. 1984; Dickinson 1985; Roser, 1996; Shao et al., 2012).

5. Conclusion

The facies characteristics and geometries of sedimentary fill of the Oudtshoorn Basin with a northern fault bounded margin dominated by debris- and hyperconcentrated flows dominated alluvial fan deposits and a southern margin dominated by fluvially dominated alluvial fans, which might have been characterised by gravelly braided channels. Sandy and mixed load sand-gravel fluvial channel and floodplain facies occur in the centre of the basin and may have been part of an axial river. Floodplain and gravelly associations occur in the southwest and west of the basin.

Although, without age constraints, the spatio-temporal facies relationships could not be established, the following deductions can be made:

1. Depositional gradient (possibly two main palaeoslopes: northern and southern) was greater in the northern basin margin than in the south, and was possibly maintained by fault activity, whereas deposition on the south occurred on gentler slopes;
2. Sediments were sourced both locally (close to sites of deposition) and away from the basin margins. Source rock was dominated by quartzite; in the northern margin, sediments were also sourced from metaconglomerates, sandstone and slaty source rocks, presumed to be Table Mountain, Bokkeveld and Kango Groups;
3. The existence of a fluvial system in the basin centre (as suggested by Lock et al, 1975), likely to have been meandering, running along the axis of the basin (E-W), however not conclusively shown by the current data. These central channels and associated floodplain received sediments both from the north and southern margins, in additional to potential sources in the east of the basin;
4. Deposition was controlled by tectonic or climatic variations, which resulted in changes in sediment supply and progradation of facies. Tectonic activity via normal faults would promote an increase in accommodation space and the reduction in cross-sectional area of northern debris flow fans facies (cf. Holzforster, 2007). In turn, the drainage area of the southern fluvial fans

would be increased during periods of tectonic quiescence, given the inverse relationship between depositional gradient and fan surface area;

5. Sandstones are predominantly texturally and compositionally immature, hence point to a proximal source, possibly within the basin, however in the south, the more mature sandstones and roundness of the gravelly facies imply more distal sources.
6. Composite geochemical analysis (e.g., SiO_2/Al_2O_3 ratio) of sandstones and mudstones suggests low sediment maturity and hence relatively low chemical weathering;
7. Climate was likely arid/semi-arid with prevalence of catastrophic discharge events resulting in flooding and mass transport events. Evidence also points to wildfires, which were important for large scale evolutionary pattern in the flora especially in the Cretaceous.

Although geochronological studies constraining the broad stratigraphic relationships in the Oudtshoorn Basin are in progress (e.g., Muir, 2018, in press), it is suggested that additional high precision dating should be utilized if possible on drill core samples from various parts of the basin. Without systematic sampling of the facies associations identified in this study and constraining their relative stratigraphic ages, the evolution of the fill of the Oudtshoorn Basin and its relationship to the other Mesozoic grabens and half grabens of the southern Cape remain elusive. Furthermore, investigating possible geochemical, textural and mineralogical trends in the dated drill core samples could yield inferences on 1) whether the basin received first cycle vs. recycled detrital input, and 2) the impact of diagenesis (e.g., burial depths), topography, geomorphology, modern weathering, etc. n the geochemical proxies used in this study, and thus assess the robustness of the primary results of this study.

6. Reference list

Al-Farraj, A. and Harvey, A.M., 2005. Morphometry and depositional style of Late Pleistocene alluvial fans: Wadi Al-Bih, northern UAE and Oman. *Geological Society, London, Special Publications*, 251(1), pp.85-94.

Allen, J.R.L., 1983. Studies in fluviatile sedimentation: bars, bar-complexes and sandstone sheets (low-sinuosity braided streams) in the Brownstones (L. Devonian), Welsh Borders. *Sedimentary Geology*, 33(4), pp.237-293.

Bahlburg, H. and Dobrzinski, N., 2011. A review of the Chemical Index of Alteration (CIA) and its application to the study of Neoproterozoic glacial deposits and climate transitions. *Geological Society, London, Memoirs*, 36(1), pp.81-92.

Benvenuti, M., 2003. Facies analysis and tectonic significance of lacustrine fan-deltaic successions in the Pliocene–Pleistocene Mugello Basin, Central Italy. *Sedimentary Geology*, 157(3-4), pp.197-234.

Bhatia, M.R., 1983. Plate tectonics and geochemical composition of sandstones. *The Journal of Geology*, 91(6), pp.611-627.

Blair, T.C. and McPherson, J.G., 1994. Alluvial fan processes and forms. *Geomorphology of desert environments* (pp. 354-402). Springer, Dordrecht.

Boggs Jr, S. and Boggs, S., 2009. *Petrology of sedimentary rocks*. Cambridge University Press.

Bond, W.J. and Midgley, J.J., 2012. Fire and the angiosperm revolutions. I*nternational Journal of Plant Sciences*, 173(6), pp.569-583.

Bordy, E.M., Head, H. & Runds, M.J. 2016. Palaeoenvironment and provenance in the early Cape Basin of southwest Gondwana: sedimentology of the Lower Ordovician Piekenierskloof Formation, Cape Supergroup, South Africa. *South African Journal of Geology*. 119(2):399-414.

Brierley, G.J., Liu, K. and Crook, K.A., 1993. Sedimentology of coarse-grained alluvial fans in the Markham Valley, Papua New Guinea. *Sedimentary Geology*, 86(3-4), pp.297-324.

Bull, W.B., 1972. Recognition of alluvial fan deposits in the stratigraphic record. *Special Publications of SEPM*.

Chaudhri, A.R. and Singh, M., 2012. Clay Minerals as Climate Change Indicators—A Case Study. *American journal of climate change*, 1(4), pp.231-239.

Collinson J.D., 1996. Alluvial sediments (book chapter). *Sedimentary environments: process, facies and stratigraphy* (book, edited by Reading, H.G), pp.37-82.

Colombera, L., Mountney, N.P. and McCaffrey, W.D., 2013. A quantitative approach to fluvial facies models: methods and example results. *Sedimentology*, 60(6), pp.1526-1558.

Costa, J.E., 1983. Paleohydraulic reconstruction of flash-flood peaks from boulder deposits in the Colorado Front Range. *Geological Society of America Bulletin*, 94(8), pp.986-1004.

Costa, J.E., 1984. Physical geomorphology of debris flows. *Developments and applications of geomorphology* (pp. 268-317). Springer Berlin Heidelberg.

Cox, R. and Lowe, D.R., 1995. A conceptual review of regional-scale controls on the composition of clastic sediment and the co-evolution of continental blocks and their sedimentary cover. *Journal of Sedimentary Research*, 65(1).

Cox, R., Lowe, D.R. & Cullers, R.L. 1995. The influence of sediment recycling and basement composition on evolution of mudrock chemistry in the southwestern United States. *Geochimica Et Cosmochimica Acta*, 59(14):2919-2940.

De Klerk, W.J., 2008. A review of the occurrence of disarticulated Early Cretaceous sauropod dinosaur fossils from the Kirkwood Formation of the Oudtshoorn and Algoa Basins. Programme and abstracts. In Biennial Conference of the Palaeontological Society of South Africa, Matjiesfontein September (Vol. 2008, pp. 90-91).

Dickinson, W.R., 1985. Interpreting provenance relations from detrital modes of sandstones. *Provenance of arenites*, pp. 333-361. Springer Netherlands.

Dingle, R.V., 1973. Mesozoic palaeogeography of the southern Cape, South Africa. *Palaeogeography, Palaeoclimatology, Palaeoecology*, 13(3), pp.203-213.

Dingle, R.V., Siesser, W.G. and Newton, A.R., 1983. *Mesozoic and Tertiary geology of southern Africa*. Rotterdam: Balkema.

Du Toit, A.L., 1939. *The Geology of South Africa*. Oliver and Boyd.

Du Preez, J.W., 1944. *Lithology, structure and mode of deposition of the Cretaceous deposits in the Oudtshoorn area*. Nasionale Pers.

Fedo, C.M., Wayne Nesbitt, H. and Young, G.M., 1995. Unraveling the effects of potassium metasomatism in sedimentary rocks and paleosols, with implications for paleoweathering conditions and provenance. *Geology*, 23(10), pp.921-924.

Fisher, J.A. and Nichols, G.J., 2013. Interpreting the stratigraphic architecture of fluvial systems in internally drained basins. *Journal of the Geological Society*, 170(1), pp.57-65.

Folk, R.L. 1980. *Petrology of sedimentary rocks* (book). Hemphill Publishing Company.

Garzanti, E., Andò, S., France-Lanord, C., Vezzoli, G., Censi, P., Galy, V. and Najman, Y., 2010. Mineralogical and chemical variability of fluvial sediments: 1. Bedload sand (Ganga–Brahmaputra, Bangladesh). *Earth and Planetary Science Letters*, 299(3), pp.368-381.

Gibling, M.R., 2006. Width and thickness of fluvial channel bodies and valley fills in the geological record: a literature compilation and classification. *Journal of sedimentary Research*, 76(5), pp.731-770.

Goldberg, K. and Humayun, M., 2010. The applicability of the Chemical Index of Alteration as a paleoclimatic indicator: An example from the Permian of the Paraná Basin, Brazil. *Palaeogeography, Palaeoclimatology, Palaeoecology*, 293(1), pp.175-183.

Green, P.F., Duddy, I.R., Japsen, P., Bonow, J.M. and Malan, J.A., 2017. Post-breakup burial and exhumation of the southern margin of Africa. *Basin Research*, 29(1), pp.96-127.

Hillier, S., 2003. Quantitative Analysis of Clay and other Minerals in Sandstones by X-Ray Powder Diffraction (XRPD). *Clay mineral cements in sandstones*, pp.213-251.

Holzförster F., 2007. Alluvial fan systems in the Late Mesozoic Oudtshoorn Basin, South Africa, and their implications for basin development. Beringeria 37, pp.81-93.

Hooke, R.L., 1967. Processes on arid-region alluvial fans. The Journal of Geology, 75(4), pp.438-460.

Howard, J.L., 1993. The statistics of counting clasts in rudites: a review, with examples from the upper Palaeogene of southern California, USA. *Sedimentology*, 40(2), pp.157-174.

Ingersoll, R.V., Bullard, T.F., Ford, R.L., Grimm, J.P., Pickle, J.D. and Sares, S.W., 1984. The effect of grain size on detrital modes: a test of the Gazzi-Dickinson point-counting method. *Journal of Sedimentary Research*, 54(1), pp.103-116.

Koopmann, H., Franke, D., Schreckenberger, B., Schulz, H., Hartwig, A., Stollhofen, H. and di Primio, R., 2014. Segmentation and volcano-tectonic characteristics along the SW African continental margin, South Atlantic, as derived from multichannel seismic and potential field data. *Marine and Petroleum Geology*, 50, pp.22-39.

Lindsey, D.A., Langer, W.H. and Van Gosen, B.S., 2007. Using pebble lithology and roundness to interpret gravel provenance in piedmont fluvial systems of the Rocky Mountains, USA. *Sedimentary Geology*, 199(3-4), pp.223-232.

Liu, G. and Cui, Z., 1999. Sedimentary macro-structures and forming mechanism of debris flow. *Chinese Geographical Science*, 9(1), p.33.

Lock, B.E., Shone, R., Coates, A.T. and Hatton, C.J., 1975. Mesozoic Newark type sedimentary basins within the Cape Fold belt of southern Africa. *Proc. Int. Congr. Sedimentol., 9th*, pp.217-225.

Lock, B.E., 1978. The Cape Fold belt of South Africa; tectonic control of sedimentation. *Proceedings of the Geologists' Association*, 89(4), pp.263-281.

Loubser, M. and Verryn, S., 2008. Combining XRF and XRD analyses and sample preparation to solve mineralogical problems. *South African Journal of Geology*, 111(2-3), pp.229-238.

Marsh, J.G., 2016. New evidence for the correlation of basalts of the Suurberg Group with the upper part of the Karoo basalt sequence of Lesotho. O*rigin and Evolution of the Cape Mountains and Karoo Basin* (pp. 59-65). Springer, Cham.

McLachlan, I.R. and McMillan, I.K., 1976. Review and stratigraphic significance of southern Cape Mesozoic palaeontology. S*outh African Journal of Geology*, 79(2), pp.197-212.

McLennan, S.M., Hemming, S., McDaniel, D.K. and Hanson, G.N., 1993. Geochemical approaches to sedimentation, provenance, and tectonics. *Geological Society of America Special Papers*, 284, pp.21-40.

McMillan, I.K., Brink, G.I., Broad, D.S. and Maier, J.J., 1997. Late Mesozoic sedimentary basins off the south coast of South Africa. *Sedimentary Basins of the World*, 3, pp. 319-376. Elsevier.

McPhee, B.W., Mannion, P.D., de Klerk, W.J. and Choiniere, J.N., 2016. High diversity in the sauropod dinosaur fauna of the Lower Cretaceous Kirkwood Formation of South Africa: implications for the Jurassic–Cretaceous transition. *Cretaceous Research*, 59, pp.228-248.

Miall, A.D., 1985. Architectural-element analysis: a new method of facies analysis applied to fluvial deposits. *Earth-Science Reviews*, 22(4), pp.261-308.

Miall, A.D., 1988. Architectural elements and bounding surfaces in fluvial deposits: anatomy of the Kayenta Formation (Lower Jurassic), southwest Colorado. *Sedimentary Geology*, 55(3-4), pp.233247-240262.

Miall, A.D., 2013. *The geology of fluvial deposits: sedimentary facies, basin analysis, and petroleum geology*. Springer.

Miall, A., 2014. *Fluvial depositional systems*. Springer.

Miall, A.D., 2016. The valuation of unconformities. Earth-Science Reviews, 163, pp.22-71.

Muir, R.A., Bordy, E.M. and Prevec, R., 2015. Lower Cretaceous deposit reveals first evidence of a post-wildfire debris flow in the Kirkwood Formation, Algoa Basin, Eastern Cape, South Africa. *Cretaceous Research*, 56, pp.161-179.

Muir, R.A. and Bordy, E.M., 2016. Stratigraphic framework for the Kirkwood Formation in the southern Cape region: invertebrate biostratigraphy and zircon geochronology. In: 19th Palaeontological Society of South Africa biennial conference, Stellenbosch University, 65p.

Muir, R.A., Bordy, E.M., Reddering, J.S.V. and Viljoen, J.H.A., 2017a. Lithostratigraphy of the Enon Formation (Uitenhage Group), South Africa. *South African Journal of Geology*, 120(2), pp.273-280.

Muir, R.A., Bordy, E.M., Reddering, J.S.V. and Viljoen, J.H.A., 2017b. Lithostratigraphy of the Kirkwood Formation (Uitenhage Group), including the Bethelsdorp, Colchester and Swartkops Members, South Africa. *South African Journal of Geology*, 120(2), pp.281-293.

Muir, R.A., 2018. The Stratigraphic Framework of the Uitenhage Group. PhD. thesis in preparation, University of Cape Town.

Nemec, W. and Steel, R., 1984. Alluvial and coastal conglomerates: their significant features and some comments on gravelly mass-flow deposits. *CSPG Special Publications, Memoir* 10, pp.1-31.

Nesbitt, H. and Young, G.M., 1982. Early Proterozoic climates and plate motions inferred from major element chemistry of lutites. *Nature*, 299(5885), pp.715-717.

Nichols, G., 2009. *Sedimentology and stratigraphy*. John Wiley & Sons.

Norrish, K. and Hutton, J.T., 1969. An accurate X-ray spectrographic method for the analysis of a wide range of geological samples. *Geochimica et cosmochimica acta*, 33(4), pp.431-453.

Petroleum Agency South Africa, 2008. Generalised chronostratigraphy of the Bredasdorp basin. Petroleum Exploration: Information and opportunities, 30 pp.

Potter, P.E. and Pettijohn, F.J. 1963. *Paleocurrents and Basin Analysis.* Springer.

Richardson, J.C., Hodgson, D.M., Paton, D., Craven, B., Rawcliffe, A. and Lang, A., 2017. Where is my sink? Reconstruction of landscape development in southwestern Africa since the Late Jurassic. *Gondwana Research*, 45, pp.43-64.

Roser, B.P. and Korsch, R.J., 1986. Determination of tectonic setting of sandstone-mudstone suites using content and ratio. *The Journal of Geology*, 94(5), pp.635-650.

Roser, B.P. and Korsch, R.J., 1988. Provenance signatures of sandstone-mudstone suites determined using discriminant function analysis of major-element data. *Chemical geology*, 67(1-2), pp.119-139.

Roser, B.P., Cooper, R.A., Nathan, S. and Tulloch, A.J., 1996. Reconnaissance sandstone geochemistry, provenance, and tectonic setting of the lower Paleozoic terranes of the West Coast and Nelson, New Zealand. *New Zealand Journal of Geology and Geophysics*, 39(1), pp.1-16.

Sciscio, L. and Bordy, E.M., 2016. Palaeoclimatic conditions in the Late Triassic-Early Jurassic of southern Africa: a geochemical assessment of the Elliot Formation. *Journal of African Earth Science*s, 119, pp.102-119.

Shao, J., Yang, S. and Li, C., 2012. Chemical indices (CIA and WIP) as proxies for integrated chemical weathering in China: inferences from analysis of fluvial sediments. *Sedimentary Geology*, 265, pp.110-120.

Shone, R.W., 1978. A case for lateral gradiation between the Kirkwood and Sundays River Formations, Algoa Basin. *South African Journal of Geology*, 81(3), pp.319-326.

Shone, R.W., 1976. The sedimentology of the Mesozoic Algoa basin. Unpublished MSc., University of Port Elizabeth.

Shone, R.W., 2006. Onshore post-Karoo Mesozoic deposits. *The Geology of South Africa*, pp.541-552.

Singer, A., 1984. The paleoclimatic interpretation of clay minerals in sediments—a review. *Earth-Science Review*s, 21(4), pp.251-293.

Shultz, A.W., 1984. Subaerial debris-flow deposition in the upper Paleozoic Cutler Formation, western Colorado. Journal of Sedimentary Research, 54(3).

Smoot, J.P., 1991. Sedimentary facies and depositional environments of early Mesozoic Newark Supergroup basins, eastern North America. *Palaeogeography, Palaeoclimatology, Palaeoecology*, 84(1-4), pp.369-423.

Viljoen, J.H.A., 1992. The stratigraphy of the Heidelberg/Riversdale Mesozoic Basin. *Inversion Tectonics of the Cape Fold Belt, Karoo and Cretaceous Basins of Southern Africa*. Balkema, Rotterdam, Netherlands, pp.77-84.

Walker, R., 1984. Facies models, Second. ed. Geological Association of Canada, Canada. Weltje, G.J. and von Eynatten, H., 2004. Quantitative provenance analysis of sediments: review and outlook. *Sedimentary Geology*, 171(1-4), pp.1-11.

Wildman, M., Brown, R., Watkins, R., Carter, A., Gleadow, A. and Summerfield, M., 2015. Post break-up tectonic inversion across the southwestern cape of South Africa: New insights from apatite and zircon fission track thermochronometry. *Tectonophysics*, *654*, pp.30-55.

Willis, J.P., Turner, K. and Pritchard, G., 2011. *XRF in the workplace: a guide to practical XRF spectrometry*. PANalytical Australia.

Wizevich, M.C. 1992. Photomosaics of outcrops: useful photographic techniques.

Yagishita, K., 1997. Paleocurrent and fabric analyses of fluvial conglomerates of the Paleogene Noda Group, northeast Japan. *Sedimentary Geology*, 109(1-2), pp.53-71.

7. Appendix

Raw and semi-processed palaeocurrent, clast count and other data are avaialbe upon request from the author or can be downloaded from here:

https://drive.google.com/file/d/1Pnm5afRvJ9hmy3u0_42basC4-mJJ3ODz/view?usp=sharing

7.1. Sample preparation for geochemical analysis

1. Rock samples were first crushed into chip sizes 2-5 mm in diameter using a laboratory jaw crusher (Fig. 7.1A). In suitable samples, a portion was used for clay separation.

2. Samples were then milled for 1-3 minutes into a fine powder using a disk-and-cylinder swing-mill (Fig. 7.1B). After milling, samples were ready for XRD analysis.

3. Exactly 2 g of powder was separated, dried at 100^0C and then heated at 1000^0C for at least four hours (Fig. 7.1C), before 0.7 g of it was mixed with flux (Fig. 7.1D) and placed in fusion disks for XRF analysis.

4. Clay separation of suitable samples was done via wet separation. Using 64 µm and 32 µm sieves, the cuttings were repeatedly washed so that the clay-sized potion was collected into a container (Fig. 7.1E).

5. The clay portion was allowed to settle to the bottom of the container for at least 48 hours, and then transferred onto glass slides using a syringe (Fig. 7.1F). Finally, samples were allowed to dry at room temperature and were then submitted for XRD analysis.

Crushing and milling apparatus was cleaned after each sample. Jaw crusher and mill were first blown with pressurised air and then wiped with paper towels damped in water and then acetone for drying. Pure quartzite rock was crushed and milled in between samples to further prevent any contamination.

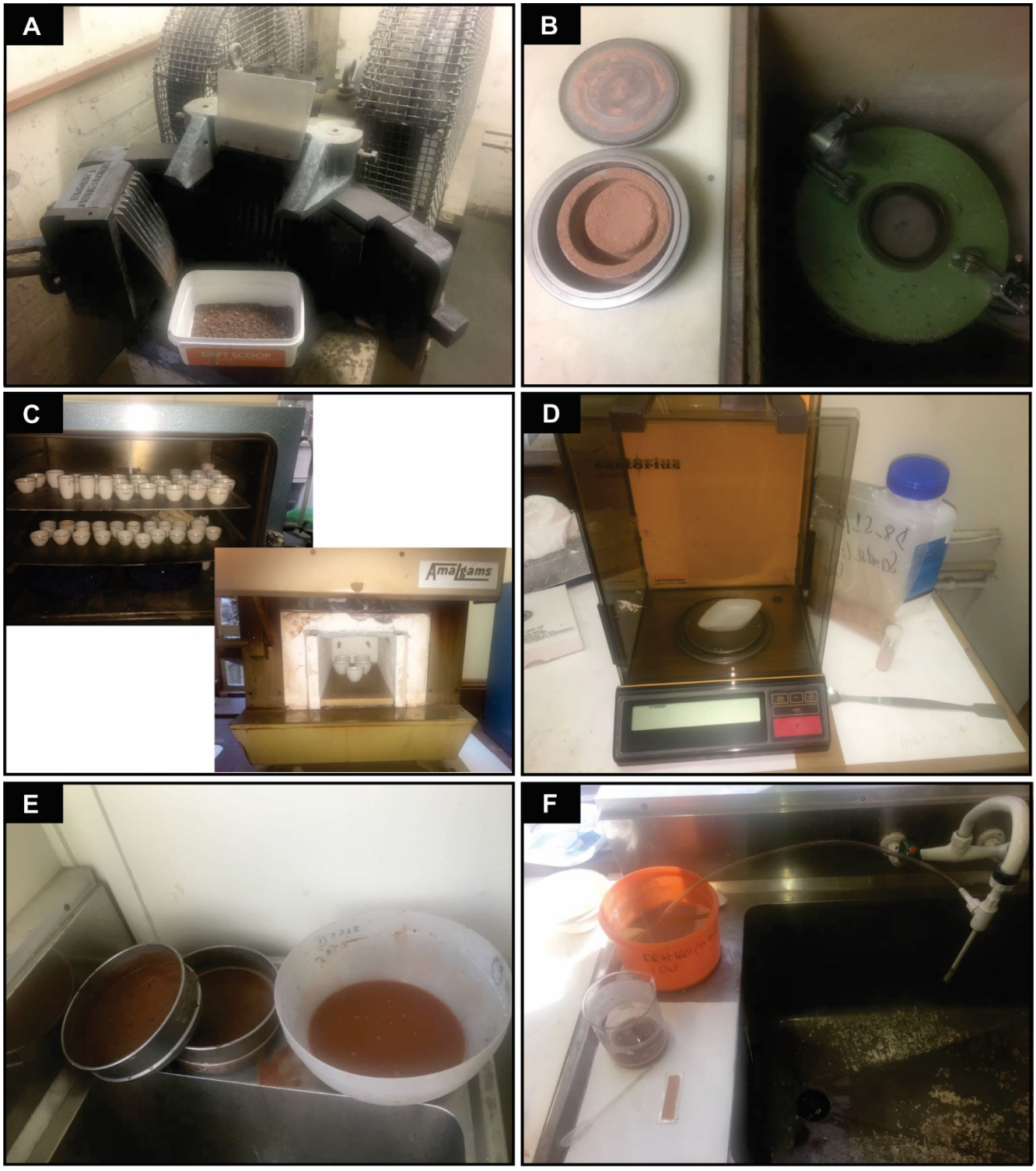

Figure 7. 1. Powder sample preparation process for geochemical analysis. A: jaw crusher, B: swing mill, C: 1000˚C dryer (top) and 10000˚C furnace (bottom), D: sample powder weighing apparatus, E: wet sieving for clay separation, F: collection of clay fraction onto glass slides for XRD analysis.

7.2. Site locations and site D6_S1

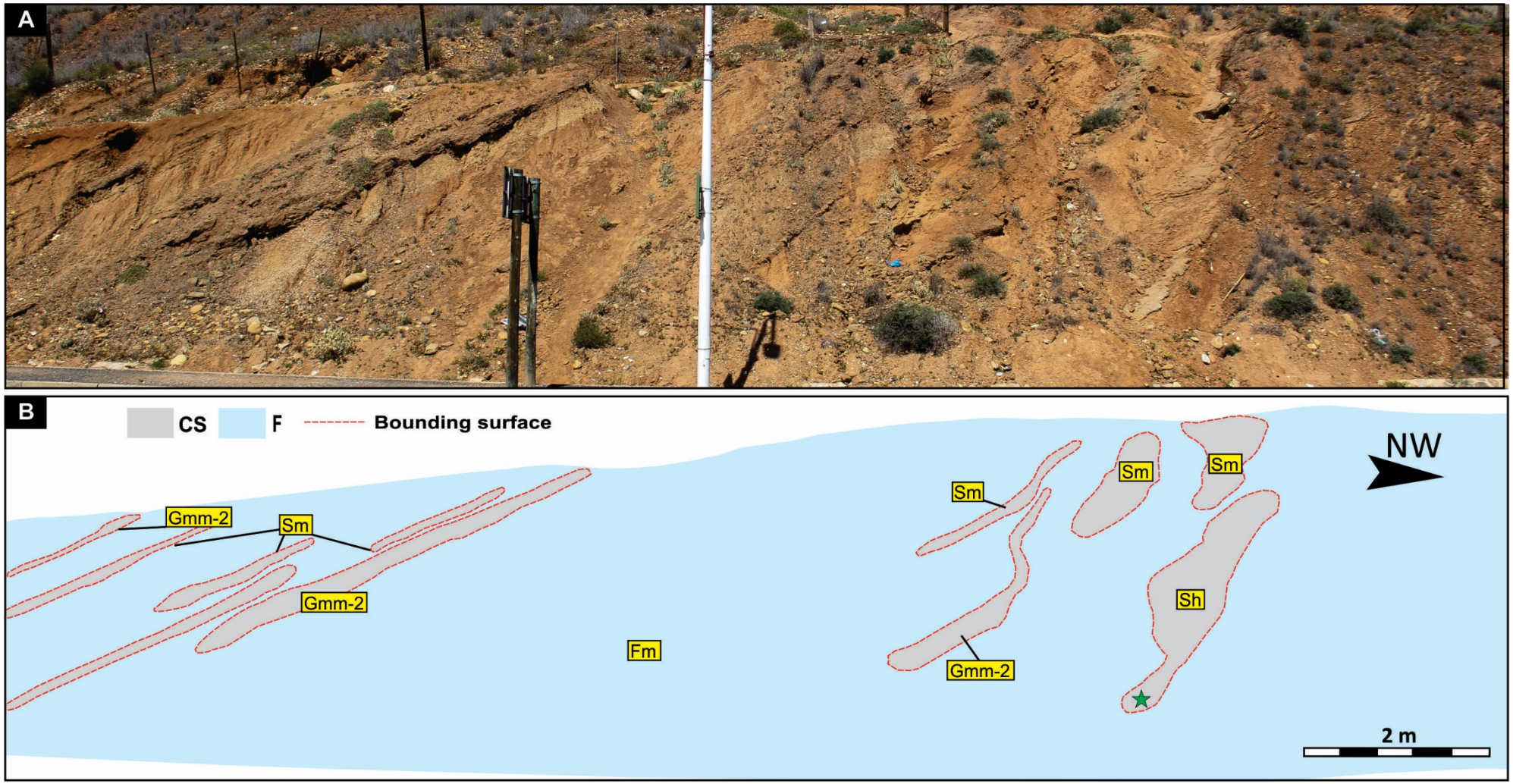

Figure 7.2. Elements F and CS at site D6_S1, dipping at 170/30 E. The geographical proximity (see Table 7.1 and Fig. 3.20) and the structural attitude of the strata suggest that these facies are stratigraphically below facies GS and site D5_S3 (Fig. 3.7). Green star indicates where burrows in Figure 3.3D were found. One bentonite horizon was noted 300 meters NW of this location, at siteD6_S2 (see map in Fig. 1.1B).

Table 7.1. Localities names (and corresponding numbers from map in Fig. 1.1B) and locations in decimal degrees and deg/min/secs.

Site Name	X	Y	Latitude	Longitude
D1_S1 (1)	-33.57794	22.20754	33°34'40.58"S	22°12'26.15"E
D1_S2 (2)	-33.53442	22.24481	33°32'3.91"S	22°14'41.32"E
D2_S1 (3)	-33.47819	22.24800	33°28'41.50"S	22°14'52.80"E
D2_S3 (4)	-33.46767	22.25584	33°28'3.63"S	22°15'21.01"E
D2_S5 (5)	-33.47831	22.34924	33°28'41.91"S	22°20'56.27"E
D2_S6 (6)	-33.48125	22.35703	33°28'52.50"S	22°21'25.30"E
D3_S2 (7)	-33.49864	21.99242	33°29'55.10"S	21°59'32.70"E
D3_S3 (8)	-33.50453	21.98758	33°30'16.30"S	21°59'15.30"E
D4_S1 (9)	-33.49647	22.01164	33°29'46.30"S	22° 0'41.90"E
D4_S3 (10)	-33.56950	22.05917	33°34'10.20"S	22° 3'33.00"E
D4_S4 (11)	-33.57686	22.05950	33°34'36.70"S	22° 3'34.20"E
D5_S1 (12)	-33.50247	21.87828	33°30'8.90"S	21°52'41.80"E
D5_S2 (13)	-33.51789	21.86339	33°31'4.40"S	21°51'48.20"E
D5_S3 (14)	-33.52850	21.68089	33°31'42.60"S	21°40'51.20"E
D5_S4 (15)	-33.51214	21.87019	33°30'43.70"S	21°52'12.70"E
D5_S5 (16)	-33.52025	21.85367	33°31'12.90"S	21°51'13.20"E
D6_S1 (17)	-33.52906	21.67997	33°31'44.60"S	21°40'46.90"E
D6_S2 (18)	-33.52822	21.67686	33°31'41.60"S	21°40'36.70"E
D6_S3 (19)	-33.50130	21.65500	33°30'4.69"S	21°39'18.00"E
D6_S4 (20)	-33.53939	21.68578	33°32'21.80"S	21°41'8.80"E
D7_S1 (21)	-33.62180	21.89472	33°37'18.50"S	21°53'41.30"E
D7_S2 (22)	-33.62003	21.87314	33°37'12.10"S	21°52'23.30"E
D7_S2.1 (23)	-33.61997	21.87393	33°37'11.90"S	21°52'26.16"E
D8_S1 (24)	-33.61911	21.86703	33°37'8.80"S	21°52'1.30"E
D8_S1.1 (25)	-33.61883	21.86703	33°37'6.80"S	21°52'1.30"E
D8_S7 (26)	-33.59486	22.02317	33°35'41.50"S	22° 1'23.40"E

Site Name	X	Y	Latitude	Longitude
D9_S1 (27)	-33.63078	22.21858	33°37'50.80"S	22°13'6.90"E
D9_S2 (28)	-33.63575	22.21894	33°38'8.70"S	22°13'8.20"E
D9_S3 (29)	-33.64392	22.22483	33°38'38.10"S	22°13'29.40"E
D9_S3.1 (30)	-33.64486	22.22483	33°38'41.50"S	22°13'29.40"E
D9_S4 (31)	-33.64889	22.22628	33°38'56.00"S	22°13'34.60"E
D9_S5 (32)	-33.64992	22.22694	33°38'59.70"S	22°13'36.00"E
D10_S1 (33)	-33.63242	22.21628	33°37'56.70"S	22°12'58.60"E
D10_S2 (34)	-33.63903	22.20911	33°38'20.50"S	22°12'32.80"E
D10_S3 (35)	-33.64061	22.20719	33°38'26.20"S	22°12'25.90"E
D10_S4 (36)	-33.64106	22.20672	33°38'26.80"S	22°12'24.20"E
D10_S5 (37)	-33.64156	22.20586	33°38'29.60"S	22°12'21.10"E
D11_S1 (38)	-33.64186	22.20481	33°38'30.70"S	22°12'16.30"E
D11_S2 (39)	-33.64189	22.20275	33°38'30.80"S	22°12'9.90"E
D11_S3 (40)	-33.64419	22.19856	33°38'39.10"S	22°11'54.80"E
D12_S1 (41)	-33.61925	22.40675	33°37'9.30"S	22°24'24.30"E
D12_S2 (42)	-33.6347	22.39917	33°38'4.90"S	22°23'56.30"E
D12_S3 (43)	-33.64258	22.37881	33°38'33.30"S	22°22'43.70"E
D12_S4 (44)	-33.62236	22.31103	33°37'20.50"S	22°18'39.70"E
D12_S6 (45)	-33.54278	22.46406	33°32'34.00"S	22°27'50.60"E
D12_S7 (46)	-33.55392	22.48761	33°33'14.10"S	22°29'15.40"E
D12_S8 (47)	-33.53828	22.45378	33°32'16.80"S	22°27'13.60"E
D13_S2 (48)	-33.57439,	22.20964	33°34'26.79"S	22°12'34.72"E
D17_S1 (49)	-33.63839	21.98547	33°38'18.20"S	21°59'6.70"E
D17_S1.1 (50)	-33.63886	21.98541	33°38'19.91"S	21°59'6.48"E
D17_S2 (51)	-33.63797	21.98431	33°38'16.70"S	21°59'3.50"E
D17_S2.1 (52)	-33.63769	21.98331	33°38'15.70"S	21°58'60.00"E
D23_S2 (53)	-33.57400	22.22417	33°34'26.40"S	22°13'26.00"E
D17_S2_Z (54)	-33.63889	21.98583	33°38'31.20"S	21°59'8.70"E
D23_S3 (55)	-33.57426	22.20852	33°34'26.34"S	22°12'30.68"E

7.3. Clast counts

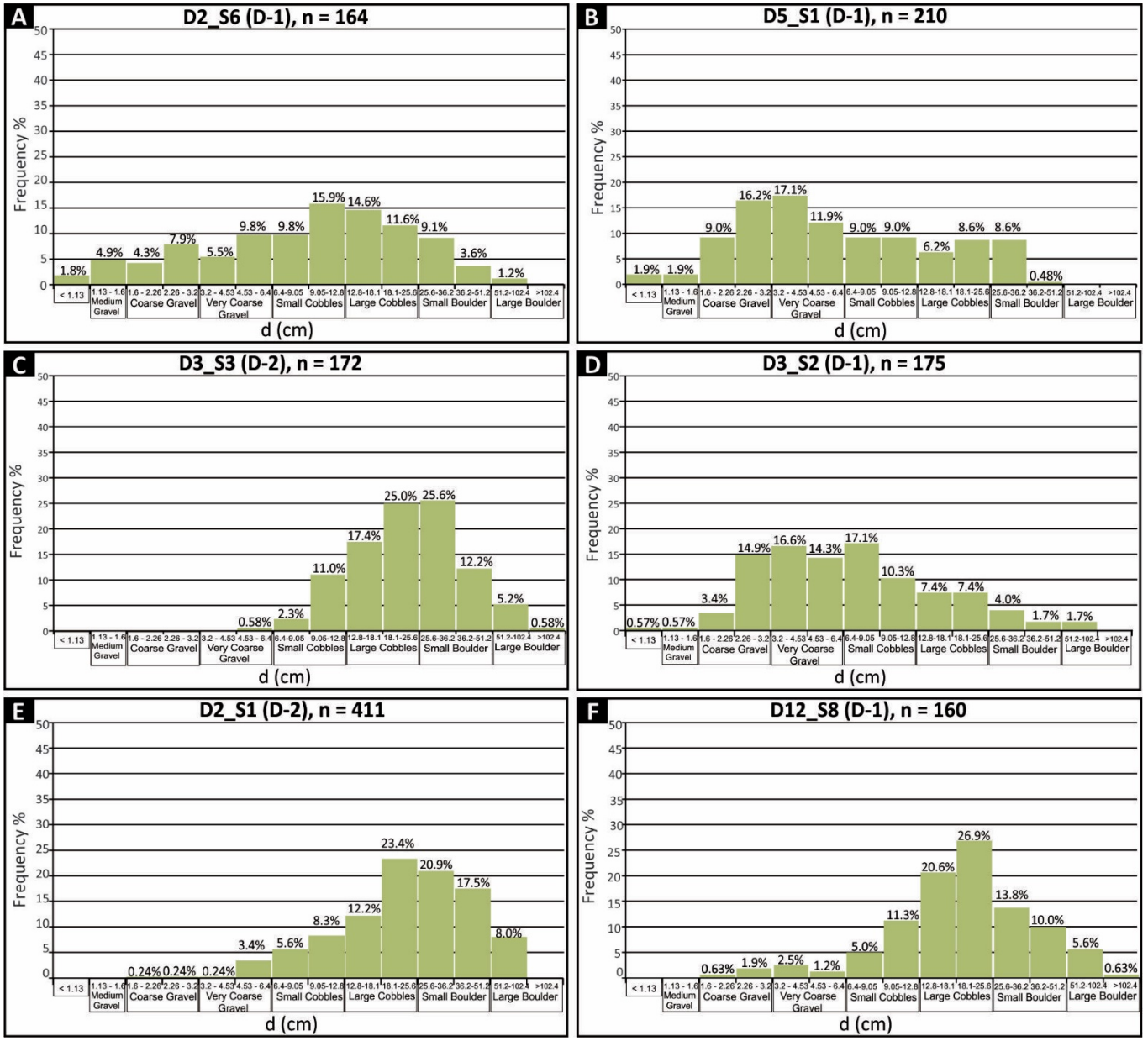

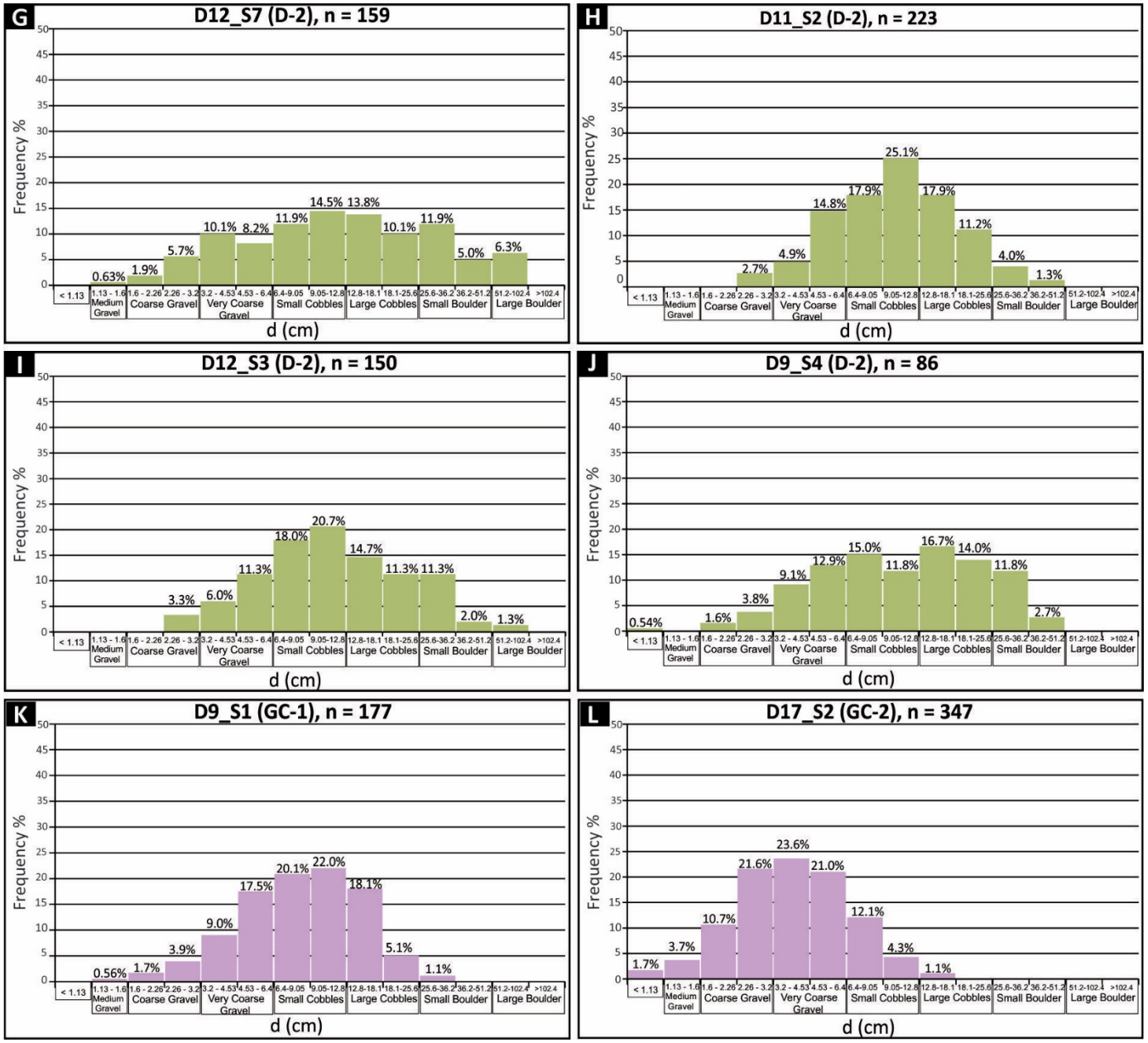
G
D12_S7 (D-2), n = 159
Frequency %
d (cm)
0.63%
1.9%
5.7%
10.1%
8.2%
11.9%
14.5%
13.8%
10.1%
11.9%
5.0%
6.3%
H
D11_S2 (D-2), n = 223
2.7%
4.9%
14.8%
17.9%
25.1%
17.9%
11.2%
4.0%
1.3%
I
D12_S3 (D-2), n = 150
3.3%
6.0%
11.3%
18.0%
20.7%
14.7%
11.3%
11.3%
2.0%
1.3%
J
D9_S4 (D-2), n = 86
0.54%
1.6%
3.8%
9.1%
12.9%
15.0%
11.8%
16.7%
14.0%
11.8%
2.7%
K
D9_S1 (GC-1), n = 177
0.56%
1.7%
3.9%
9.0%
17.5%
20.1%
22.0%
18.1%
5.1%
1.1%
L
D17_S2 (GC-2), n = 347
1.7%
3.7%
10.7%
21.6%
23.6%
21.0%
12.1%
4.3%
1.1%
< 1.13
1.13 - 1.6 Medium Gravel
1.6 - 2.26
2.26 - 3.2 Coarse Gravel
3.2 - 4.53
4.53 - 6.4 Very Coarse Gravel
6.4-9.05 Small Cobbles
9.05-12.8
12.8-18.1 Large Cobbles
18.1-25.6
25.6-36.2 Small Boulder
36.2-51.2
51.2-102.4 Large Boulder
>102.4

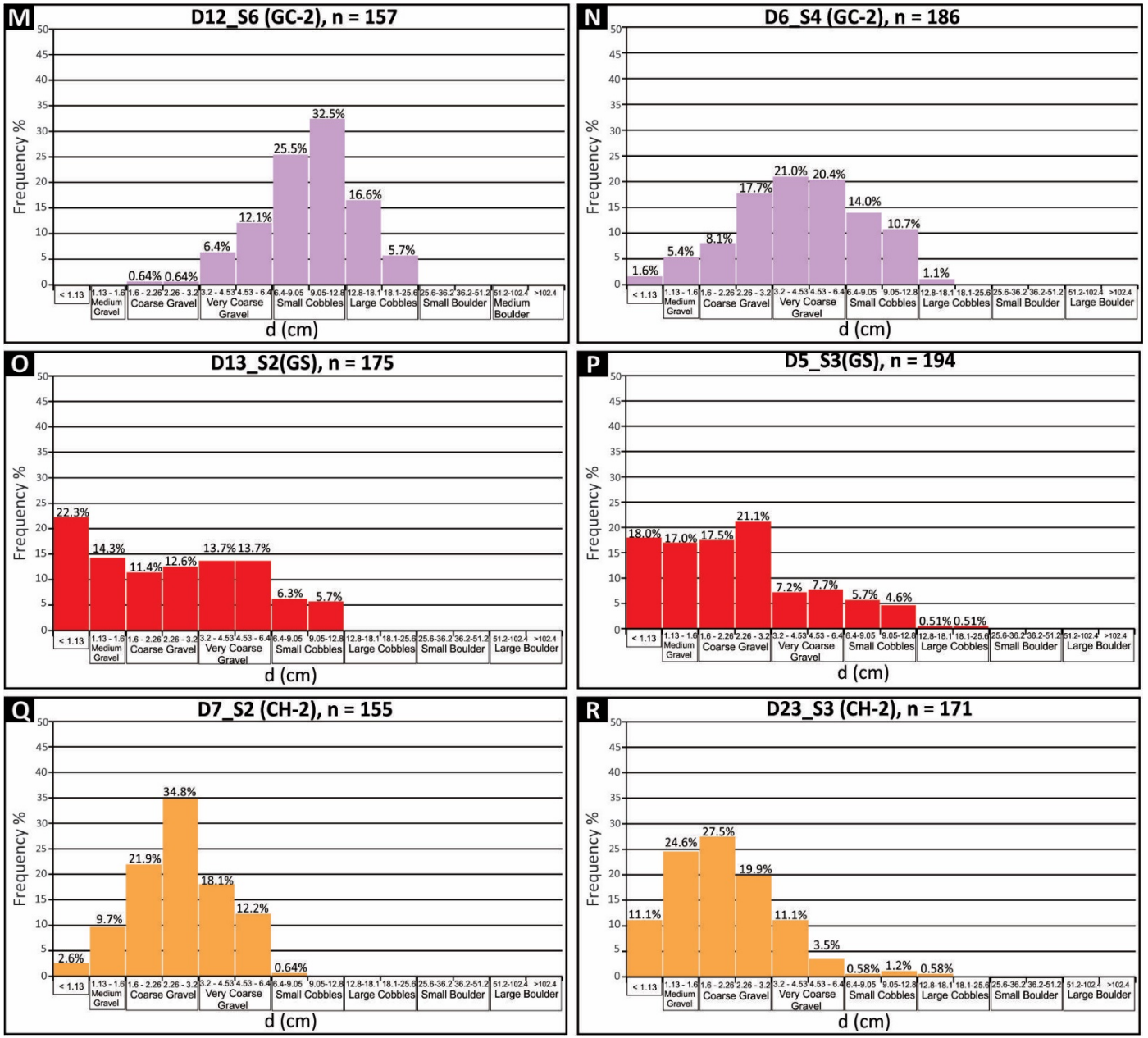

Figure 7.3. Distribution plots of percentage abundances of clast size in coarse-grained facies elements.

7.4. Petrography

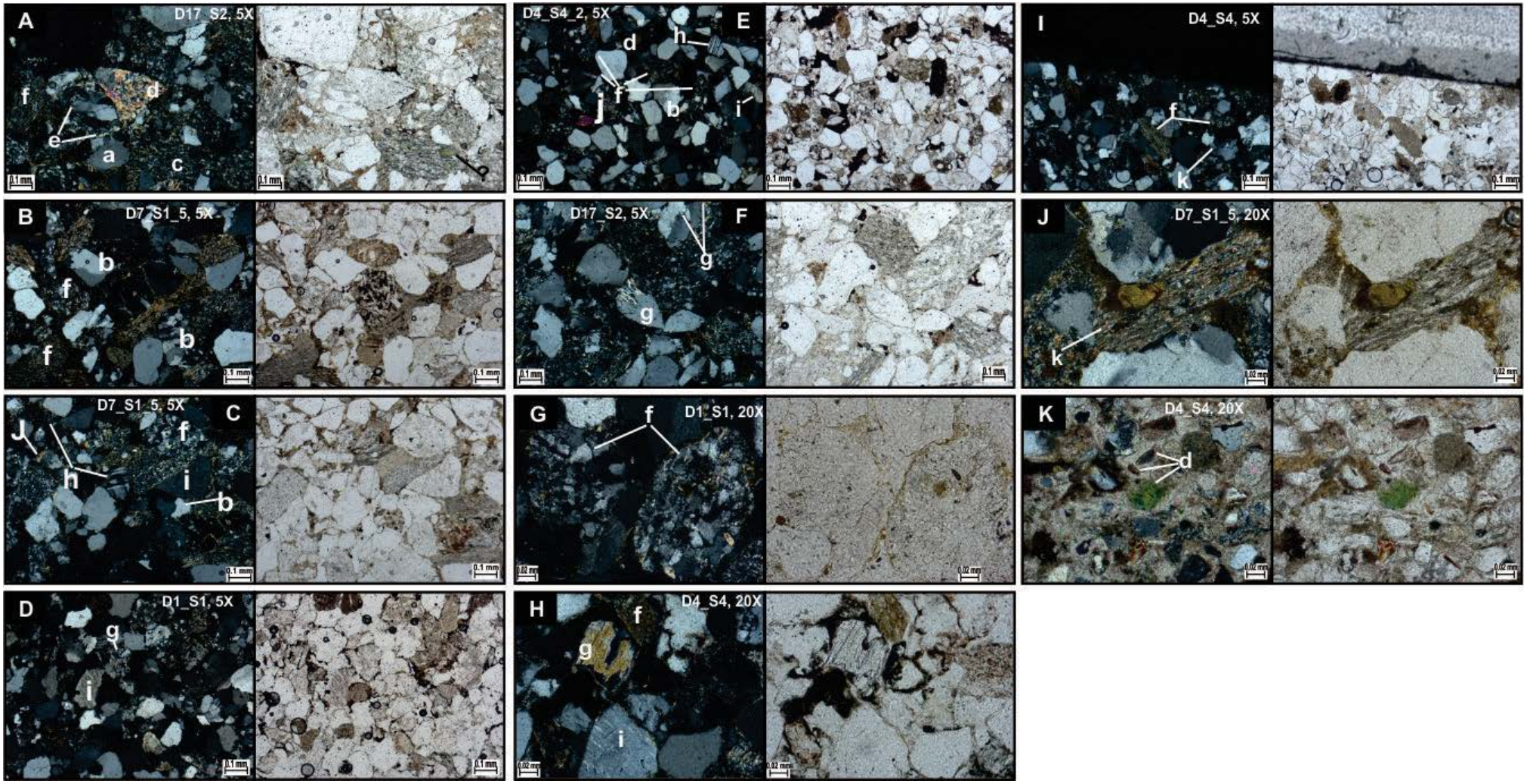

Figure 7.4. Thin section photomosaics of sandstones analysed for petrographic studies. Key: a – Qm; b – Qp; c – Lm; d – unidentified accessory mineral; e – clay cement; f – Ls; g – unidentified alteration; h – multiple twin microcline; i – alkali feldspar; j – mica; k – Lm.

Table 7.2. Classification of sandstones based on diagnostic features and modal compositions. Samples are coloured according to their locations in the basin: blue - centre; green - northwest; orange and grey: southwest; red: south.

Sample name and number		Sorting	Grain size range	Predominant rain size class	Gain:Matrix	Grain packing	Angularity	Sed Structures	Classification
D1_S1	1	Mod-Well	0,08-0,48mm, with one outlier exceeding 5mm (Lm)	Med-Coarse sand	97:3 %	Tightly	Mostly subangular	Massive	Med-coarse grained litharenite
D1_S2	2	Mod-Well	<0,08-0,32mm	Medium	95:5 %	Variable, mostly tightly	Mostly subangular	Massive	Medium-grained litharenite
D4_S3	3	Moderately	<0,08-0,24	Fine	95:5 %	Tightly	V-angular-subangular but mostly angular	Some lamination defined by dark brown bands	Fine-grained feldspathic litharenite
D4_S4	4	Poorly	<0,08-0,12	Very fine	60:40 %	Loosely	V-angular-subrounded, mostly angular	Massive, but extinction of groundmass alternates across bands/laminae	Very fine-grained carboneceous wacke
D4_S4	5	Poorly-moderate	0,16-0,56 mm, one occurrence of 1,6mm Ls	Med-coarse	98:2 %	Tightly	Angular-rounded, mostly subangular	Massive	Med-coarse grained feldspathic litharenite
D8_S7	11	Poorly	<0,08-2,16 mm	Medium	90:10 %	Tightly	Mostly subangular	Massive	Medium-grained feldspathic litharenite
D13_S2	16	Moderately	<0,08-0,24 mm	Fine	85:15 %	Loosely	Angular-subrounded	Massive	Fine-grained litharkosic wacke
D5_S3	6	Poorly	<0,08-0,16 mm, one Ls 1,28 mm	Mostly fine	70:30 %	Loosely	Mostly subangular	Massive	fine-grained wacke
D5_S5	7	Poorly	<0,08-0,4 mm	Mostly fine	90:10 %	Mostly tightly	mostly subangular	Massive, with coarse-grained minor laminae	Fine-grained lithic arkose
D7_S1	8	Moderately	0,08-1,04 mm	Coarse	90:10 %	Tightly	Mostly subangular and subrounded	Mostly massive, with some laminae	Coarse-grained litharenite
D7_S2	9	Moderately	<0,08-1,12 mm	Medium sand	90:10 %	Mostly tight	Mostly subangular	Laminae	Medium-grained litharenite
D8_S1	10	Moderately-well	<0,08-0,40 mm	Fine-medium	85:15 %	Difficult to establish, bust mostly loosely	Mostly angular	Massive	Medium-grained felspathic wacke
D9_S1	12	Poorly	0,08-0,96 mm	Medium-coarse	85:15 %	Loosely	Subangular and Subrounded	Massive	Medium-grained sublitharenite
D10_S1	13	Poorly	<0,08-0,56 mm, an outlier Ls 1,28 mm	Fine	80:20 %	Loosely	Subangular	Massive	Fine-grained litharkosic wacke
D10_S3	14	Poorly	<0,08-32 mm	Fine-medium	80:20 %	Variable; mostly loosely	Subangular-subrounded	Laminated, determined by grain size	Medium-grained quartzitic wacke
D11_S3	15	Poorly	0,08-0,56 mm	Fine-medium	75:25 %	Loosely	Angular-subrounded	Mostly massive, some laminae	Medium-grained quartzitic wacke
D17_S2	17	Poorly	0,08-1,12 mm	Medium-coarse	98:2 %	Tighty	Angular	Massive	Coarse-grained sublitharenite

Table 7.2B. Petrographic data from point counting of sandstones. A total of 300 grains were counted per sample. Percentages may not add to 100% due to rounding off.

Name, number	Qm	Qm%	Qp	Qp%	Qt	Qt%	Pk	Pk%	Ak	Ak%	Ft	Ft%	Lv	Lv%	Lm	Lm%	Lp	Lp%	Ls	Ls%	Acs	Acs %	Lt	Lt%	LT%
D1_S1U4, 1	87	29	43	14,3	130	43,3	7	2,3	26	8,7	33	11	1	0,3	3	1	0	0	45	15	88	29,3	137	45,7	45,7
D1_S2, 2	113	37,7	27	9	140	46,7	15	5	24	8	39	13	0	0	2	0,7	0	0	14	4,7	105	35	121	40,3	40,3
D4_S3, 3	118	39,3	48	16	166	55,3	13	4,3	32	10,7	45	15	0	0	0	0	0	0	1	0,3	88	29,3	89	29,7	29,7
D4_S4 U1, 4	143	47,7	2	0,8	145	48,3	12	4	43	14,3	55	18,3	0	0	28	9,3	0	0	12	4	60	20	100	33,3	33,3
D4_S4U4, 5	132	44	33	11	165	55	6	2	36	12	42	14	0	0	8	2,7	0	0	75	25	10	3,3	93	31	31
D8_S7LXP, 11	101	33,7	53	17,7	154	51,3	3	1	44	14,7	47	15,7	0	0	3	1	0	0	81	27	15	5	99	33	33
D13_S2, 16	160	53,3	33	11	193	64,3	18	6	43	14,3	61	20,3	0	0	16	5,3	0	0	2	0,7	28	9,3	46	15,3	15,3
Average %	**40,7**		**11,4**		**52**		**3,54**		**11,8**		**15,4**		**0,05**		**2,8**		**0**		**10,9**		**18,8**		**32,6**		
D5_S3, 6	140	46,7	43	14,3	183	61	4	1,3	15	5	19	6,3	0	0	22	7,3	0	0	30	10	46	15,3	98	32,7	32,7
D5_S5, 7	158	52,7	54	18	212	70,7	13	4,3	45	15	58	19,3	0	0	14	4,7	0	0	2	0,7	14	4,7	30	10	10
D7_S1, 8	105	35	63	21	168	56	0	0	13	4,3	13	4,3	0	0	2	0,7	0	0	102	34	15	5	119	39,7	39,7
D7_S2, 9	92	30,7	47	15,7	139	46,3	1	0,3	35	11,7	36	12	0	0	4	1,3	0	0	98	32,7	23	7,7	125	41,7	41,7
D8_S1U2, 10	128	42,7	38	12,7	166	55,3	19	6,3	39	13	58	19,3	0	0	6	2	0	0	51	17	19	6,3	76	25,3	25,3
Average %	**36,1**		**16,4**		**52,6**		**2,2**		**9,7**		**11,9**		**0**		**1,3**		**0**		**27,9**		**6,3**		**35,6**		
D9_S1B, 12	118	39,3	136	45,3	254	84,7	0	0	21	7	21	7	0	0	3	1	0	0	18	6	4	1,3	25	8,3	8,3
D10_S1, 13	160	53,3	62	20,7	222	74	2	0,7	49	16,4	51	17	0	0	4	1,37	0	0	6	2	17	5,7	27	9	9
D10_S3, 14	147	49	99	33	246	82	5	1,7	25	8,3	30	10	0	0	3	1	0	0	8	2,7	13	4,3	24	8	8
D11_S3, 15	122	40,7	130	43,3	252	84	9	3	17	5,7	26	8,7	0	0	2	0,7	0	0	6	2	14	4,7	22	7,3	7,3
Average %	**45,6**		**35,6**		**81,2**		**1,37**		**9,36**		**10,7**		**0**		**1**		**0**		**3,2**		**4**		**8,2**		
D17_S2, 17	86	28,7	141	47	227	75,7	2	0,7	10	3,3	12	4	0	0	6	2	0	0	52	17,3	3	1	61	20,3	20,3

7.4. Geochemistry

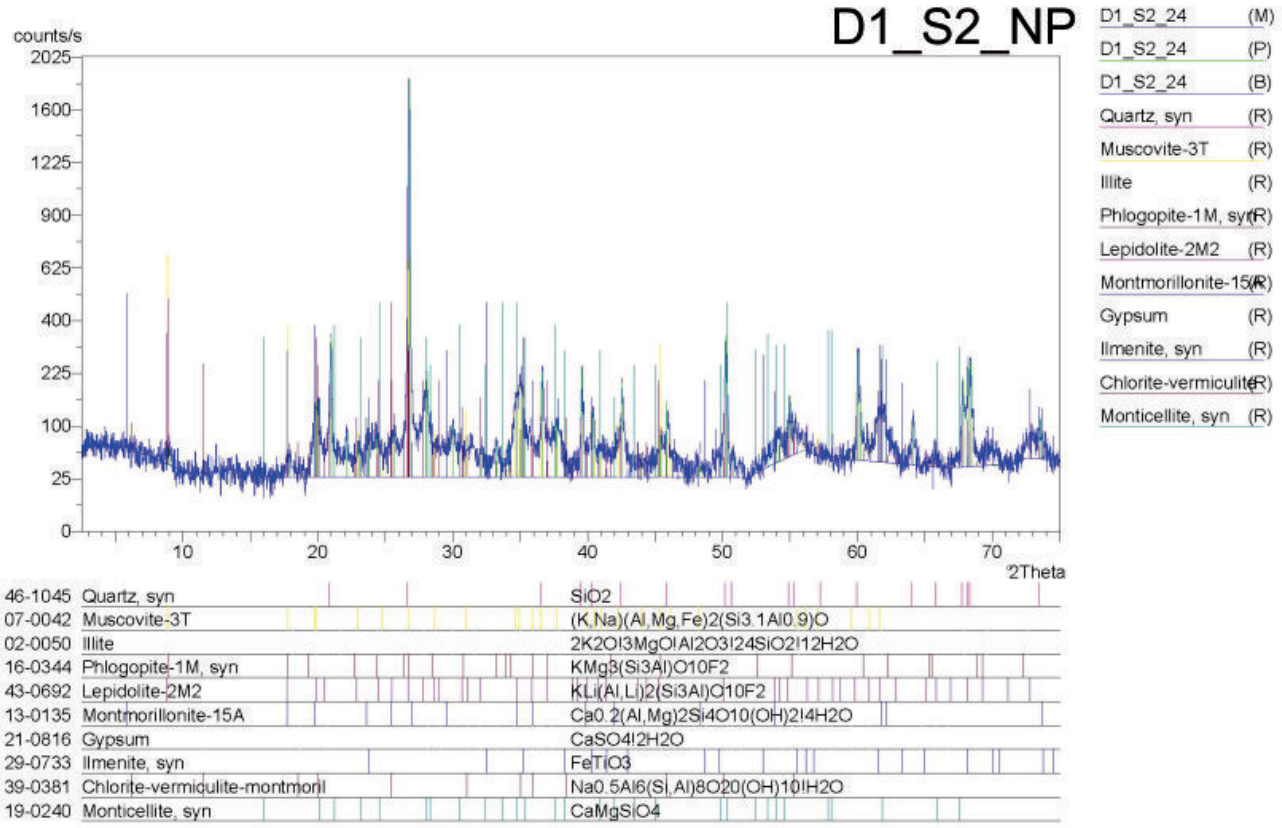

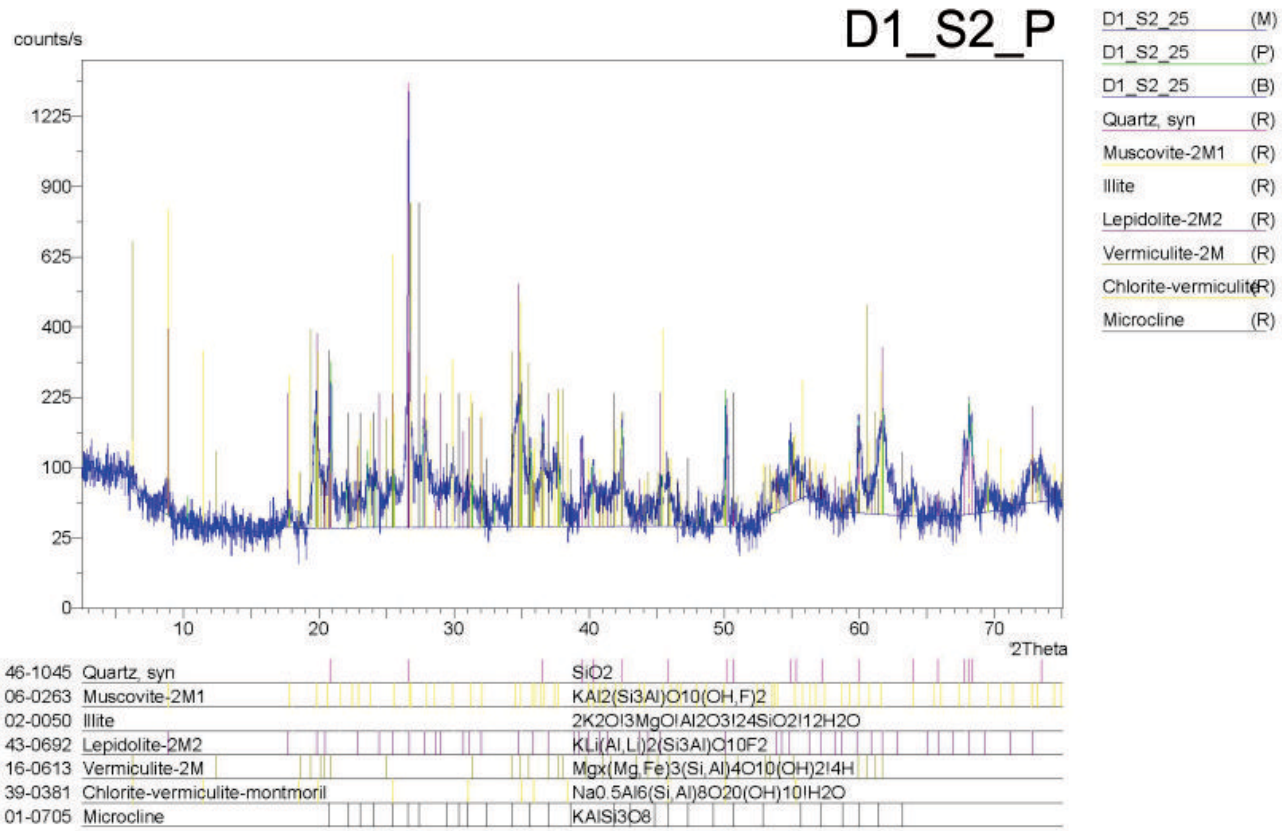

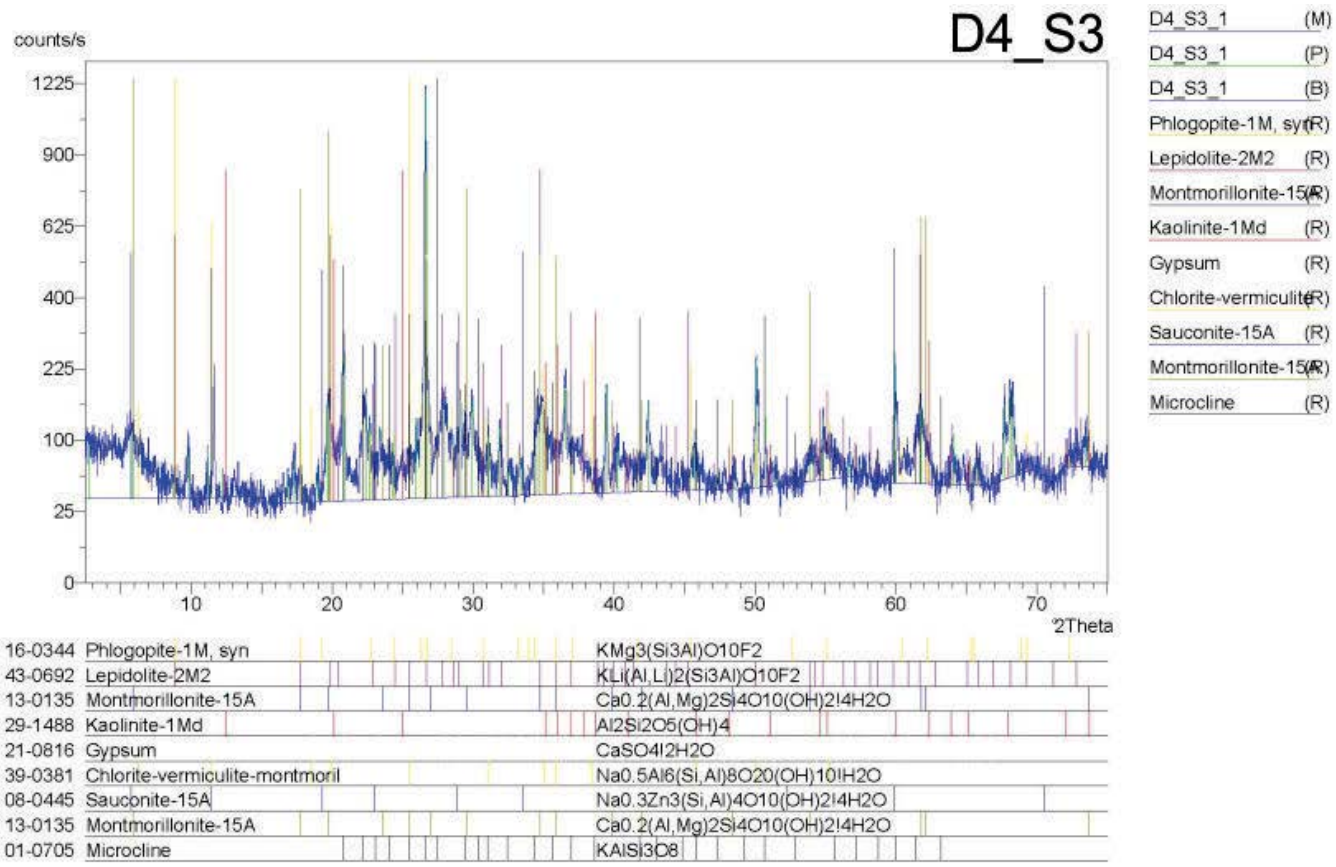
D4_S3
counts/s
1225
900
625
400
225
100
25
0
10
20
30
40
50
60
70
2Theta
D4_S3_1 (M)
D4_S3_1 (P)
D4_S3_1 (B)
Phlogopite-1M, syn (R)
Lepidolite-2M2 (R)
Montmorillonite-15A (R)
Kaolinite-1Md (R)
Gypsum (R)
Chlorite-vermiculite (R)
Sauconite-15A (R)
Montmorillonite-15A (R)
Microcline (R)
16-0344 Phlogopite-1M, syn KMg3(Si3Al)O10F2
43-0692 Lepidolite-2M2 KLi(Al,Li)2(Si3Al)O10F2
13-0135 Montmorillonite-15A Ca0.2(Al,Mg)2Si4O10(OH)2!4H2O
29-1488 Kaolinite-1Md Al2Si2O5(OH)4
21-0816 Gypsum CaSO4!2H2O
39-0381 Chlorite-vermiculite-montmoril Na0.5Al6(Si,Al)8O20(OH)10!H2O
08-0445 Sauconite-15A Na0.3Zn3(Si,Al)4O10(OH)2!4H2O
13-0135 Montmorillonite-15A Ca0.2(Al,Mg)2Si4O10(OH)2!4H2O
01-0705 Microcline KAlSi3O8

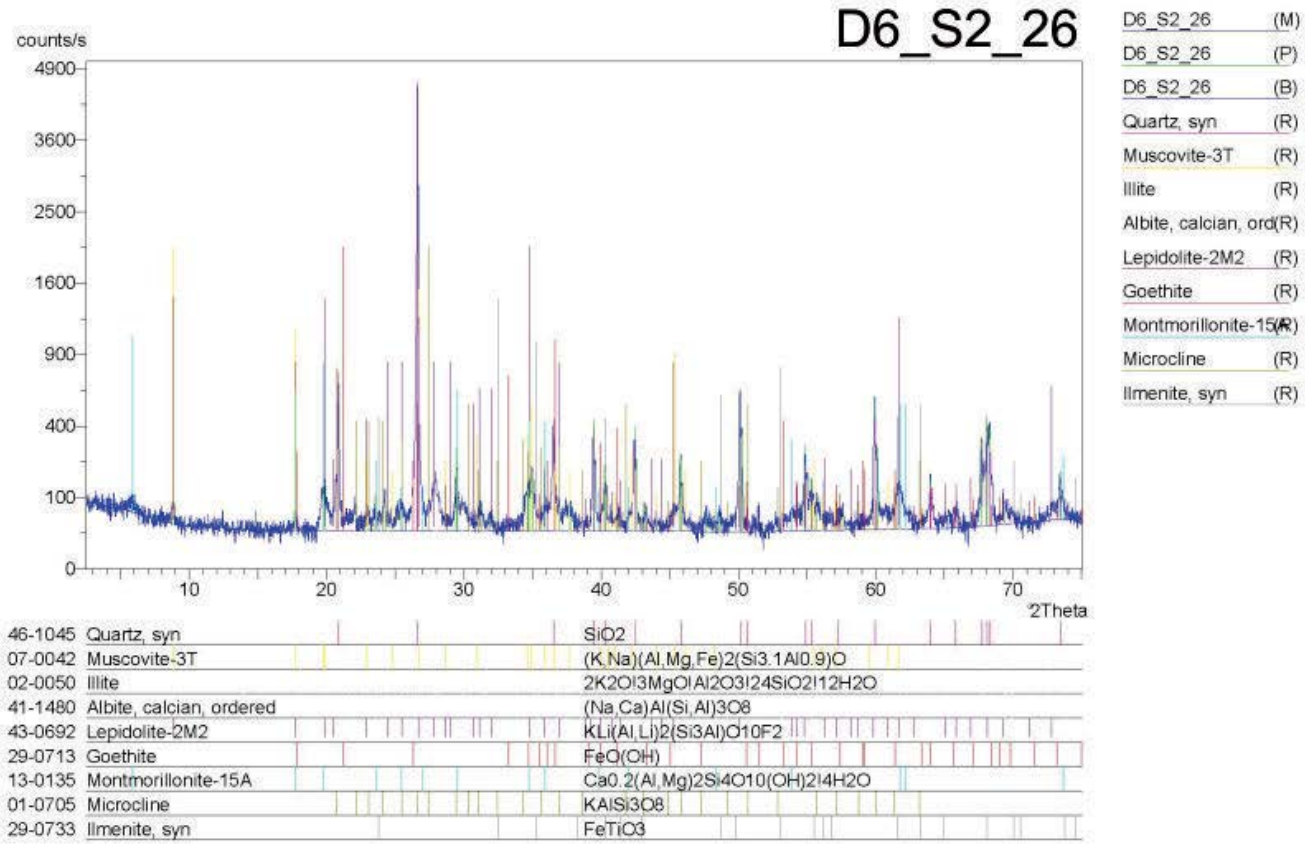
D6_S2_26
counts/s
4900
3600
2500
1600
900
400
100
0
10
20
30
40
50
60
70
2Theta
D6_S2_26 (M)
D6_S2_26 (P)
D6_S2_26 (B)
Quartz, syn (R)
Muscovite-3T (R)
Illite (R)
Albite, calcian, ord (R)
Lepidolite-2M2 (R)
Goethite (R)
Montmorillonite-15A (R)
Microcline (R)
Ilmenite, syn (R)
46-1045 Quartz, syn SiO2
07-0042 Muscovite-3T (K,Na)(Al,Mg,Fe)2(Si3.1Al0.9)O
02-0050 Illite 2K2O!3MgO!Al2O3!24SiO2!12H2O
41-1480 Albite, calcian, ordered (Na,Ca)Al(Si,Al)3O8
43-0692 Lepidolite-2M2 KLi(Al,Li)2(Si3Al)O10F2
29-0713 Goethite FeO(OH)
13-0135 Montmorillonite-15A Ca0.2(Al,Mg)2Si4O10(OH)2!4H2O
01-0705 Microcline KAlSi3O8
29-0733 Ilmenite, syn FeTiO3

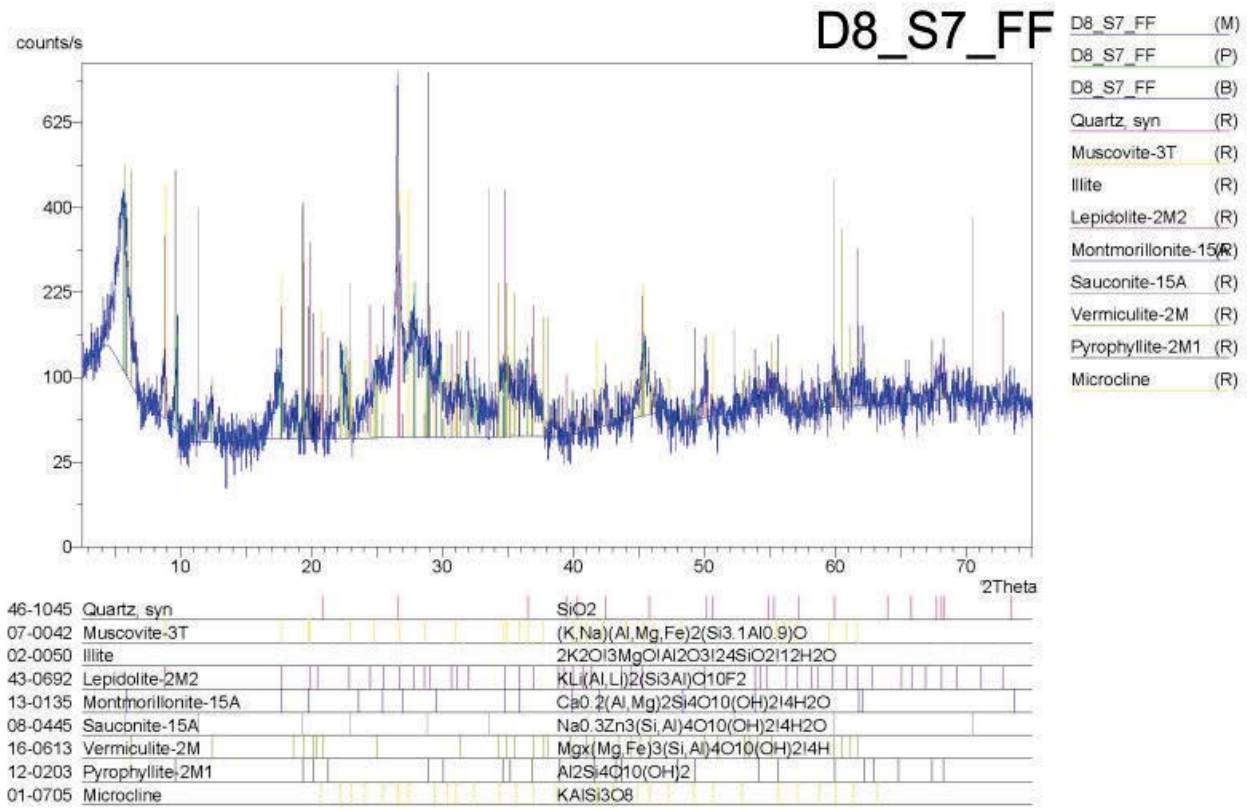
D8_S7_FF
counts/s
625
400
225
100
25
0
10
20
30
40
50
60
70
2Theta
D8_S7_FF (M)
D8_S7_FF (P)
D8_S7_FF (B)
Quartz, syn (R)
Muscovite-3T (R)
Illite (R)
Lepidolite-2M2 (R)
Montmorillonite-15A (R)
Sauconite-15A (R)
Vermiculite-2M (R)
Pyrophyllite-2M1 (R)
Microcline (R)
46-1045 Quartz, syn SiO2
07-0042 Muscovite-3T (K,Na)(Al,Mg,Fe)2(Si3.1Al0.9)O
02-0050 Illite 2K2O!3MgO!Al2O3!24SiO2!12H2O
43-0692 Lepidolite-2M2 KLi(Al,Li)2(Si3Al)O10F2
13-0135 Montmorillonite-15A Ca0.2(Al,Mg)2Si4O10(OH)2!4H2O
08-0445 Sauconite-15A Na0.3Zn3(Si,Al)4O10(OH)2!4H2O
16-0613 Vermiculite-2M Mgx(Mg,Fe)3(Si,Al)4O10(OH)2!4H
12-0203 Pyrophyllite-2M1 Al2Si4O10(OH)2
01-0705 Microcline KAlSi3O8

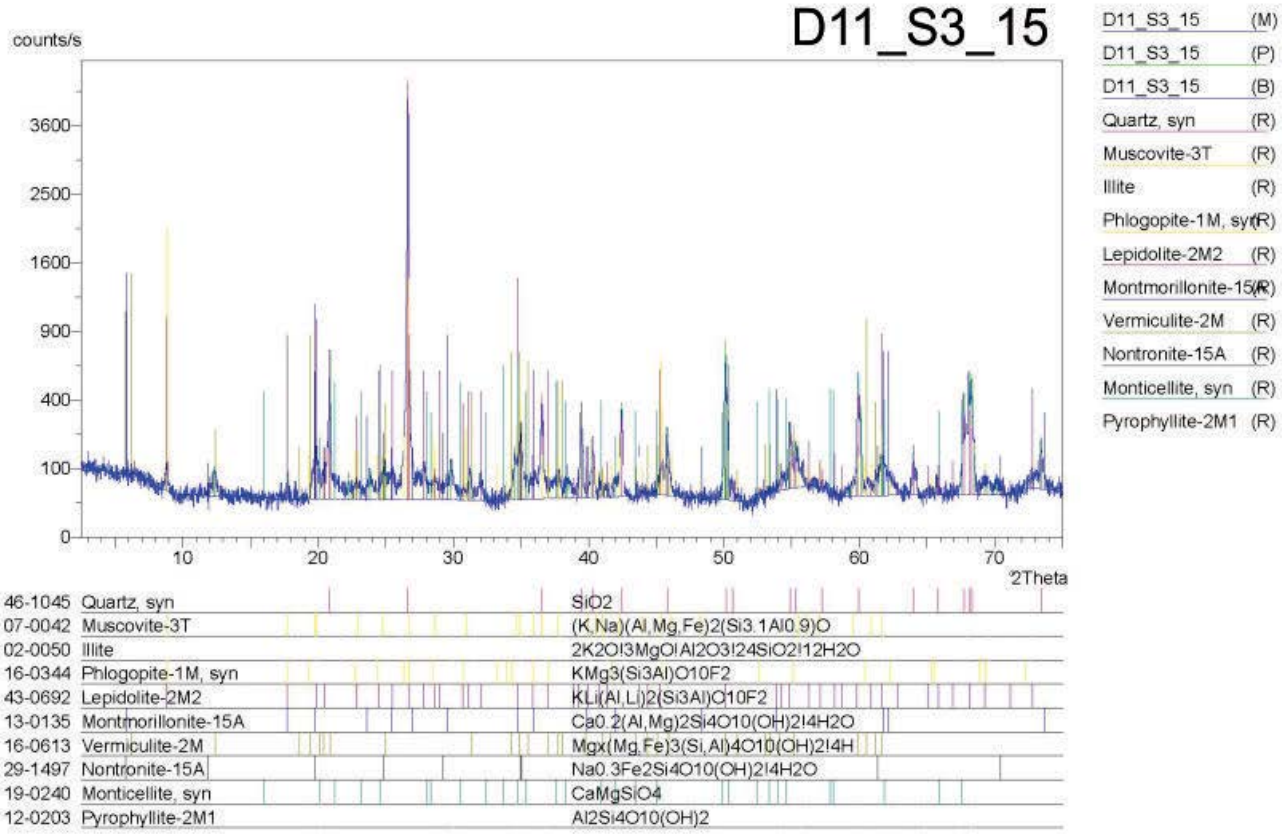
D11_S3_15
counts/s
3600
2500
1600
900
400
100
0
10
20
30
40
50
60
70
2Theta
D11_S3_15 (M)
D11_S3_15 (P)
D11_S3_15 (B)
Quartz, syn (R)
Muscovite-3T (R)
Illite (R)
Phlogopite-1M, syn (R)
Lepidolite-2M2 (R)
Montmorillonite-15A (R)
Vermiculite-2M (R)
Nontronite-15A (R)
Monticellite, syn (R)
Pyrophyllite-2M1 (R)
46-1045 Quartz, syn SiO2
07-0042 Muscovite-3T (K,Na)(Al,Mg,Fe)2(Si3.1Al0.9)O
02-0050 Illite 2K2O!3MgO!Al2O3!24SiO2!12H2O
16-0344 Phlogopite-1M, syn KMg3(Si3Al)O10F2
43-0692 Lepidolite-2M2 KLi(Al,Li)2(Si3Al)O10F2
13-0135 Montmorillonite-15A Ca0.2(Al,Mg)2Si4O10(OH)2!4H2O
16-0613 Vermiculite-2M Mgx(Mg,Fe)3(Si,Al)4O10(OH)2!4H
29-1497 Nontronite-15A Na0.3Fe2Si4O10(OH)2!4H2O
19-0240 Monticellite, syn CaMgSiO4
12-0203 Pyrophyllite-2M1 Al2Si4O10(OH)2

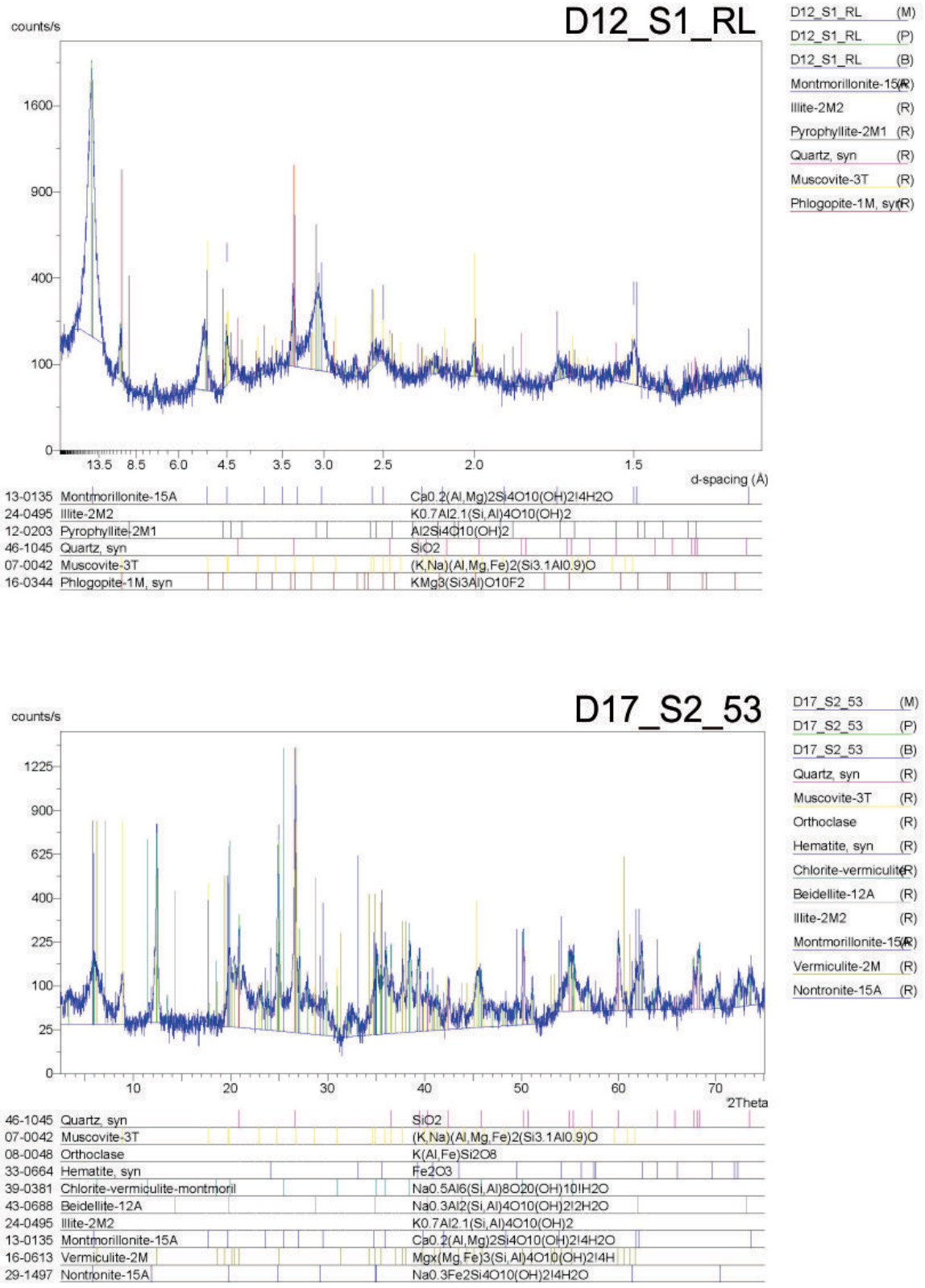

Figure 7.5. XRD spectra for F-lithofacies and clay fractions of very fine-grained S-lithofacies. Analysis carried out using a Philips PW 1390 XRD machine in the Dept. Geol. Sci. at UCT. Machine specs: Cu K-α X-Ray tube (wavelength of 1.541 A), accelerating voltage= 40 kV, current=25mA.

Table 7.3. Major oxide weight percentages of 38 sandstone and mudstone samples in the study area. Calculations with "*" exclude outliers 7, 13 and 22 which show very high of wt% CaO. F-Av/StDev: mudstones average/standard deviation; S-Av/StDev: sandstones average/standard deviation.

Site name and sample number		SiO_2	TiO_2	Al_2O_3	Fe_2O_3	MnO	MgO	CaO	Na_2O	K_2O	P_2O_5	SO_3	Cr_2O_3	NiO	H_2O-	LOI	Total	Facies code	Location and Arch. element
D17_S2	1	53,2	0,5	23,9	4,0	0,03	1,3	0,5	1,0	1,5	0,14	0,1	b.d.	0,007	2,4	10,5	99,0	Fl	Southwest, CH-1
D4_S3	2	79,3	0,5	8,8	3,1	0,04	0,7	0,6	1,7	1,8	0,08	b.d.	0,006	0,008	0,5	2,6	99,9	Fm	Centre,F
D8_S7	3	67,5	0,6	12,7	4,4	0,11	1,5	1,1	2,2	2,2	0,08	0,0	b.d.	0,007	1,6	5,3	99,2	Fm	Centre, F
D1_S2	4	58,9	0,6	16,5	6,2	0,08	2,0	0,6	1,5	3,8	0,14	b.d.	0,006	0,009	3,1	5,6	99,1	Fm	Center, F
D7_S2	5	53,5	0,3	17,5	3,4	0,09	3,4	0,3	3,0	0,8	0,05	0,6	b.d.	0,007	10,0	6,9	99,8	Fm	Southwest, F
D7_S2	6	66,4	0,6	13,8	3,9	0,05	1,6	0,5	1,9	3,0	0,10	b.d.	0,006	0,009	2,7	4,1	98,7	Fm	Southwest, F
D4_S3	7	56,0	0,2	14,6	2,7	0,11	1,9	2,6	2,6	1,1	0,04	0,9	b.d.	0,008	5,5	10,5	98,9	Fm (Fl)	Centre, F
D1_S2	8	55,9	0,6	17,5	6,4	0,10	2,3	1,0	1,1	4,0	0,13	0,0	0,007	0,016	3,7	7,2	99,8	Fp	Centre, F
D11_S3	9	73,4	0,6	12,1	2,4	0,01	0,7	0,1	0,6	2,3	0,03	b.d.	0,006	0,008	2,3	4,6	99,2	Sf	South, CH-2
D13_S2	10	77,6	0,6	9,8	2,6	0,05	0,7	0,5	1,4	2,0	0,09	b.d.	0,006	0,008	1,5	2,8	99,6	Sf	Centre, CH-2
D10_S3	11	81,1	0,7	10,5	0,9	0,01	0,3	0,1	0,3	1,8	0,03	0,0	b.d.	0,008	0,3	3,4	99,3	Sh	South, CH-2
D1_S1	12	88,3	0,3	5,0	1,9	0,02	0,4	0,2	0,7	1,0	0,10	0,0	b.d.	0,007	0,3	1,5	99,7	Shc	Centre, CH-2
D4_S4	13	54,5	0,4	8,5	2,5	0,16	1,0	14,1	1,7	1,8	0,07	0,0	b.d.	0,007	1,1	13,7	99,6	Sh	Centre, CH-2
D4_S3	14	76,7	0,5	8,7	2,4	0,04	0,8	0,9	1,8	1,8	0,06	0,0	b.d.	0,008	1,3	4,0	99,1	Sm	Centre, CS
D5_S3	15	80,0	0,6	8,3	3,6	0,04	0,7	0,2	0,4	1,8	0,09	b.d.	b.d.	0,008	0,4	2,8	99,1	Sm	Northeast, GS
D7_S1	16	84,6	0,3	5,9	2,4	0,03	0,6	0,2	0,9	1,2	0,04	b.d.	b.d.	0,007	0,7	2,1	99,1	Sm	Southwest, CH-2
D10_S3	17	86,7	0,7	7,2	0,4	0,01	0,2	0,0	0,4	1,2	0,01	b.d.	b.d.	0,006	0,1	2,4	99,3	Sm	South, CH-2
D11_S3	18	78,0	0,7	10,5	2,1	0,01	0,6	0,0	0,5	2,4	0,02	0,0	0,008	0,011	1,5	3,4	99,7	Sm	South, CS
D1_S2	19	81,8	0,5	8,1	2,1	0,11	0,6	0,5	1,7	1,5	0,06	b.d.	b.d.	0,008	0,5	2,0	99,6	Sm	Centre, CS
D9_S1	20	85,1	0,5	8,1	1,6	0,01	0,2	0,0	0,2	1,6	0,02	b.d.	b.d.	0,007	0,1	2,0	99,5	Sm	South, GS
D9_S1	21	82,1	0,8	10,7	1,4	0,01	0,2	0,0	0,2	1,8	0,01	b.d.	0,006	0,007	0,3	3,0	100,5	Sm	South, GS
D6_S2	22	66,6	0,7	12,5	3,9	0,04	1,3	2,9	1,1	2,4	0,06	0,1	0,006	0,008	1,6	6,1	99,3	Sm	Northeast, CS
D7_S2	23	83,4	0,4	6,3	2,2	0,03	0,7	0,6	1,0	1,4	0,06	0,0	0,006	0,008	1,2	2,2	99,5	Sm	Southwest, CH-2
D8_S1	24	73,6	0,6	10,9	2,9	0,04	1,1	0,4	2,0	2,2	0,08	0,1	b.d.	0,008	2,1	3,5	99,7	Sm	Southwest, CH-2
D8_S1.1	25	73,3	0,9	13,7	2,5	0,01	0,6	0,1	0,4	2,4	0,02	b.d.	b.d.	0,008	0,7	4,2	98,9	Sm	Southwest, CS
D17_S2	26	82,8	0,8	8,6	2,2	0,03	0,7	0,1	0,5	1,9	0,03	b.d.	b.d.	0,007	0,2	1,7	99,6	Sm	Southwest, GB
D17_S2	27	81,0	0,5	9,7	2,8	0,03	0,7	0,0	0,6	2,1	0,02	b.d.	b.d.	0,008	0,3	1,5	99,3	Sm	Southwest, GB
D17_S2	28	69,5	0,7	12,3	3,6	0,04	1,1	1,3	0,8	2,6	0,03	0,0	b.d.	0,007	1,6	5,7	99,1	Sm, Sf	Southwest, GC-3

Site name and sample number		SiO_2	TiO_2	Al_2O_3	Fe_2O_3	MnO	MgO	CaO	Na_2O	K_2O	P_2O_5	SO_3	Cr_2O_3	NiO	H_2O-	LOI	Total	Facies code	Location and Arch. element
D5_S3	29	74,7	0,7	10,7	4,2	0,05	0,9	0,3	0,5	2,1	0,12	b.d.	b.d.	0,008	0,8	3,8	99,0	Sm, Smc	Northeast, GS
D8_S1	30	68,9	0,7	13,3	6,7	0,07	1,4	0,3	1,2	2,8	0,18	b.d.	0,006	0,010	0,6	3,2	99,4	Sm, Sh, Shc	Southwest, CH-2
D10_S1	31	78,7	0,8	11,9	0,6	0,01	0,4	0,1	0,3	2,0	0,03	b.d.	0,006	0,007	0,4	4,0	99,2	Sm, Sh, Shc	South, GS
D10_S1	32	81,2	0,7	8,2	3,0	0,01	0,7	0,2	0,2	1,6	0,03	b.d.	0,006	0,008	0,5	3,0	99,3	Sm, Sh, Shc	South, GS
D12_S1	33	81,0	0,6	9,8	1,8	0,01	0,6	0,0	0,3	1,8	0,02	b.d.	b.d.	0,007	0,5	3,0	99,3	Sm, Sh, Shc	South, GB
D12_S1	34	79,0	0,6	10,3	3,3	0,01	0,4	0,0	0,2	2,1	0,03	b.d.	0,006	0,008	0,3	3,0	99,2	Sm, Sh, Shc	South, GB
D4_S4	35	83,7	0,5	6,3	2,5	0,05	0,6	0,7	1,3	1,2	0,08	b.d.	0,006	0,007	0,5	2,0	99,7	Sm, Sh, Shc	Centre, CH-2
D4_S4	36	85,6	0,4	5,8	2,1	0,04	0,5	0,6	1,1	1,2	0,07	b.d.	0,007	0,008	0,3	1,8	99,5	Sm, Sh, Shc	Centre, CH-2
D8_S1.1	37	75,9	0,8	12,2	3,0	0,01	0,6	0,0	0,3	2,3	0,01	b.d.	0,006	0,008	0,6	3,7	99,7	Sm, Sh bottom	Southwest, CS
D8_S7	38	84,2	0,3	6,1	1,6	0,04	0,6	0,9	1,1	1,0	0,07	0,2	0,006	0,008	0,3	2,8	99,3	Smc	Centre, CH-2
Average		74,8	0,6	10,7	2,9	0,04	0,9	0,9	1,0	1,9	0,1	0,1	0,006	0,008	1,4	4.1	99,4		
StDev		10,22	0,16	3,87	1,41	0,04	0,65	2.9	0,73	0,69	0,04	0,25	0,001	0,002	1,84	2,68	0,34		
Average*		76,2	0,6	10,6	2,9	0,04	0,9	0,4	1,0	1,9	0,1	0,1	0,06	0,008	1,3	3,6	99,4		
StDev*		9,34	0,15	3,95	1,46	0,03	0,65	0,35	0,70	0,71	0,04	0,16	0,001	0,002	1,78	1,87	0,34		
F-Av		62.1	0,5	15,8	4,5	0,1	1,8	0,7	1,8	2,4	0,1	0,2	0,006	0,009	3,4	6,0	99,4		
F-StDev		9,34	0,13	4,73	1,29	0,03	0,84	0,26	0,68	1,2	0,03	0,26	0,001	0,003	3.1	2,53	0,46		
S- Av		79,7	0,6	9,3	2,5	0,03	0,6	0,3	0,7	1,8	0,1	0,1	0,006	0,008	0,7	3,0	99,4		
S-StDev		5,03	0,16	2,42	1,21	0,02	0,27	0,34	0,53	0,49	0,04	0,07	0,001	0,001	0,60	1,0	0,32		

Table 7.3. Major element ratios and weathering/palaeoclimate indexes used in this study. Calculations with "*" exclude outliers 7, 13 and 22 which show very high of wt% CaO.

Site name and sample number		K_2O/Na_2O	SiO_2/Al_2O_3	CIA	CIAmol	ICV	Facies code	Location and Arch. element
D17_S2	1	1,54	2,22	88,7	5,62	0,37	Fl	SW, CH-1
D4_S3	2	1,08	9,03	67,9	1,48	0,98	Fm	Centre,F
D8_S7	3	1,00	5,30	70,2	1,63	0,95	Fm	Centre, F
D1_S2	4	2,44	3,56	73,5	2,12	0,89	Fm	Center, F
D7_S2	5	0,256	3,05	81,0	2,75	0,64	Fm	SW, F
D7_S2	6	1,52	4,80	72,0	1,91	0,83	Fm	SW, F
D4_S3	7	0,44	3,83	69,9	1,44	0,77	Fm (Fl)	Centre, F
D1_S2	8	3,53	3,20	74,2	2,21	0,88	Fp	Centre, F
D11_S3	9	4,15	6,08	80,6	3,43	0,56	Sf	South, CH-2
D13_S2	10	1,43	7,93	71,4	1,81	0,80	Sf	Centre, CH-2
D10_S3	11	6,71	7,72	83,0	4,15	0,38	Sh	South, CH-2
D1_S1	12	1,39	17,6	72,5	1,93	0,91	Shc	Centre, CH-2
D4_S4	13	1,06	6,38	32,6	0,280	2,54	Sh	Centre, CH-2
D4_S3	14	1,05	8,84	65,7	1,32	0,95	Sm	Centre, CS
D5_S3	15	4,61	9,58	77,8	2,81	0,88	Sm	NE, GS
D7_S1	16	1,31	14,2	72,0	1,87	0,96	Sm	SW, CH-2
D10_S3	17	3,55	12,1	81,8	3,73	0,40	Sm	South, CH-2
D11_S3	18	5,25	7,43	78,3	3,07	0,60	Sm	South, CS
D1_S2	19	0,863	10,1	68,0	1,47	0,88	Sm	Centre, CS
D9_S1	20	8,36	10,4	82,3	4,08	0,51	Sm	South, GS
D9_S1	21	8,99	7,68	84,1	4,62	0,41	Sm	South, GS
D6_S2	22	2,16	5,34	65,9	1,28	0,99	Sm	Northeast, CS
D7_S2	23	1,33	13,2	67,8	1,48	1,00	Sm	SW, CH-2
D8_S1	24	1,11	6,72	70,0	1,67	0,86	Sm	SW, CH-2
D8_S1.1	25	6,12	5,34	82,6	4,00	0,50	Sm	SW, CS
D17_S2	26	3,95	9,59	77,9	2,89	0,72	Sm	SW, GB
D17_S2	27	3,47	8,38	78,1	2,94	0,71	Sm	SW, GB
D17_S2	28	3,26	5,66	72,7	1,93	0,82	Sm, Sf	SW, GC-3
D5_S3	29	3,99	6,96	78,2	2,84	0,82	Sm, Smc	NE, GS
D8_S1	30	2,23	5,17	75,9	2,43	0,99	Sm, Sh, Shc	SW, CH-2
D10_S1	31	7,14	6,63	83,3	4,24	0,35	Sm, Sh, Shc	South, GS
D10_S1	32	6,36	9,91	80,4	3,38	0,77	Sm, Sh, Shc	South, GS
D12_S1	33	5,93	8,28	82,4	4,01	0,52	Sm, Sh, Shc	South, GB
D12_S1	34	10,4	7,70	81,3	3,81	0,65	Sm, Sh, Shc	South, GB
D4_S4	35	0,949	13,3	66,0	1,32	1,11	Sm, Sh, Shc	Centre, CH-2
D4_S4	36	1,07	14,7	66,8	1,38	1,01	Sm, Sh, Shc	Centre, CH-2
D8_S1.1	37	6,55	6,2	82,1	3,91	0,59	Sm, Sh bottom	SW, CS
D8_S7	38	0,877	13,8	67,0	1,35	0,91	Smc	Centre, CH-2
Average		3,35	8,10	74,4	2,59	0,800		
StDev		2,65	3,55	9,29	1,19	0,354		
Average*		3,54	8,35	75,9	2,73	0,746		
StDev*		2,67	3,58	6,23	1,13	0,214		
Fine-Av*		1,62	4,45	75,4	2,53	0,792		
Fine-StDev*		0,991	2,10	6,62	1,32	0,200		
Coarse- Av*		4,01	9,32	76,1	2,78	0,734		
Coarse-StDev*		2,74	3,18	6,12	1,07	0,216		

Table 7.4. Qualitative XRD analysis results of bulk mudstone and very fine-grained sandstone lithofacies.

Sample name	Mineral phases identified	Description/facies	Location in the basin
D1_S2_NP	Qtz, Mq, Il, Phl, Lep, Montm, Gyp, Ilm, Chl-Verm-Montm, Monte	Fm	Centre
D1_S2_P	Qtz, Mq, Il, Lep, Verm, Chl-Verm-Montm, Micr	Fp	Centre
D4_S3_1	Phl, Lep, Montm, Kao, Gy, Ch-Verm-Montm, Sau, Micr	Fm	Centre
D6_S2_26	Qtz, Mq, Il, Alb, Lep, Goe, Montm, Micr, Ilm	Fm (clayey)	West
D8_S7_FF	Qtz, Mq, Il, Lep, Montm, Sau, Verm, Pyr, Micr	Fm (clayey)	Centre - SW
D11_S3_15	Qtz, Mq, Il, Phl, Lep, Montm, Verm, Nontr, Monte, Pyr	Very fine-grained sandstone (clay fraction)	South
D12_S1_16	Qtz, Mq, Il, Phl, Montm, Pyr	Fine-grained sandstone (clay fraction)	South-east
D17_S2_53	Qyz, Mq, Orth, Hem, Chl-Verm-Montm, Beid, Il, Montm, Verm, Nontr	Very fine-grained sandstone (clay fraction)	South - SW